

VERSATILE STRUCTURED ILLUMINATION MICROSCOPY

VERSATILE STRUCTURED ILLUMINATION MICROSCOPY

Proefschrift

ter verkrijging van de graad van doctor
aan de Technische Universiteit Delft,
op gezag van de Rector Magnificus prof. ir. K.C.A.M. Luyben,
voorzitter van het College voor Promoties,
in het openbaar te verdedigen op dinsdag 1 januari 2017 om 10:00 uur

door

Nadezda CHAKROVA

geboren te Almaty, Kazakhstan.

Dit proefschrift is goedgekeurd door de

promotor: prof. dr. L.J. Van Vliet

copromotors: dr. S. Stallinga en dr. B. Rieger

Samenstelling promotiecommissie:

Rector Magnificus,	voorzitter
Prof. dr. A. Kleiner,	Technische Universiteit Delft
Dr. A.A. Aaronson,	Technische Universiteit Delft

Onafhankelijke leden:

Overige leden:



Keywords: ...

Printed by: Gildeprint

Front & Back:

Copyright © 2016 by N. Chakrova

ISBN 000-00-0000-000-0

An electronic version of this dissertation is available at
<http://repository.tudelft.nl/>.

CONTENTS

Summary	ix
Samenvatting	xi
1 Introduction	1
1.1 Fluorescence microscopy	3
1.1.1 Inside a fluorescence microscope	3
1.1.2 Limitations of widefield fluorescence microscopy	3
1.2 Deconvolution and confocal microscopy	5
1.3 Super-resolution fluorescence microscopy	7
1.4 Structured Illumination Microscopy	9
1.4.1 Image formation in SIM	9
1.4.2 Examples of SIM images	11
1.4.3 The diversity of SIM methods	11
1.5 Objectives of this thesis	13
1.5.1 Motivation	13
1.5.2 Thesis outline	14
References	15
2 Development of a DMD-based fluorescence microscope	19
2.1 Introduction	20
2.2 Experimental methods	21
2.2.1 Digital micro-mirror device operation	21
2.2.2 Setup layout	23
2.2.3 Samples	24
2.3 Optical quality assessment	24
2.3.1 Estimating the MTF by the edge-profile measurement method	24
2.3.2 Theoretical MTF curves	25
2.3.3 Comparison of the experimental and theoretical MTF curves	26
2.4 Mapping the DMD to the camera	28
2.5 Multi-spot illumination results	29
2.6 Outlook on the use of pseudo-random patterns	31
References	32
3 Studying different illumination patterns for resolution improvement in fluorescence microscopy	35
3.1 Introduction	36
3.2 Theory	37
3.2.1 Fourier Ptychography method as steepest descent of a quadratic function	37

3.2.2	Fourier Ptychography algorithm with Newton-Raphson update . . .	39
3.3	Simulations	41
3.3.1	Simulation setup	41
3.3.2	Stopping criterion	42
3.3.3	The effect of sparsity and number of pseudo-random patterns . . .	43
3.3.4	Comparison of illumination pattern types	45
3.4	Experiment	47
3.4.1	Experimental setup	47
3.4.2	Imaging fluorescent beads	48
3.4.3	Imaging filamentous samples	50
3.4.4	Reconstruction of illumination patterns	50
3.5	Conclusion	52
3.6	Acknowledgments	54
	References	54
4	Deconvolution methods for structured illumination microscopy	59
4.1	Introduction	60
4.2	Theory	61
4.2.1	Image reconstruction in SIM with MLE	61
4.2.2	Pattern-illuminated Fourier Ptychography	63
4.2.3	Joint Richardson-Lucy deconvolution	63
4.2.4	Newton-Raphson update step	64
4.3	Simulation results	64
4.3.1	Quantitative assessment of the reconstructed images	65
4.3.2	Object-dependent resolution improvement	68
4.4	Experimental results	70
4.4.1	Read-out noise of the sCMOS camera	70
4.4.2	Comparison to the performance of commercial SIM microscope . .	72
4.5	Conclusion	72
4.6	Acknowledgments	74
	References	74
5	Adaptive Structured Illumination Microscopy for photobleaching reduction	79
5.1	Introduction	80
5.2	Principles of adaptive SIM	81
5.2.1	Calculation of the illumination mask	82
5.3	Materials and methods	82
5.3.1	Experimental setup	82
5.3.2	Mapping the DMD onto the camera	83
5.3.3	Sample preparation	83
5.4	Experimental results	84
5.4.1	Photobleaching behavior of the fluorophore	84
5.4.2	Illumination mask examples	85
5.4.3	Image quality in adaptive SIM	85
5.4.4	Photobleaching studies	86
5.4.5	The influence of out-of-focus light	88

5.5	Conclusion	88
5.6	Acknowledgements	90
	References	90
6	Conclusion	95
6.1	Results	96
6.1.1	Optical sectioning in a DMD-based SIM microscope	96
6.1.2	Resolution-doubling in a DMD-based SIM microscope	96
6.1.3	Adaptive SIM.	98
6.2	Discussion and Outlook.	99
6.2.1	Future SIM.	99
6.2.2	Developments in deconvolution	100
6.2.3	Comparison to Selective Plane Illumination Microscopy.	100
6.2.4	Image quality assessment	100
6.2.5	Suggestions for follow-up research in adaptive SIM	101
	References	102
	List of Publications	105

SUMMARY

Biological cells are very small units with an incredibly complex organization. Biologists who try to understand the processes within the cells use fluorescence microscopes as visualization tools on a daily basis. The popularity of fluorescence microscopy originates from the specificity of labeling, which makes it possible to study the functionality of components within the structure of living biological cells. This thesis focuses on Structured Illumination Microscopy (SIM) – a technique that provides optical sectioning and lateral resolution of up to two times the resolution of standard fluorescence microscopy.

As the name suggests, in SIM a sample is illuminated not uniformly, but with a number of different illumination patterns. An image with improved resolution and optical sectioning is mathematically reconstructed from the set of acquired images corresponding to different illumination patterns. Several illumination pattern types and a number of different reconstruction algorithms can be employed for this purpose. In this thesis we present an adaptive SIM microscope, built on the basis of a digital micro-mirror device (DMD). We study which type of illumination and which type of reconstruction are preferable, and address the photobleaching problem in SIM.

Our DMD-based SIM microscope has a single-pass configuration: structured illumination is provided by the DMD, and the fluorescence is detected in a widefield manner. Resolution improvement and optical sectioning are obtained during the digital post-processing of the acquired images. The optical design of a DMD-based microscope takes the diffraction effects of the DMD into account, and the optical quality is estimated by the modulation transfer function (MTF) obtained from an edge-profile measurement.

The flexibility of a DMD-based SIM microscope enables the study of various illumination patterns. We examine how the quality of the reconstructed images and the convergence speed of the reconstruction algorithms depend on the sparsity and the number of random patterns. Furthermore, we experimentally demonstrate that periodic (line and multi-spot) patterns are superior to random patterns in terms of resolution improvement and signal-to-noise ratio (SNR) even when illumination patterns are known and integrated into the reconstruction process. High spatial frequency components have larger magnitudes in periodic patterns, resulting in a better support of the optical transfer function in the reconstructed images.

The reconstruction problem is addressed in this thesis by formulating a generalization of the maximum likelihood estimation methods in SIM. Depending on the choice of the noise model, update step and regularization function, this generalization reduces to different well-known forms of reconstruction algorithms. We examine in detail two particular cases – the pattern illuminated Fourier Ptychography (piFP) and the joint Richardson-Lucy (jRL) algorithm. Via our generalization we identify the piFP algorithm as a steepest descent optimization of a quadratic error function, derived using a Gaussian noise model. By studying MTF curves representing different types of sample structures, we show that the resolution improvement in piFP reconstructions is uniform,

whereas in the jRL reconstructions it is object-dependent. The convergence speed, resolution improvement and SNR provided by the piFP and jRL algorithms are further compared in experiments conducted on fixed cells. We find that the convergence of the piFP algorithm is up to ten times faster than the convergence of the jRL algorithm. However, the piFP algorithm results in images with higher noise amplification and more pronounced artifacts. Dense and periodic objects are better resolved using piFP algorithm, while isolated objects are better resolved using the jRL algorithm. A combination of both methods provides the best overall results.

As a technique for visualization of biological specimens, fluorescence microscopy should be as non-invasive as possible. This thesis proposes an adaptive illumination scheme for SIM, which reduces the overall illumination light dose and, thereby, attenuates the photobleaching. In adaptive SIM the illumination intensity is locally adjusted according to the sample, such that brighter sample areas receive less light than darker sample areas. The decrease in photobleaching is quantified using the integrated image intensity in time-lapse experiments performed on fixed cells. We demonstrate a photobleaching reduction in adaptive SIM which enables a three times longer observation time than in non-adaptive SIM.

In a nutshell, the research work presented in this thesis contributes to the ongoing development of SIM as a flexible and minimally invasive technique for high-resolution imaging of living cells.

SAMENVATTING

Samenvatting in het Nederlands...

1

INTRODUCTION

The interest in life on a scale smaller than the limit of human eyesight and attempts to understand what constitutes matter appeared very early in history. Already in ancient Greece a concept of small building blocks of matter - atoms - was introduced, although, of course, more in a philosophical than in an experimental way. Today it is known that the world of microorganisms, cells, molecules and atoms is hidden behind the apparent integrity of the objects in our daily environment. Since the smallest details seen by a naked human eye are on the order of $\sim 50 \mu\text{m}$, people are not able to discern the building blocks of matter without special tools. With the help of modern light and electron microscopes, however, we can visualize structures that are several orders of magnitude smaller than the naked human eye allows us to see.

One of the most exciting small-scale worlds we can peek into today is the world of a living biological cell. Cells have complex organization and appear in many different types. Fig. 1.1 shows an overview of the cells and subcellular components together with microscopy techniques that can be used for visualizing them. Developments in cell biology have a large impact on medicine, genetics, nutrition, agriculture and many other areas of human activity. Although huge progress has been made in identifying various components of the cells and their functions, many of the intracellular processes remain poorly understood. An indispensable technique for studying these processes is fluorescence microscopy, which enables specific labeling of cellular structures.

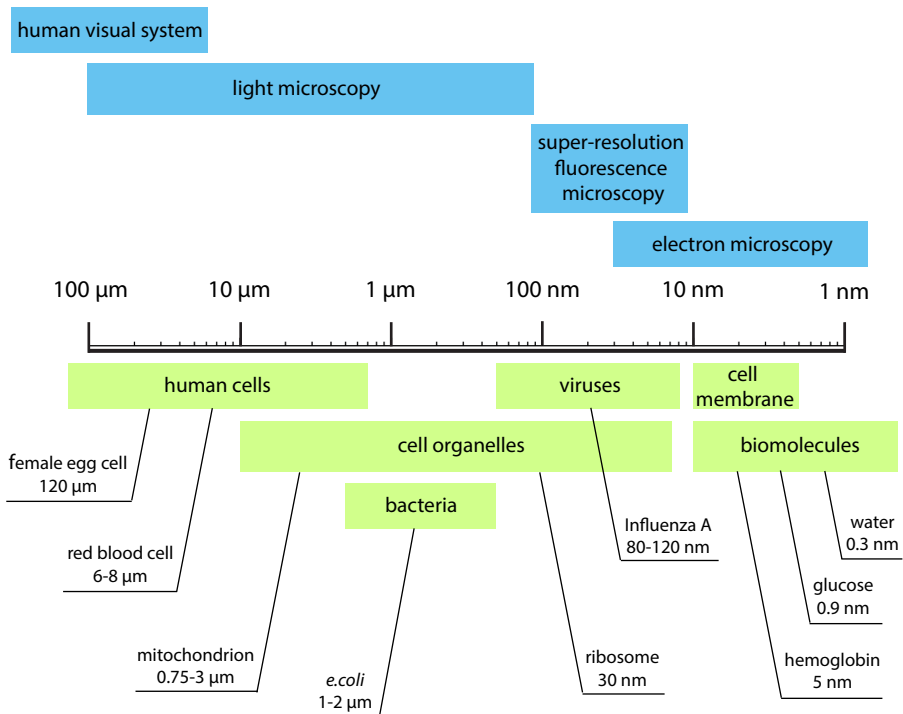


Figure 1.1: Characteristic length scales of cells, cellular components and biomolecules are shown together with microscopy techniques that can be used for their visualization.

1.1. FLUORESCENCE MICROSCOPY

FLUORESCENCE microscopy is a truly interdisciplinary field. It is mostly used in biological labs, however, it owes its existence to advances made in the fields of electronics, optics and biochemistry. Moreover, modern microscopes use digital cameras to capture images. Hence, quantitative analysis of the acquired images additionally requires, to a greater or lesser extent, digital image processing tools.

1.1.1. INSIDE A FLUORESCENCE MICROSCOPE

In fluorescence microscopy a biological sample is stained with fluorescent labels. The labeling methods depend on the cellular structure of interest and the parameters of the experiment. These methods can be roughly divided into three groups: staining using fluorescent dyes that bind specifically to the target molecules, immunolabeling using fluorescently labeled antibodies, and labeling using fluorescent proteins (FP), which are expressed by the cell after genetic modification. The emergence of FP labels, which started with extracting and sequencing of the green fluorescent protein (GFP), hugely increased the usage of fluorescence microscopy, since FP labels make it possible for biologists not only to locate specific proteins, but also to study their functionality in living cells. A wide range of fluorescent dyes and engineered FPs is currently available for labeling different cellular structures at various wavelengths. The field of biochemistry is engaged in designing fluorescent labels and improving their performance in terms of selectivity, stability and brightness.

As an optical instrument, a fluorescence microscope has to provide illumination of the labeled sample and allow observation of the emitted fluorescence. To this end fluorescence microscopes typically have an epi-illumination design, which means that the excitation and emission light both pass through the objective lens (see Fig.1.2). The fluorescently labeled sample is illuminated with the wavelength that corresponds to the energy difference between the ground state and excited singlet state of the fluorescent molecules. Lamps, light emitting diodes (LEDs) and lasers can be used as light sources, and the correct illumination wavelength is selected using the excitation filter. The excitation beam is focused onto the sample by an objective lens – the core optical element of the microscope. Fluorescent molecules absorb illumination light and emit fluorescence light, which has a slightly larger wavelength due to the Stokes shift. In order to separate excitation and emission light, a dichroic mirror and an emission filter are placed in the optical path. The dichroic mirror reflects illumination light and transmits fluorescence light, i.e. acts as a wavelength-dependent beam splitter. This component is produced using thin film deposition. After passing through the dichroic and emission filters, the fluorescence signal is detected by a digital camera. Since fluorescence signals are often weak, one of the main requirements for the camera is a high sensitivity and low read-out noise. In applications where the sensitivity of the conventional CCD camera is not sufficient EM-CCD or sCMOS cameras are used.

1.1.2. LIMITATIONS OF WIDEFIELD FLUORESCENCE MICROSCOPY

The most widely used type of fluorescence microscopes is the widefield microscope. It provides uniform sample illumination and captures an image of the whole field of view in one camera shot. The major advantages of widefield fluorescence microscopy are fast

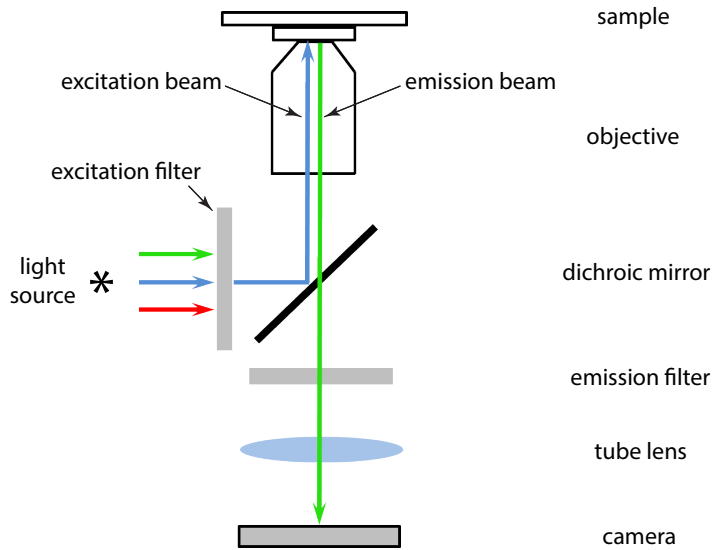


Figure 1.2: Schematic view of the epi-illumination fluorescence microscope setup. The sample is illuminated with light that passes through the excitation filter and reflects off the dichroic mirror. The most important component of the microscope, the microscope objective lens, focuses the excitation light onto the sample. Fluorescent labels in the sample absorb excitation light and emit fluorescence. The fluorescence light is collected by the same microscope objective, then passes through the dichroic mirror and emission filter to be imaged by the camera.

image acquisition, low illumination light doses, and ease of use.

The lateral resolution in a widefield microscope is limited by diffraction and, according to Ernst Abbe's formula [1], is proportional to $\lambda/2NA$, where λ is the emission wavelength and NA is the numerical aperture of the objective lens (the resolution in Abbe's formula is defined as the smallest resolvable period of a grating). Hence, better resolution can be achieved by using shorter wavelengths and higher NA optics. High NA objectives are complex multi-component lenses, meticulously designed to correct for chromatic aberrations, spherical aberrations, coma, astigmatism, and field curvature. The routinely used high NA water and oil immersion objectives have $NA = 1.2 - 1.45$, which results in a lateral resolution of approximately 200 nm at $\lambda = 500$ nm. This means that an infinitely small point appears as a blurred spot with a size of ~ 200 nm when imaged by such an objective lens. The blurred spot is termed the Point Spread Function (PSF), and is given by an Airy disk in case of an aberration-free axisymmetric lens [2], provided the NA is low enough for scalar diffraction to be valid. An image of an object appears as if each point of an object was substituted by the PSF – a process, which is mathematically described by a convolution of the object with the PSF of the objective lens.

In most cases the sample under study has a three-dimensional (3D) structure and the observer is interested in the 3D distribution of the target molecules. The depth of field of a widefield microscope is, however, worse than the lateral resolution, and is about 500 – 700 nm. 3D imaging is typically performed by moving the objective in small steps in the axial direction and acquiring an image (section) at every position of the objective. However, when the microscope objective focuses the excitation beam onto the sample, the whole volume of the sample is illuminated rather than a selective plane. As a result, fluorescence from the planes below and above the focal plane contributes to the image at a current focal plane, thereby lowering the contrast and reducing the signal-to-noise ratio (SNR) of an image. Poor optical sectioning is one of the limitations of the widefield microscopy.

In general, applying the term "three-dimensional imaging" in high resolution epillumination fluorescence microscopy is a slight overstatement, since only very thin specimens can be studied with this technique. The penetration depth with high-NA oil immersion objectives can be at best $\sim 100 \mu\text{m}$, if the refractive index of the specimen is matched to the refractive index of the immersion medium. In many practical cases, however, the penetration depth is only 10–20 μm due to the scattering and absorption within the specimen. In order to perform actual 3D imaging one could refer to Light Sheet Fluorescence Microscopy [3], or, alternatively, to one of the non-fluorescent medical imaging techniques with substantially lower resolution, such as Optical Coherence Tomography [4].

1.2. DECONVOLUTION AND CONFOCAL MICROSCOPY

ALTHOUGH the widefield fluorescence microscope is a widespread practical tool, its resolution is not sufficient to visualize many of the cellular components and processes of interest. Two established methods to improve the resolution and, most importantly, the poor optical sectioning of a widefield microscope are confocal microscopy and deconvolution.

As mentioned in section 1.1.2, the blurring of the object during the imaging process is mathematically described by convolution of the sample with the PSF of the microscope. Image processing algorithms developed to reverse the convolution and in that way de-blur the image are referred to as deconvolution. Deconvolution is typically performed in the domain of spacial frequencies, the so-called Fourier space. Deconvolution in its basic form - the direct inverse filtering in Fourier domain - is a simple and fast process, which would immediately result in a perfect image in the absence of any noise, accurate knowledge about the PSF, and assuming $C(x,y) = 0$ everywhere. In reality, unfortunately, the image is always corrupted by shot noise, which has a Poisson distribution, and the camera read-out noise, which has a Gaussian distribution. Deconvolution of noisy images by direct inverse filtering does not give the desired effect and, in fact, is never used for recovering the blurred images in fluorescence microscopy. Practical solutions to the deconvolution problem of noisy images employ various noise models to generate sharpened images with improved sectioning [5–8]. The actual power of deconvolution is quite limited, but it remains a very popular method to boost the resolution and contrast of widefield fluorescence microscopy images, since it does not require any additional equipment or any change in the image acquisition process. All resolution improvement methods have their drawbacks, and deconvolution is no different. The deconvolution algorithms, often iterative, are based on a number of back and forth Fourier transforms of the image, and lead to image reconstruction artefacts. Most commonly, the artefacts manifest themselves as ringing structures at the borders of objects and speckle-like noise amplification throughout the image.

Confocal microscopy was the first technique developed to improve upon the performance of the fluorescence microscope by using a novel optical configuration instead of digital image restoration [9, 10]. In a confocal microscope the sample is illuminated by a diffraction-limited spot and the fluorescence is detected through a pinhole, positioned in the conjugate image plane. The illumination spot is scanned over the sample, and the fluorescence signal is registered at each scanning position by the a photodetector placed behind the pinhole. The smaller the detection pinhole, the higher the obtained resolution. Theoretically, in confocal microscopy a resolution improvement of $2\times$ over widefield microscopy can be achieved. Realistically, the detection pinhole can never be made sufficiently small for such an improvement due to the low SNR. Therefore, the image quality in confocal microscopy is mainly improved because of the enhanced image contrast, obtained due to the efficient out-of-focus light rejection by the detection pinhole. In order to achieve acceptable SNR, the illumination intensity in confocal microscopy has to be increased. The high illumination light doses lead to photobleaching, which is the loss of illumination intensity as a result of the permanent chemical damage of the fluorescent molecules, and phototoxicity, which is the light-induced damage of the cellular components and changes in the behavior of the cells. Photobleaching and phototoxicity of the biological samples under study are negative side effects of confocal microscopy.

Both 3D deconvolution of widefield images and confocal microscopy are described in the literature in great detail [6–8, 11]. These methods produce images with similar quality: confocal microscopy by blocking the out-of-focus light, and deconvolution microscopy by reallocating the out-of-focus light back to its original axial position. The

combination of two - the deconvolution of confocal images - produces the best results [12].

1.3. SUPER-RESOLUTION FLUORESCENCE MICROSCOPY

SEVERAL methods to further improve the lateral and axial resolution of a standard widefield fluorescence microscope were developed in the last 20 years. These methods got the collective name "super-resolution microscopy", and granted some of their inventors the Nobel prize in chemistry 2014.

The super-resolution methods have evolved in three major directions. One of the directions, named localization microscopy, is using localization of single fluorescent molecules in order to form an image [13–15]. First, the sample is labeled with photo-switchable or photo-activatable fluorophores, which have blinking behavior – they undergo a number of cycles with "on" (emitting) and "off" (non-emitting) states. Next, a couple of thousands of camera acquisitions is taken. The switching rate of the fluorophores, labeling density and camera exposure time have to be balanced in such a way, that in each separate camera frame the emitting fluorophores are located at least half of the microscope PSF apart. If fluorophores appear sufficiently sparse from each other, they can be individually localized, namely, the PSF model can be fitted to each separate emitting fluorescent molecule. The coordinates of the localizations from all the fluorophores in all the camera frames form a pointillistic image. The resolution in this image is defined by the labeling density and localization precision, it typically amounts to ~ 10 – 30 nm laterally and ~ 100 nm axially. The downsides of localization microscopy in comparison to widefield microscopy are long image acquisition times, increased illumination doses, the need for fluorophores with special characteristics and post-processing of the acquired images.

The second super-resolution method is Stimulated Emission Depletion (STED) microscopy [16]. In STED the sample is illuminated by two overlapping beams with aligned centers. The first beam produces a diffraction-limited PSF and is used for the excitation of the fluorescent molecules. The second beam has a donut-shaped PSF and is used for depletion of the fluorescence at the outer rim of the first beam. The resulting depleted spot has a PSF that is substantially more narrow than the original diffraction-limited PSF. The STED image is acquired by scanning this spot across the sample. STED microscopy reaches 30 – 100 nm lateral and ~ 100 nm axial resolution. The major disadvantages of this method are very high illumination light doses and complicated alignment of the optical setup.

Another group of super-resolution methods is based on structured illumination of the specimen [17–20]. In conventional Structured Illumination Microscopy (SIM) the sample is illuminated with a number of very fine sinusoidal patterns. For each of the illumination patterns a separate camera image is taken. Registered images represent the interference of the sample with illumination patterns. These interference patterns can be seen as *Moiré* effect, which describes a situation when the superposition of two fine periodic patterns with small periods results in a third periodic pattern with a larger period (shown in Fig. 1.3). In SIM the sample structures that are smaller than the diffraction limit, and, hence, previously could not be captured by the microscope objective, are now interfering with the illumination pattern and become observable via the used

objective. The final SIM image has to be mathematically reconstructed from the registered interference patterns. The resolution improvement is defined by the pitch of the projected illumination pattern. In the case of an epi-illumination microscope the pitch of the projected pattern is limited by the NA of the objective, therefore, the resolution in SIM can be up to $2\times$ better than in a widefield microscope. In order to achieve the axial resolution improvement in SIM, the sample has to be illuminated by patterns that are additionally modulated along the axial direction. The limitations of the SIM method are the high risk of reconstruction artifacts and only modest (up to $2\times$) resolution improvement. Theoretically, the resolution in SIM can be extended further by exploiting nonlinearity between the illumination intensity and emission rate. Such nonlinearity can be achieved by saturation of the fluorophores [21]. The corresponding technique, termed saturated SIM (SSIM), has been shown to generate images with resolution on the order of 50 nm [22, 23]. However, applicability of SSIM to live cell imaging is limited due to the induced photobleaching.

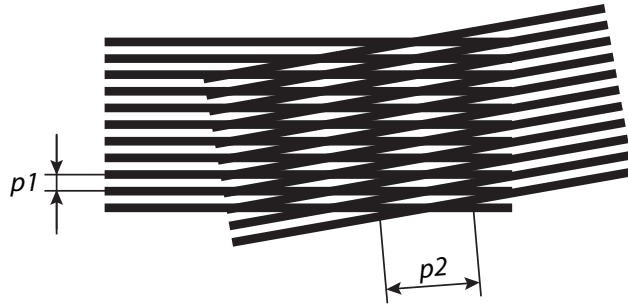


Figure 1.3: Visualization of the *Moiré* effect. The superposition of two periodic patterns with small period p_1 forms a third periodic pattern with larger period p_2 . In SIM, fine structures, which cannot be resolved by the microscope objective, become observable thanks to the interference with the illumination pattern.

Various super-resolution methods are complimentary to each other. Localization microscopy methods offer the best resolution, however, require special dyes and have low temporal resolution. STED allows faster imaging, however, is harmful for the biological samples due to the high illumination doses. SIM offers fast and less aggressive imaging, but a rather small resolution improvement. The choice of the super-resolution technique for a particular study depends on the specific experimental parameters: the sample under study, available dyes, required axial and lateral resolution, and the speed of the observed biological process. All of the discussed methods have been commercialized, and modern biological labs often have several types of super-resolution microscopes at their disposal. In this work we focus on SIM, which will be discussed in more detail further on.

1.4. STRUCTURED ILLUMINATION MICROSCOPY

1.4.1. IMAGE FORMATION IN SIM

A very useful concept to interpret the resolution improvement in SIM is the Optical Transfer Function (OTF). The OTF is the Fourier transform of the PSF, it indicates which spatial frequencies k can be transmitted through the optical system. The OTF of a widefield fluorescence microscope is given by the autocorrelation function of the exit pupil of the objective. As can be seen in Fig. 1.4, the transmission of a widefield

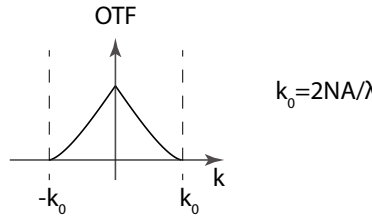


Figure 1.4: OTF of a widefield fluorescence microscope is given by the autocorrelation of the pupil function of the objective, and is limited to $|k| < k_0$, with $k_0 = 2NA/\lambda$, NA is the numerical aperture of the objective and λ is the wavelength of the emitted fluorescence.

OTF decreases with increasing spacial frequency $|k|$, and is limited to $|k| < k_0$, where $k_0 = 2NA/\lambda$. Enlarging the OTF footprint of the microscope corresponds to improving its resolution. In order to understand why SIM has an extended OTF, we will examine the image formation in 2D SIM in the absence of noise.

Consider a fluorescently labeled object x illuminated by a sinusoidal illumination pattern p with periodicity corresponding to the cutoff frequency of the microscope objective k_0 , as shown in Fig. 1.5(A). The objective collects emitted fluorescence and forms an image f :

$$f(r) = (x(r) \cdot p(r)) \otimes h(r), \quad (1.1)$$

where r is the coordinate vector, \otimes symbol is used for convolution, and h is the objective PSF. In the Fourier domain Eq. 1.1 is given by:

$$F(k) = (X(k) \otimes P(k)) \cdot H(k), \quad (1.2)$$

where capital letters F, X, P and H denote the Fourier Transforms (FT) of the functions f, x, p and h , and $H(k)$ is the OTF of the microscope. Since the illumination pattern is given by a sinusoidal pattern plus an offset, its FT consists of three delta peaks (see Fig. 1.5(B)). Assuming full modulation depth of the sinusoidal pattern, Eq. 1.2 can be written as:

$$F(k) = (X(k) + \frac{1}{2}X(k - k_0)e^{2\pi i\phi} + \frac{1}{2}X(k + k_0)e^{-2\pi i\phi}) \cdot H(k), \quad (1.3)$$

where ϕ is the phase of the sinusoidal pattern. Equation 1.3 represents the mixture of three spectral components, attenuated by the OTF. Since two of these spectral components are shifted by $\pm k_0$, the previously undetectable parts of the spatial frequency spectrum of an object ($k \in [k_0, 2k_0]$) and $k \in [-2k_0, -k_0]$) fall into the transmission pass-band

of the microscope's OTF and can now be observed (see Fig. 1.5(B)). The effective OTF in

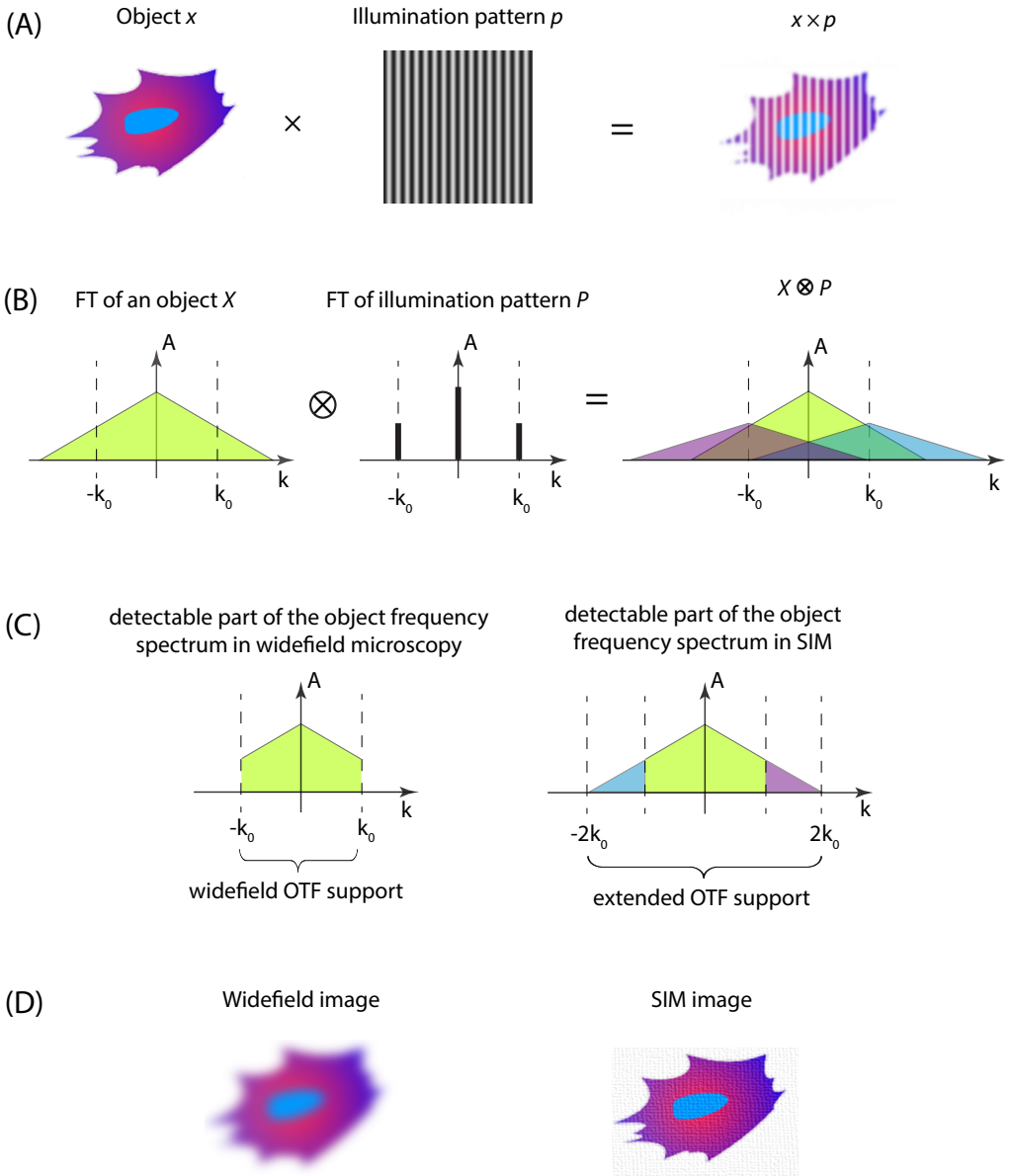


Figure 1.5: Illustration of the working principle of SIM. (A) An object x is illuminated by a sinusoidal pattern p . (B) Convolution of the spatial frequency spectra of the object and illumination pattern produces three copies of the original spatial frequency spectrum of the object. Previously unobserved parts of the object frequency spectrum are shifted into the pass-band of the microscope OTF. The OTF pass-band is indicated by the dashed lines at k_0 and $-k_0$. By separating the copies and shifting them to their original positions, we obtain an extended OTF support (C) and, hence, an improved resolution (D).

SIM is therefore approximately twice larger than in a widefield microscope (Fig. 1.5(C)). In order to reconstruct an image with extended OTF, the three components have to be separated, shifted to their original positions, and combined together again. To allow separation of the three components, at least three images with different phases ϕ have to be acquired. An isotropic resolution improvement is achieved by repeating this procedure for three orientations of the sinusoidal pattern. Thus, the final 2D SIM image is reconstructed from 9 raw acquisitions.

1.4.2. EXAMPLES OF SIM IMAGES

The resolution improvement in SIM comes at the cost of artefacts associated with the image reconstruction process. Fig. 1.6 demonstrates both the resolution improvement and reconstruction-induced artefacts in SIM. An air objective with $NA = 0.7$ was used to image the resolution target in widefield and SIM modes. The resolution target contains a chirped comb of closely spaced lines. The distances between the lines range from 340 nm to 400 nm with a step of 5 nm, which is close to the diffraction limit of the objective $\lambda/2NA = 372$ nm. The lines are not resolved in the widefield image (1.6(b)), but are clearly distinguishable in the SIM image (1.6(a)).

Additionally, a widefield image was taken with an oil immersion objective with $NA = 1.45$ for comparison. Since the NA of the oil immersion objective is approximately twice larger than the NA of the air objective, the SIM image produced with the 0.7 NA objective (1.6(a)) is comparable to the widefield image produced with the 1.45 NA objective (1.6(c)). However, the overall quality of the widefield image is higher due to the better SNR and the absence of the reconstruction artefacts. The artefacts, characteristic of SIM (and, more generally, of deconvolution-based methods), can be observed in image 1.6(a): edge ringing, indicated with red arrows, and noise amplification, pronounced in the background areas and in the tainted appearance of the originally straight lines.

1.4.3. THE DIVERSITY OF SIM METHODS

The term "structured illumination" is used quite loosely in fluorescence microscopy. A large group of methods for optical sectioning and resolution-doubling employ structured illumination of some form. Frequently used types of structured illumination include sinusoidal, multi-spot, and pseudo-random patterns. Here we provide an overview of various SIM methods.

Confocal microscopy can be seen as the most basic example of sectioning achieved by structured illumination, where the illumination pattern consists out of only one spot. Several techniques were developed to improve the performance of confocal microscopes. Spinning disk microscopes are using multiple illumination spots to scan the sample in parallel in order to speed up confocal microscopy [25]. Furthermore, Programmable Array Microscopes (PAM) provide sectioning by using Spatial Light Modulators (SLM) in the illumination and detection paths of the microscope [26–29]. SLMs are pixelated displays, which allow projection of binary or gray-scale images at high speed. In a double-pass PAM, pixels of the SLM play the role of programmable pinholes and the out-of-focus light is not blocked, but redirected to a different optical path and registered by a second camera. This makes it possible to use very dense pseudo-random illumination patterns. As a result, PAM can perform optical sectioning at high speed with improved

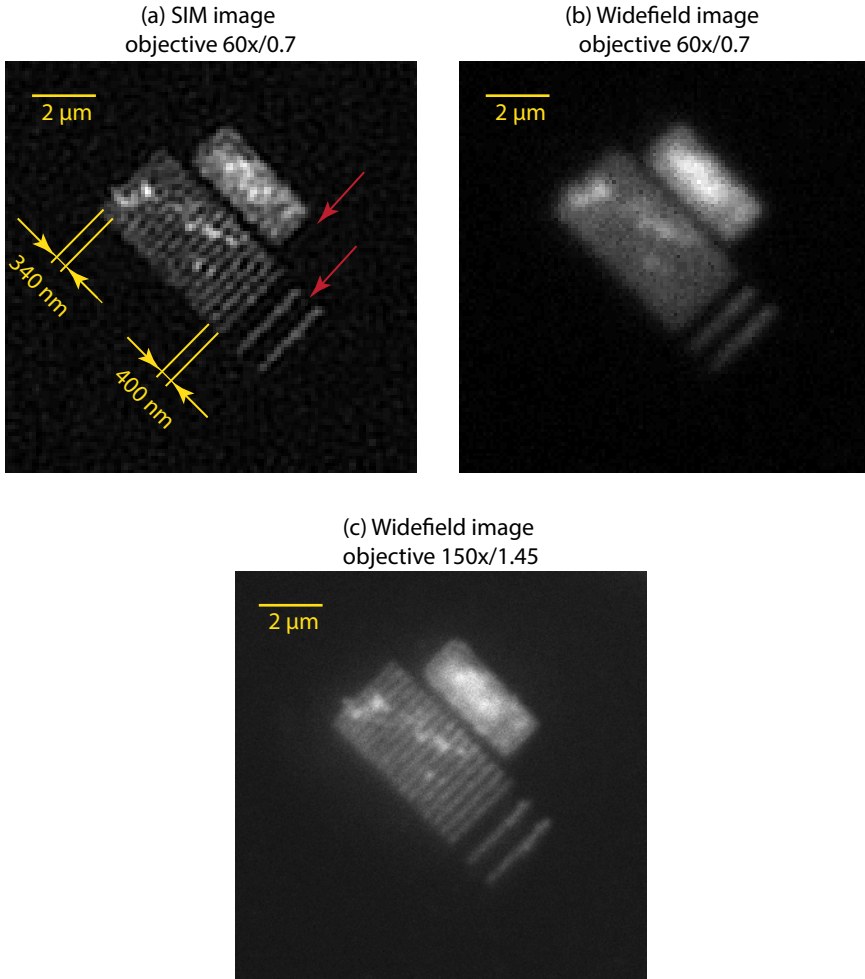


Figure 1.6: Resolution improvement in SIM over widefield microscopy. Images of the resolution target containing closely spaced lines were taken with the $60\times/0.7$ objective. The lines that are resolved in a multi-spot SIM imaging mode (a) can not be discerned in a widefield mode (b). SIM image (a) displays the reconstruction artefacts in the form of noise amplification (pronounced in the background) and edge ringing (indicated by red arrows). Another widefield image taken with a $150\times/1.45$ objective is given for comparison. (Sample courtesy S. Hari (TU Delft - Imaging Physics), [24])

sensitivity. A different way to obtain sectioning by structured illumination is to use three phase-shifted sinusoidal line illumination patterns in combination with widefield detection and computational reconstruction [30]. Finally, speckle illumination, created by projecting the surface of a diffuser onto the sample [31–33], can also be used for optical sectioning. The latter two recipes are different from other sectioning methods, since in their case the rejection of out-of-focus light is achieved during the image reconstruction process, whereas in confocal, spinning disk and PAM microscopes it occurs optically.

The bridging technique between the optical sectioning SIM and resolution-doubling SIM is Image Scanning Microscopy (ISM) [34]. Just like in confocal or spinning disk microscopy, in ISM a single or multiple foci are used to scan the sample. However, in contrast to confocal microscopy, in ISM widefield detection of fluorescence is used. Thus, every pixel of the detector registers light for each scanning position of the illumination spot(s). The ISM reconstruction algorithm corrects for the shift between the excitation and detection PSFs for all pixels of the detector that are positioned off the optical axis. As a result, a resolution improvement of approximately $\sqrt{2}$ over widefield microscope is achieved. In practice, additional deconvolution of the reconstructed ISM image provides further resolution improvement. The ISM principle has been demonstrated in confocal [34], spinning disk [35], and SLM-based microscopes [36]. Moreover, several all-optical ISM implementations, based on augmenting a confocal microscope with a second, (re)scanning, step, are of practical interest [37–39].

The resolution-doubling SIM also encompasses a number of different realizations. In standard resolution-doubling SIM a fine sinusoidal illumination pattern is created by a movable diffraction grating, which is placed in the image plane of the microscope. The reconstruction of the final image is done using the so-called generalized Wiener filter [40]. This implementation is adopted by all commercial SIM microscopes. Alternatively, the structured illumination can be created by an SLM [36, 41, 42] or by a diffuser [43], and the reconstruction can be done using statistical methods [43–45]. In the following we will use the term 'SIM' to refer to the resolution-doubling techniques only.

Interestingly, all of the above mentioned techniques can in principle be realized within one instrument: a microscope, which is equipped with an SLM. An SLM allows projection of any suitable illumination pattern onto the sample, whether multi-spot, sinusoidal, or pseudo-random (speckle) patterns. Depending on the chosen illumination pattern and reconstruction algorithm, this microscope can perform either optical sectioning or resolution improvement according to one of the schemes described above. Such a flexible SLM-based microscope is the object of the present research.

1.5. OBJECTIVES OF THIS THESIS

1.5.1. MOTIVATION

AFTER its first successful experimental demonstration in 2000, SIM technology has reached biological labs and has been quite quickly commercialized. However, the current commercially available SIM implementations have several shortcomings.

First of all, the hardware of a commercial SIM is based on a movable diffraction grating, which has a fixed pitch size. This limits the flexibility of the SIM machine, since only a few objectives match the grating perfectly. The flexibility of SIM can be improved by substituting the diffraction grating with an SLM, as the type and the pitch of the illumination pattern projected by an SLM can be adapted to the particular sample or objective.

Next, the software of a commercial SIM is based on separating the two modulated and the unmodulated copies of the spatial frequency spectrum of the object in the detected images, placing them at the original positions and combining via a generalized Wiener filter. As a result of this procedure, reconstructed SIM images often suffer from artefacts. Most common artefacts are edge ringing and noise amplification due to in-

sufficient apodization [46], and residual stripe patterns due to the inaccurate shift of the grating and photobleaching of the sample [47]. Therefore, consideration must be given to the development of novel SIM reconstruction algorithms.

Last, but not least, photobleaching and phototoxicity present a very serious issue in fluorescence microscopy. These negative side effects do not only hamper the extended observation of the biological samples, but also cast doubt on the naturalness of the observed processes. The photobleaching and phototoxicity rates increase with increasing light illumination dose. In order to provide long imaging and prevent harmful light-induced intracellular interactions, the light dose in fluorescence microscopy has to be reduced.

In this thesis we address the discussed issues by developing an adaptive SLM-based SIM microscope. The thesis includes the optical design and characterization of the microscope, investigation of various illumination types, comparison of reconstruction algorithms, and, finally, consideration of light dose reduction strategies. This multifocal research work is a step towards a more robust and flexible SIM microscope as a tool suitable for imaging sensitive biological samples.

1.5.2. THESIS OUTLINE

Chapter 2 provides a technical reference to the development of a microscope with a digital micro-mirror device (DMD) incorporated in its conjugate image plane. We present an optical design of a single-pass SIM and discuss several issues related to this design, mainly focusing on the diffraction effects of the DMD. The optical quality of the microscope is estimated by measuring the modulation transfer function (MTF) with the edge-profile method. Images, produced using multi-spot scanning patterns, display out-of-focus light rejection, i.e. a sectioning effect. The strength of the sectioning effect is estimated from the SNR and signal-to-background ratios. The final image in case of multi-spot illumination is reconstructed by applying digital pinholing to each raw image and summing up the processed images. We study the influence of the pitch of the projected multi-spot patterns and the size of the digital pinhole on the sectioning capabilities of our DMD-based microscope.

Since resolution-doubling SIM can be accomplished in different ways, it is important to understand the benefits and drawbacks of each implementation. In **Chapter 3** we question which type of illumination patterns - regular, such as multi-spot and sinusoidal, or irregular, such as pseudo-random, - provide the best results. We model SIM imaging of a simulated resolution target, containing objects of various shapes and sizes. The quality of the simulated SIM images produced using different illumination types is compared in terms of the resolution, measured as the full width at half maximum (FWHM) of point-like objects, and SNR, measured in the bright uniform areas of the resolution target. The image reconstruction is performed using the pattern-illuminated Fourier Ptychography (piFP) algorithm. We identify the piFP algorithm as a steepest descent optimization of a quadratic function, and improve its convergence speed by introducing Newton-Raphson update coefficients. Finally, we compare experimental images of fixed cells and fluorescent beads acquired under multi-spot and pseudo-random illumination.

In **Chapter 4** we formulate the generalized maximum likelihood estimation (MLE)

treatment of the image reconstruction problem in SIM. This generalization can serve as an umbrella for all the SIM reconstruction algorithms that employ statistical noise models. We consider two particular cases: the piFP algorithm, derived assuming additive Gaussian noise distribution, and the joint Richardson-Lucy algorithm (jRL), derived from the Poisson noise distribution. By analyzing the development of the modulation transfer functions during the iterations of these algorithms we investigate the phenomenon of the non-uniform resolution improvement. The performance of the piFP and jRL algorithms is compared in simulations and experiments conducted on fixed cells.

In **Chapter 5** we suggest to use adaptive illumination patterns of the DMD to alleviate the photobleaching issue in SIM. In adaptive SIM we employ multi-spot illumination patterns and the piFP reconstruction algorithm. The illumination intensity is locally adjusted to the sample by applying grayscale masks to the illumination patterns. We consider several strategies for calculating the grayscale masks from a widefield image. The intensities in the grayscale mask are inversely proportional to the intensities in a widefield image, so the illumination dose is reduced at the expense of a lower SNR in bright areas of the sample. In this context, we quantify the degree of image deterioration in adaptive SIM. The performance of adaptive SIM is compared to standard SIM in time-lapse experiments.

A summary of the results and concluding remarks are given **Chapter 6**.

REFERENCES

- [1] E. K. Abbe, "Beiträge zur Theorie des Mikroskops und der mikroskopischen Wahrnehmung," *Archiv für Mikroskopische Anatomie* **5**, 413–468 (1873).
- [2] G. B. Airy, "On the diffraction of an object-glass with circular aperture," *Transactions of the Cambridge Philosophical Society* **5**, 283–292 (1835).
- [3] J. Huisken, J. Swoger, F. Del Bene, J. Wittbrodt, and E. H. Stelzer, "Optical sectioning deep inside live embryos by selective plane illumination microscopy," *Science* **305(5686)**, 1007–1009 (2004).
- [4] B. Bouma, *Handbook of optical coherence tomography* (Marcel Dekker, 2002).
- [5] D. Agard, Y. Hiraoka, P. Shaw, and J. Sedat, "Fluorescence microscopy in three dimensions," *Meth. Cell Biol.* **30**, 353–377 (1989).
- [6] P. J. Verveer, M. J. Gemkow, and T. M. Jovin, "A comparison of image restoration approaches applied to three-dimensional confocal and wide-field fluorescence microscopy," *J. Microsc.* **193**, 50–61 (1999).
- [7] W. Wallace, L. H. Schaefer, and J. R. Swedlow, "A workingperson's guide to deconvolution in light microscopy," *BioTechniques* **31**, 1076–1097 (2001).
- [8] P. Sarder and A. Nehorai, "Deconvolution methods for 3-D fluorescence microscopy images," *IEEE Trans. Signal Process.* **23**, 32–45 (2006).
- [9] M. Minsky, "Microscopy apparatus," US Patent **3013467**, 32–45 (1961).

- [10] J. White, W. B. Amos, and M. Fordham, "An evaluation of confocal versus conventional imaging of biological structures by fluorescence light microscopy," *J. Cell Biol.* **105**, 41–48 (1987).
- [11] J. Pawley, *Handbook of Biological Confocal Microscopy* (Springer US, 2010).
- [12] P. Shaw, "Comparison of Widefield/Deconvolution and Confocal Microscopy for Three-Dimensional Imaging," *Handbook of Biological Confocal Microscopy* **Chapter 23**, 453–467 (2010).
- [13] E. Betzig, G. H. Patterson, R. Sougrat, O. W. Lindwasser, S. Olenych, J. S. Bonifacino, M. W. Davidson, J. Lippincott-Schwartz, and H. F. Hess, "Imaging intracellular fluorescent proteins at nanometer resolution," *Science* **313**, 1642–1645 (2006).
- [14] M. J. Rust, M. Bates, and X. Zhuang, "Sub-diffraction-limit imaging by stochastic optical reconstruction microscopy (STORM)," *Nat. Methods* **3**, 793–795 (2006).
- [15] S. T. Hess, T. P. K. Girirajan, and M. D. Mason, "Ultra-high resolution imaging by fluorescence photoactivation localization microscopy," *Biophys. J.* **91**, 4258–4272 (2006).
- [16] S. W. Hell and J. Wichmann, "Breaking the diffraction resolution limit by stimulated emission: stimulated-emission-depletion fluorescence microscopy," *Opt. Lett.* **19**, 780–782 (1994).
- [17] R. Heintzmann and C. Cremer, "Laterally modulated excitation microscopy: improvement of resolution by using a diffraction grating," *Proc. SPIE* **3568**, 185–196 (1999).
- [18] M. G. L. Gustafsson, "Surpassing the lateral resolution limit by a factor of two using structured illumination microscopy," *J. Microsc.* **198**, 82–87 (2000).
- [19] J. T. Frohn, H. F. Knapp, and A. Stemmer, "True optical resolution beyond the Rayleigh limit achieved by standing wave illumination," *Proc. Natl. Acad. Sci. USA* **93**, 7232–7236 (2000).
- [20] G. E. Cragg and P. T. So, "Lateral resolution enhancement with standing evanescent waves," *Opt. Lett.* **25**, 46–48 (2000).
- [21] R. Heintzmann, T. M. Jovin, and C. Cremer, "Saturated patterned excitation microscopy—a concept for optical resolution improvement," *J. Opt. Soc. Am. A* **19**, 1599–1609 (2002).
- [22] R. Heintzmann, "Saturated patterned excitation microscopy with two-dimensional excitation patterns," *Micron* **34**, 283–291 (2003).
- [23] M. G. L. Gustafsson, "Nonlinear structured-illumination microscopy : Wide-field fluorescence imaging with theoretically unlimited resolution," *Proc. Natl. Acad. Sci. USA* **102**, 13081–13086 (2005).

- [24] S. Hari, "Resolution test target for optical nanoscopy," Delft University of Technology (in preparation).
- [25] R. Gräf, J. Rietdorf, and T. Zimmermann, "Live Cell Spinning Disk Microscopy," *Adv. Biochem. Eng./Biotechnol.* **95**, 57–75 (2005).
- [26] M. Liang, R. L. Stehr, and A. W. Krause, "Confocal pattern period in multiple-aperture confocal imaging systems with coherent illumination," *Opt. Lett.* **22**, 751–753 (1997).
- [27] P. J. Verveer, Q. S. Hanley, P. W. Verbeek, L. J. v. Vliet, and T. M. Jovin, "Theory of confocal fluorescence imaging in the programmable array microscope (PAM)," *J. Microsc.* **189**, 192–198 (1998).
- [28] Q. S. Hanley, P. J. Verveer, M. J. Gemkow, and T. M. Jovin, "An optical sectioning programmable array microscope implemented with a digital micromirror device," *J. Microsc.* **196**, 317–331 (1999).
- [29] R. Heintzmann, Q. Hanley, D. Arndt-Jovin, and T. Jovin, "A dual path programmable array microscope (PAM): simultaneous acquisition of conjugate and non-conjugate images," *J. Microsc.* **204**, 119–135 (2001).
- [30] M. Neil, R. Juškaitis, and T. Wilson, "Method of obtaining optical sectioning by using structured light in a conventional microscope," *Opt. Lett.* **22**, 1905–1907 (1997).
- [31] M. G. Somekh, C. W. See, and J. Goh, "Wide field amplitude and phase confocal microscope with speckle illumination," *Opt. Commun.* **174**, 75–80 (2000).
- [32] J. G. Walker, "Non-scanning confocal fluorescence microscopy using speckle illumination," *Opt. Commun.* **189**, 221–226 (2001).
- [33] C. Ventalon and J. Mertz, "Quasi-confocal fluorescence sectioning with dynamic speckle illumination," *Opt. Lett.* **30**, 3350–3352 (2005).
- [34] C. B. Muller and J. Enderlein, "Image Scanning Microscopy," *Phys. Rev. Lett.* **104**, 198101 (2010).
- [35] O. Schulz, C. Pieper, M. Clever, J. Pfaff, A. Ruhlandt, R. H. Kehlenbach, F. S. Wouters, J. Großhans, G. Bunt, and J. Enderlein, "Resolution doubling in fluorescence microscopy with confocal spinning-disk image scanning microscopy." *Proc. Natl. Acad. Sci. USA* **110**, 21000–21005 (2013).
- [36] A. G. York, S. H. Parekh, D. Dalle Nogare, R. S. Fischer, K. Temprine, M. Mione, A. B. Chitnis, C. A. Combs, and H. Shroff, "Resolution doubling in live, multicellular organisms via multifocal structured illumination microscopy," *Nat. Methods* **9**, 749–754 (2012).
- [37] G. M. R. De Luca, R. M. P. Breedijk, R. Brandt, C. H. C. Zeelenberg, B. E. de Jong, W. Timmermans, L. N. Azar, R. Hoebe, S. Stallinga, and E. M. M. Manders, "Re-scan confocal microscopy: scanning twice for better resolution." *Biomed. Opt. Express* **4**, 2644–2656 (2013).

- [38] S. Roth, C. J. Sheppard, K. Wicker, and R. Heintzmann, “Optical photon reassignment microscopy (OPRA),” *Optical Nanoscopy* **2**, 1–6 (2013).
- [39] A. G. York, P. Chandris, D. D. Nogare, J. Head, P. Wawrzusin, R. S. Fischer, A. Chitnis, and H. Shroff, “Instant super-resolution imaging in live cells and embryos via analog image processing.” *Nat. Methods* **10**, 1122–1126 (2013).
- [40] S. A. Shroff, J. R. Fienup, and D. R. Williams, “Phase-shift estimation in sinusoidally illuminated images for lateral superresolution,” *J. Opt. Soc. Am. A* **26**, 413–424 (2009).
- [41] P. Křížek, I. Raška, and G. M. Hagen, “Flexible structured illumination microscope with a programmable illumination array,” *Opt. Express* **20**, 24585–24599 (2012).
- [42] D. Dan, M. Lei, B. Yao, W. Wang, M. Winterhalder, A. Zumbusch, Y. Qi, L. Xia, S. Yan, Y. Yang, P. Gao, T. Ye, and W. Zhao, “DMD-based LED-illumination Super-resolution and optical sectioning microscopy,” *Sci. Rep.* **3**, 1116 (2013).
- [43] E. Mudry, K. Belkebir, J. Girard, J. Savatier, E. Le Moal, C. Nicoletti, M. Allain, and A. Sentenac, “Structured illumination microscopy using unknown speckle patterns,” *Nature Photon.* **6**, 312–315 (2012).
- [44] F. Orieux, E. Sepulveda, V. Lorient, B. Dubertret, and J. C. Olivo-Marin, “Bayesian estimation for optimized structured illumination microscopy,” *IEEE Trans. Image Process.* **21**, 601–614 (2012).
- [45] T. Lukeš, P. Křížek, Z. Švindrych, J. Benda, M. Ovesný, K. Fliegel, M. Klíma, and G. M. Hagen, “Three-dimensional super-resolution structured illumination microscopy with maximum a posteriori probability image estimation,” *Opt. Express* **22**, 29805–29817 (2014).
- [46] C. H. Righolt, J. A. Slotman, I. T. Young, S. Mai, L. J. van Vliet, and S. Stallinga, “Image filtering in structured illumination microscopy using the Lukosz bound,” *Opt. Express* **21**, 24431–24451 (2013).
- [47] L. H. Schaefer, D. Schuster, and J. Schaffer, “Structured illumination microscopy: artefact analysis and reduction utilizing a parameter optimization approach,” *J. Microsc.* **216**, 165–174 (2004).

2


DEVELOPMENT OF A DMD-BASED FLUORESCENCE MICROSCOPE

We present a versatile fluorescence microscope, built by complementing a conventional fluorescence microscope with a digital micro-mirror device (DMD) in the illumination path. Arbitrary patterns can be created on the DMD and projected onto the sample. This patterned illumination can be used to improve lateral and axial resolution over the resolution of a wide-field microscope, as well as to reduce the illumination dose. Different illumination patterns require different reconstruction strategies and result in an image quality similar to confocal or structured illumination microscopy. We focus on the optical design and characterization of a DMD-based microscope. Estimation of the optical quality of the microscope has been carried out by measuring the modulation transfer function from edge profiles. We have obtained optically sectioned images by applying multi-spot illumination patterns followed by digital pinholing. The sectioning capabilities of our DMD-based microscope were estimated from the dependence of the signal-to-background and signal-to-noise ratios on the pitch of the projected multi-spot patterns and the size of the digital pinhole. In addition, we provide an outlook on the use of pseudo-random illumination patterns for achieving both sectioning and resolution enhancement.

Parts of this chapter have been published as N. Chakrova, B. Rieger, and S. Stallinga, Proc. SPIE **9330**, 933008 (2015) [1].

2.1. INTRODUCTION

FLUORESCENCE microscopy serves biologists as an imaging technique for studying intracellular processes and structures. However, it is well known, that the resolution of a standard wide-field microscope is limited by diffraction and the smallest resolved periodical structure is defined by Abbe's formula as $\lambda/2NA$, where λ is the wavelength and NA is the numerical aperture of the objective lens. In the last two decades, attempts to overcome this resolution limit led to various fluorescence microscopy techniques, providing lateral resolutions in the range of 20-150 nm and axial resolutions in the range of 100-700 nm (see Ref. [2] for an overview). Unfortunately, none of these methods is universal and an appropriate technique has to be chosen for each particular application to achieve the desired trade-off between the resolution improvement, signal-to-noise ratio, imaging time and photo-bleaching.

In fluorescence microscopy, non-uniform illumination can be used to improve lateral resolution, provide sectioning and reduce the illumination dose. Most prominent examples of the microscopy techniques that utilize non-uniform illumination are confocal microscopy [3] and structured-illumination microscopy (SIM) [4–8]. In confocal microscopy, sectioning is achieved by using point illumination and detection. The speed of image acquisition can be increased by using parallel scanning techniques, such as spinning disk microscopy. In SIM periodic line patterns are used to double the resolution, which are created by the interference of two or three laser beams in the sample plane. The final image has to be reconstructed from several images acquired at different positions and orientations of the line pattern. Apart from point illumination and periodic line pattern illumination, sequences of pseudo-random patterns have been studied in spinning disk systems to address the problem of inefficient use of the available illumination light [9]. 

The use of spatial light modulators, such as liquid crystal-on-silicon (LCOS) microdisplays or digital micro-mirror devices (DMD) provides spatial and temporal control over the illumination patterns and allows to combine all the mentioned patterned illumination techniques in one setup. Such a microscope is expected to produce images with a quality similar to confocal or SIM microscopy, depending on the type of projected illumination pattern. Moreover, spatial light modulators can be used to reduce the illumination dose by controlling the illumination pattern pixel by pixel [10]. Together with improvements in LCOS and DMD technologies, a number of DMD-based and LCOS-based microscopes were developed [11–17]. Although the performance of the DMD-based and LCOS-based microscopes is very similar, we consider the use of the DMD advantageous, due to its higher switching speed and higher contrast over a larger spectral range.

In the following sections we focus on the optical design and characterization of DMD-based microscopes. We first study the DMD operation and estimate the optical quality of the microscope by measuring its modulation transfer function (MTF). Next, we present the examples of sectioned images, produced by projecting the multi-spot patterns onto the sample, and estimate the sectioning by measuring signal-to-background and signal-to-noise ratios. In conclusion, we give an outlook on the use of pseudo-random illumination patterns for achieving both sectioning and resolution enhancement.

2.2. EXPERIMENTAL METHODS

2.2.1. DIGITAL MICRO-MIRROR DEVICE OPERATION

A digital micro-mirror device (DLP discovery 4100 chip set, Texas Instruments, TX, USA) consists of an array of 1024×768 square micro-mirrors with a pitch of $13.68 \mu\text{m}$ and the physical size of the mirror somewhat less due to the fill factor of 91%. Each micro-mirror can be tilted along its diagonal to occupy one of two positions: $+12^\circ$ tilt to direct the incident beam into the optical path, -12° tilt to deflect the incident beam away from the optical path. Each pixel of the DMD is addressed separately, thus providing the possibility to create arbitrary illumination patterns. Since the mirrors of the DMD tilt along their diagonals, the DMD chip is rotated 45° in order to keep both incident and reflected beams in one plane, parallel to the optical table. The DMD is controlled by the ALP-4.2 Controller Suite (Vialux, Chemnitz, Germany), which is a hardware, firmware and software package, that allows for a 22 kHz switching rate of the binary patterns.

Particular diffraction characteristics of the DMD have to be understood prior to optimal use of this device in an imaging system. The pixelated structure of the DMD is essentially a two-dimensional blazed diffraction grating with pitch $d = d_{DMD}/\sqrt{2}$ and a facet tilt angle of $\theta = 12^\circ$. In a blazed grating, intensity of the diffracted light for wavelength λ is distributed among m diffraction orders with angles $\beta_m = \arcsin(m\lambda/d) + \alpha$, where α is the angle of incidence. The center of the intensity distribution follows the reflection from a single DMD pixel and is not coupled with the 0-diffraction order, which follows specular reflection from the surface of the DMD [18]. Situation, when the center of intensity distribution aligns with one of the diffraction orders, is called the blaze condition and the corresponding order – the blazed order. The blazed order m_B receives most of the diffraction intensity. In case of normal incidence ($\alpha = 0^\circ$) the blaze condition is fulfilled when $\beta_m = 2\theta$. For given incidence angle and grating parameters each diffraction order can be at blaze condition for only one wavelength. Table 2.1 shows the blazed orders and the corresponding blazed wavelengths in case of the normal incidence for the DMD used in this work.

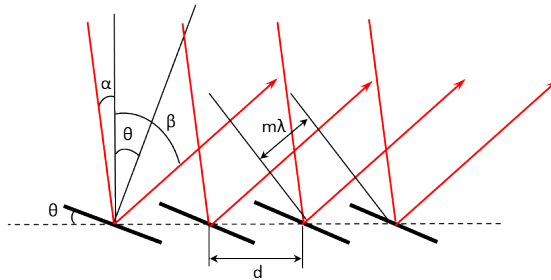


Figure 2.1: Illustration of the blazing condition. The blaze condition is fulfilled when one of the diffraction angles equals the angle of specular reflection from a single DMD pixel: $\beta = \alpha + 2\theta$. In case of normal incidence $\alpha = 0^\circ$, $\beta = 2\theta$.

In the general case, the illumination wavelength does not satisfy the blazed grating condition and diffracted light from the DMD is not parallel to the optical axis [19]. Fig. 2.2 shows this effect for a few typical laser wavelengths. The top row presents simulated

Table 2.1: Blazed orders and corresponding wavelengths in case of the normal incidence.

Blazed order	$FWHM$ nm
6	656
7	562
8	492
9	437
10	394

diffraction intensities at the conjugate pupil plane of the microscope. The simulation is based on the mathematical description of the diffraction amplitude at the DMD given in reference [20]. The bottom row shows images of the DMD diffraction patterns, projected on a white screen, taken with a digital consumer camera. Small white circles in the top row and small black circles in the bottom row represent typical numerical aperture at the image plane of the microscope $NA = 0.012$. One can notice, that without taking additional measures, some wavelengths will not be transmitted through the light path of the microscope with such an NA. The angle of incidence of the illumination beam has to be tuned to match the blazed grating condition for a specific wavelength. In case an addi-

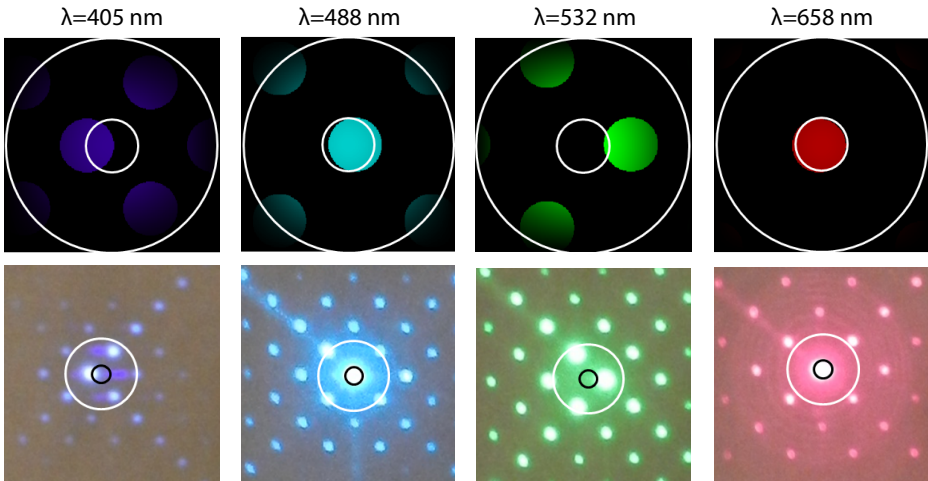


Figure 2.2: Simulated (top row) and imaged (bottom row) diffraction intensities at the conjugate pupil plane of the microscope for different wavelengths. Small white circles in the top row and small black circles in the bottom row represent typical numerical aperture at the image plane of the microscope $NA = 0.012$. Large white circles in the top and bottom rows represent increased numerical aperture $NA = 0.05$.

tional, identical DMD is also used at the detection side, tuning of the incidence angle to achieve blazed condition is not possible, as excitation and emission wavelengths differ due to the Stokes shift. One of the solutions to this problem is to increase the numerical aperture of the relay optics between the DMD and camera in order to capture enough light even in the off-blaze condition [19]. To estimate the required NA, we refer again to the mathematical description of the diffraction amplitude at the DMD. In the off-blaze

case, each of the four closest diffraction orders receives $16/\pi^4 \approx 16\%$ of the diffracted light intensity. Ensuring that at least these closest diffraction orders in the off-blaze case are captured guarantees a total light efficiency of 64% or higher for any wavelength. In practice, that means increasing the NA 4 times in comparison to the typical values of NA in the microscope's image plane. Large white circles in Fig. 2 represent this increased numerical aperture $NA = 0.05$.

In this work we have used a DMD only at the illumination side and tuned the incidence angle of the diode laser beam with 488 nm wavelength to meet the blazing condition. A pinhole placed in the Fourier plane of the DMD blocks all the diffraction orders except for the central one, in order to avoid diffraction induced distortions of the illumination pattern.

We have observed a mismatch in the intensities of the modelled and imaged diffraction patterns. Particularly, intensities of the diffraction spots in the imaged patterns exhibit top-bottom asymmetry, which is not predicted by the theory. We have not identified the reason for this asymmetry, however, we note that it was persistent with changes in polarization and alignment.

2.2.2. SETUP LAYOUT

A DMD-based fluorescence microscope is built on the basis of an inverted Olympus IX71 microscope. The DMD is placed in a plane conjugate to the image plane of the microscope. The lens relay from the DMD to the microscope image plane is made from two achromatic doublets and has a magnification of $1.66\times$. Using a $100\times$ oil immersion objective each DMD pixel of $13.68 \times 13.68 \mu\text{m}$ is demagnified $1.66 \times 100 = 166$ times down to 83×83 nm in the sample plane. The DMD is illuminated by a 100 mW diode laser source with 488 nm wavelength (Coherent Inc., CA, USA). The laser beam is first despeckled by a rotating diffuser (SUSS MicroOptics, Switzerland) and expanded to the size that covers the full area of the DMD. The expanded and despeckled laser beam is then directed to the DMD at an angle that matches the blazed grating condition of the DMD for 488 nm wavelength. The U-MWIB2 Olympus filter cube with ET535/50M dichroic mirror, which is used to separate the excitation and emission bands, is placed between the tube lens and the image plane. Placing the filter cube outside of the parallel light path is generally avoided in microscopy, since it can introduce additional distortions to the optical system. In our case the filter cube is placed outside of the parallel path to enable the design where both excitation and emission beams pass through the side port of the microscope. Fluorescence from the sample is imaged by an sCMOS camera (Hamamatsu Photonics, Hamamatsu City, Japan) placed at the image plane of the microscope. The optical layout of the experimental setup is given in Fig. 2. In order to provide proper sampling, two Nyquist criteria have to be satisfied – Nyquist sampling by the DMD is achieved if condition (1) is fulfilled, and Nyquist sampling by the camera is achieved if condition (2) is fulfilled:

$$d_{DMD} \leq \lambda_{ex}/4NA, \quad (2.1)$$

$$d_{sCMOS} \leq \lambda_{em}/4NA. \quad (2.2)$$

If a $100\times$ objective with $NA = 1.3$ is used, the required DMD pixel size in the object plane equals 94 nm and the required sCMOS pixel size equals 100 nm, assuming a Stokes

shift to 518 nm. Hence, the actual DMD pixel size of 83 nm and the actual sCMOS pixel size of 65 nm provide slight oversampling of the object plane.

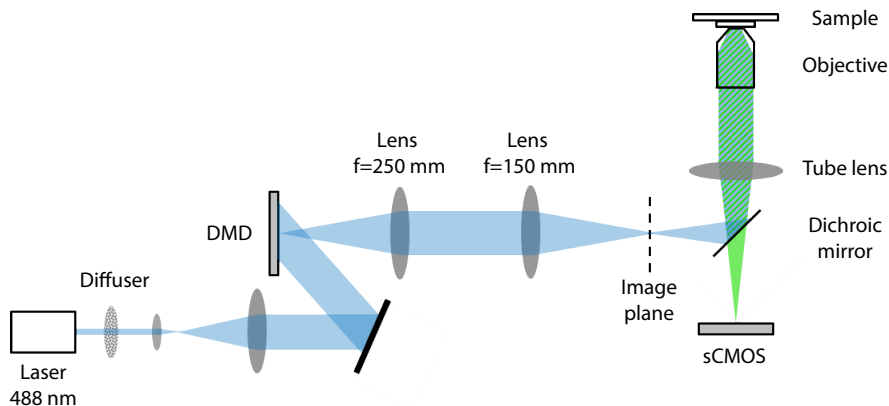


Figure 2.3: Schematic view of the setup. The DMD is illuminated by the expanded and despeckled 488 nm laser beam. The pattern of the DMD is projected into the image plane via a $1.66\times$ lens relay and further into the sample plane via the tube lens and the objective of the microscope. Fluorescence of the sample passes through the dichroic mirror and is imaged by the sCMOS camera.

2.2.3. SAMPLES

A thin fluorescent layer was used for the calibration of the system by edge profile and noise measurements and flat field images. The layer is ca. 110 nm thick and exhibits high spatial fluorescence homogeneity. The layer was originally developed to characterize the image quality in sectioning microscopy and is produced as described in Ref. [21]. Multi-spot scans were applied to the bovine pulmonary artery endothelial (BPAE) cells (Life Technologies, CA, USA), in which F-actin is stained with Alexa Fluor 488 phalloidin.

2.3. OPTICAL QUALITY ASSESSMENT

2.3.1. ESTIMATING THE MTF BY THE EDGE-PROFILE MEASUREMENT METHOD

ONE of the ways to estimate the resolution of an optical system is to measure its Modulation Transfer Function (MTF). In order to estimate the MTF, we have performed edge-profile measurements (see Fig.3 and Ref. [22]). First, a sharp edge pattern was created on the DMD by switching half of the pixels in the “on”-state and another half in the “off”-state. The edge patterns were projected into the thin, homogeneously fluorescent layer as described above, and the images were captured by the sCMOS camera. The image of the edge on the camera is the Edge Spread Function (ESF) – the two-dimensional convolution of the edge-source object with the excitation and emission PSF of the system. The camera and the DMD are precisely aligned in such a way that the DMD edge is strictly vertical or strictly horizontal with respect to the camera chip. The edge profile was calculated from an average of 10 images. After dark-field and flat-field correction, we averaged the resulting image over several hundreds of camera rows to extract the vertical

edge or over several hundreds of columns to extract the horizontal edge. The obtained edge profile is a one-dimensional projection of the ESF. Next, the ESF was differentiated in order to get the one-dimensional projection of the Line Spread Function (LSF). Finally, the MTF curve was found as the Fourier transform of the LSF.

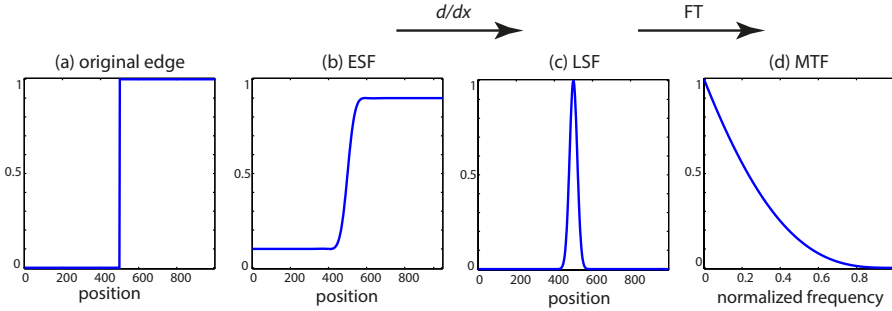


Figure 2.4: Estimation of the MTF from the edge-profile measurement. a) Original sharp edge b) Edge Spread Function c) Line-Spread Function d) Modulation Transfer Function.

In order to reduce the noise in the MTF curves, the following procedure was applied. The edge profile was upsampled by a factor of 8 using spline interpolation. Noise on the high and low plateaus of the edge profile was reduced by calculating a moving average over a varying window. After differentiation by finite differences, the LSF was downsampled back to its original rate and the zero level of the LSF was further smoothed down by applying the moving average over a varying window.

2.3.2. THEORETICAL MTF CURVES

The MTF of an incoherent optical system can be calculated as the normalized autocorrelation of the exit pupil of the system. In case of a circular aperture the MTF is of the form:

$$MTF\left(\frac{f}{f_{cutoff}}\right) = \frac{2}{\pi} \left(\cos^{-1}\left(\frac{f}{f_{cutoff}}\right) - \left(\frac{f}{f_{cutoff}}\right) \sqrt{1 - \left(\frac{f}{f_{cutoff}}\right)^2} \right), \quad (2.3)$$

where the cutoff frequency $f_{cutoff} = 2NA/\lambda$, is the highest frequency transmitted by the diffraction-limited system with numerical aperture NA for a given wavelength λ , and $f \in [0, f_{cutoff}]$ [23].

In our experiment, a sharp edge is created as a pattern on the DMD and projected into the thin fluorescent layer by the microscope objective. The projected edge is then imaged on the sCMOS camera by the same microscope objective. Since we are imaging not the sharp edge directly, but the image of this edge, each point of the original edge is blurred twice by passing twice through the optical path. Hence, the MTF given by formula 4.3 has to be squared in order to correctly represent the expected optical MTF. The MTF of the camera is found as a Fourier transform of the camera pixel. The pixel shape is represented by the rectangle function and its Fourier transform - by the *sinc* function:

$$MTF_{camera} = \text{sinc}(\pi a f), \quad (2.4)$$

with a the pixel size of the camera in the sample plane. The final theoretical MTF is calculated as a product of the optical MTF and camera MTF.

2.3.3. COMPARISON OF THE EXPERIMENTAL AND THEORETICAL MTF CURVES

MTF curves were measured for two objectives: 10× air objective with NA = 0.25 and 100× oil immersion objective with NA = 1.3. We have imaged vertical and horizontal edges of two types. Owing to the structure of the DMD, edges of type 1 are formed by neighboring pixels at an angle of 156° and edges of type 2 are formed by neighboring pixels at an angle of 204° (Fig.2.5). This difference in the geometrical structure of the edges influences the edge profiles of the system and results in different MTF curves for different edge types.

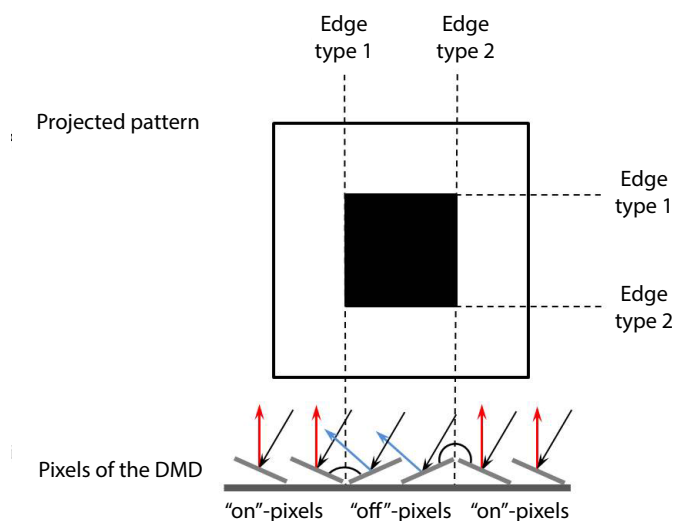



Figure 2.5: The edges formed by the DMD. Black arrows indicate the incident light, red arrows – light reflected by the pixels in the “on” state, blue arrows – light, reflected by the pixels in the “off” state.

Measured MTF curves for the 10× objective correspond well to the theoretical MTFs, which indicates that the microscope performance is close to diffraction-limited in this case (Fig.2.6). High NA objectives are more complex and are more sensitive to misalignments in the system. The measured MTF curves for the 100× oil immersion objective are also sensitive to the edge type, as can be seen from Fig.2.7. Edge type 1 results in higher values for the MTF than edge type 2. The difference in the MTF curves is the result of the difference in the geometrical structure of the edges at the DMD per se. Noteworthy, this difference is not prominent in the MTF curves for the low NA objective.

We have measured the MTF with an alternative method in order to avoid this edge-type sensitivity in the MTF curves. Horizontal and vertical lines with a thickness of a single DMD pixel where projected into the sample. Images of these projections correspond to the LSF profiles. Taking the Fourier transform of the LSF results in an edge-type independent MTF measurement, as shown in Fig.2.7. 

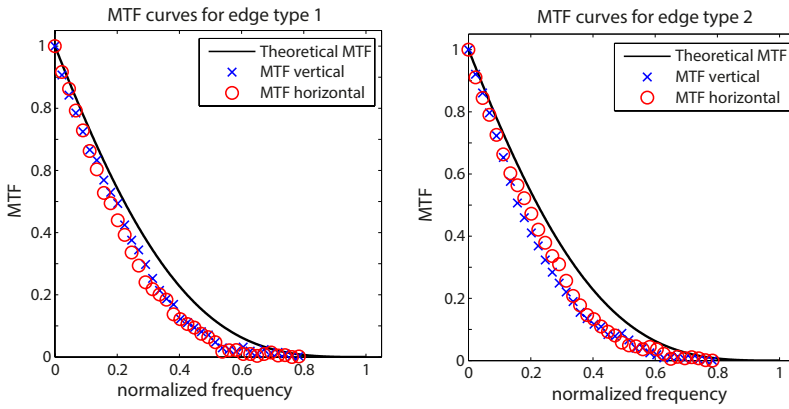


Figure 2.6: The MTF curves for 10× objective with NA = 0.25 indicate that the microscope performance is close to diffraction-limited. The spatial frequency is normalized to the cutoff spatial frequency $f_{cutoff} = 2NA/\lambda$.

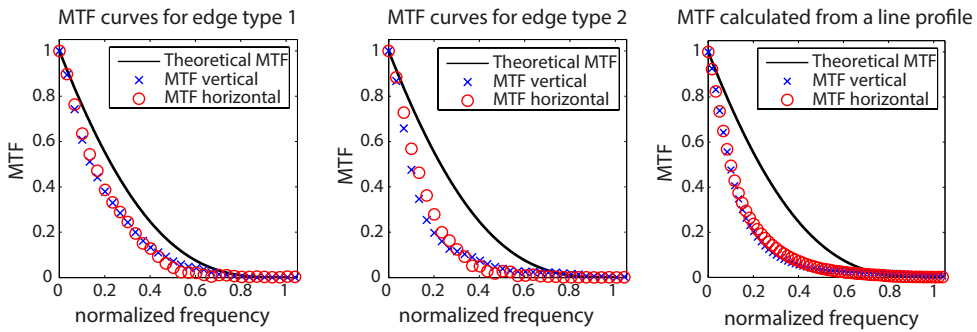


Figure 2.7: The MTF curves for 100× objective with NA = 1.3. Edge type 1 results in higher MTF values than edge type 2. The MTF profiles differ due to the difference in the edges of the DMD per se. MTF curve calculated from a line profile shows an edge-independent MTF measurement.

2.4. MAPPING THE DMD TO THE CAMERA

EACH pixel of the DMD that is projected into the sample, appears as a blurred spot in the raw camera image. In order to apply reconstruction algorithms, we have to establish the correspondence between each DMD-pixel and its image on the camera. To create a precise mapping of the DMD pixels onto the camera grid, we apply the following procedure. A calibration image is taken by projecting a multi-spot DMD pattern into a thin, homogeneously fluorescent layer. The multi-spot pattern is created as an array of switched “on” DMD pixels, arranged in a square grid with pitch p . The square with the side that equals the pitch size of the projected grid is called the unit cell. Assuming that the unit cells which are closest to the optical axis are not distorted in the camera image, we find the unit cell vector c as best fitting vector (in the least squares sense) to the 6×6 central unit cells. The square grid with the pitch size of the unit cell vector is the grid of expected spot positions of the DMD-pixels in the camera (x_c, y_c). Actual spot positions deviate from this grid of expected positions due to distortions in the system. This deviation increases with increasing distance from the optical axis. The actual spot positions (x'_c, y'_c) are found with subpixel precision as local maxima in the neighbourhoods of the expected spots positions (x_c, y_c). In order to find the coordinates of all the remaining pixels of the DMD in the camera plane, the found positions of the actual spots of the square grid have to be translated $p^2 - 1$ times with the step that equals c/p . Thus, each DMD pixel (x_{DMD}, y_{DMD}) is mapped on the camera grid with subpixel precision as (x'_c, y'_c). An example of the spot detection in a calibration image is given in Fig.2.8.

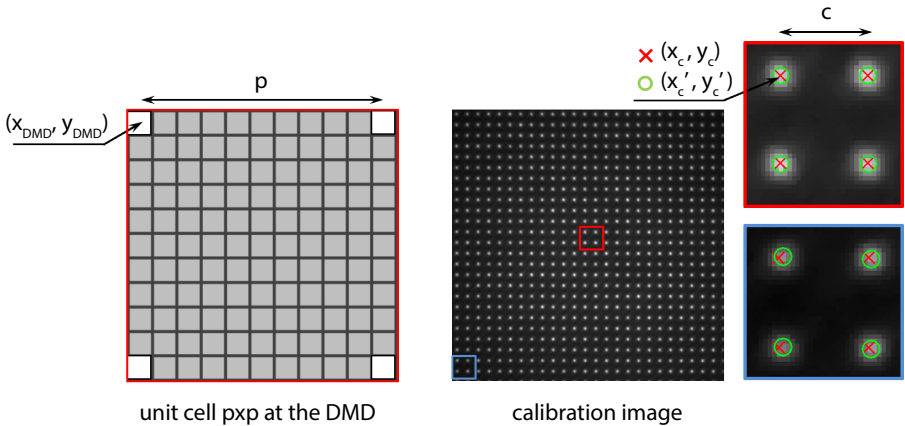


Figure 2.8: Mapping of the DMD to the camera is performed by detecting the illumination spots in the calibration image. Each DMD pixel (x_{DMD}, y_{DMD}) is mapped onto the camera grid with subpixel precision as (x'_c, y'_c).

The deviation of the actual spots from the expected spots provides valuable information about distortions that are present in the system. For our reconstruction procedure we have used the part of the image field of view (FOV) where the actual spot positions deviated from the expected spot positions by less than 1.5 camera pixels. Such a FOV typically amounts to approximately 800×800 camera pixels, which corresponds to an

area of $52\ \mu\text{m} \times 52\ \mu\text{m}$ in the sample plane if a $100\times$ oil immersion objective is used.

2.5. MULTI-SPOT ILLUMINATION RESULTS

WE obtained optically sectioned images by projecting multi-spot patterns onto the sample and applying digital pinholing to the raw images. First, a square grid pattern with pitch p is projected onto the sample. To illuminate the sample homogeneously, the pattern is translated $p^2 - 1$ times with a translation step of one DMD pixel. A camera image is taken for each pattern translation, so that in total p^2 camera frames are collected. After dark field and flat field correction, we apply digital pinholing for each raw camera frame to suppress the out-of-focus light. Digital pinholing is performed by detecting the spots in each camera frame and multiplying each of the spots with a 2D Gaussian mask with standard deviation σ . The value of σ controls the strength of the sectioning effect as will be shown later in this section. For each Gaussian spot, the intensities of all the pixels falling within a spot are summed up, and the resulting intensity value is assigned to the corresponding DMD pixel. In this way, each raw camera image is converted into an image that has the number of pixels of the DMD chip. Accurate mapping of the DMD to the camera is essential to perform this step. After the pinholing, p^2 converted images are summed up to build an optically sectioned image. A comparison of such an image with a standard wide-field image is given in Fig.2.9.

Two main parameters influencing the sectioning capabilities of a DMD-based microscope for a given objective are the pitch p of the projected pattern and the pinholing Gaussian mask width σ . By changing the pitch we are changing the trade-off between the speed of image acquisition, which is given by the number of needed raw frames, and the sectioning strength (Fig.2.10a, 2.11). The optimal pitch should provide the smallest number of raw images without compromising the sectioning quality. For the parameters of our setup, $p = 12 - 16$ DMD pixels proved to be sufficient to this end. Smaller pinhole separations result in a significant crosstalk between the pinholes and hamper the detection of the individual illumination spots, which results in artefacts in the reconstructed image. Larger pinhole separations increase the imaging time without providing substantially better sectioning. The sectioning effect can be assessed by the background level in the reconstructed images, since a better sectioning results in a higher signal-to-background ratio (SBR). The SBR was estimated by analysing the images of the BPAE cells, reconstructed after the multi-spot illumination. We have estimated the signal as the mean of the 1% highest intensity pixels and the background as the mean of the background area. The resulting SBR in the reconstructed image with $p = 16$ DMD pixels is approximately 6 times higher than the SBR in the widefield image. By squeezing the digital pinhole parameter σ we enhance the sectioning, but at the same time reduce the signal-to-noise ratio (SNR) (Fig.2.10b, 2.11). The SBR was estimated in the same manner as previously. The SNR was measured by analysing images of the thin homogeneously fluorescent layer. After dark field and flat field correction, the signal was measured as the mean intensity of the image, and the noise as the standard deviation of the intensity in the image. In confocal microscopy the size of the digital pinhole is usually set as the diameter of the first dark ring of the Airy pattern d_{Airy} . A Gaussian profile corresponding to the Airy pattern with $d_{\text{Airy}} = 1.22\lambda/NA$ has a standard deviation $\sigma \approx 0.45\lambda/2NA \approx 85$ nm for the given objective. Horizontal lines in Fig.2.10 correspond to the SBR and SNR

in a widefield image. The illumination dose used for the widefield image was approximately 10 times lower than the total illumination dose that was used for the multi-spot scan. Therefore, the SNR of the widefield image was scaled by the factor of $\sqrt{10}$ in order to compare the widefield and the reconstructed images at equal illumination doses in Fig.2.10b.

2

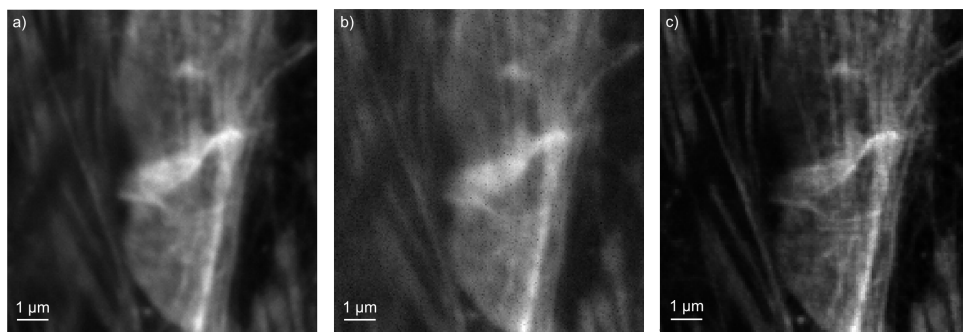


Figure 2.9: Images of BPAE cells stained with phalloidin conjugated to Alexa Fluor 488, acquired with a $100\times/1.3$ objective. a) Widefield image b) The sum of p^2 frames acquired at all scanning positions of the multi-spot illumination. Without the digital pinholing, the image resembles the widefield image, but displays higher noise level due to the pixel-dependent gain and noise of the sCMOS camera. c) Optically sectioned image reconstructed from the multi-spot illumination by applying digital pinholing.

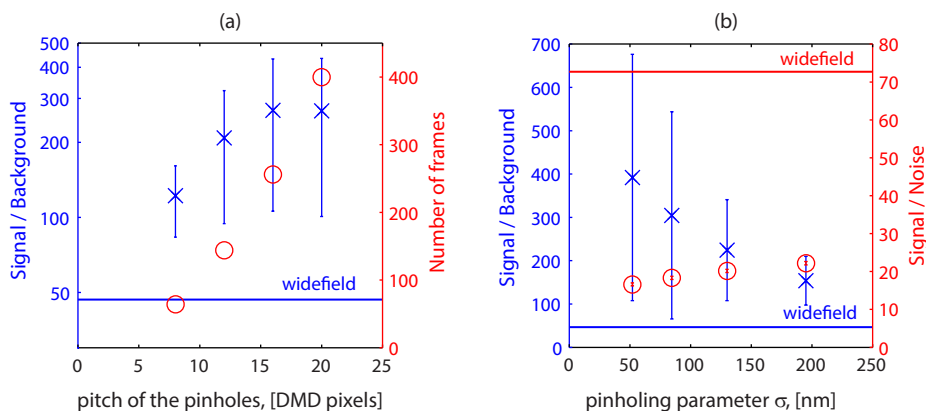


Figure 2.10: Sectioning capabilities of the DMD-based multi-spot scanning microscope depending on the pitch size (a) and the pinholing parameter σ (b). a) The sectioning effect can be improved by increasing the pitch of the projected multi-spot pattern. However, the number of frames required and the image acquisition time depend quadratically on the pitch. A pitch of 12-16 DMD pixels provides a reasonable compromise between sectioning and image acquisition time. The horizontal line indicates the SBR in a widefield image. b) By decreasing the digital pinhole parameter σ we enhance the sectioning on the one hand and deteriorate the SNR on the other hand. The optimal value $\sigma \approx 85$ nm corresponds to the pinhole size equal to the first dark ring of the Airy pattern. Horizontal lines indicate the SBR and SNR in a widefield image.

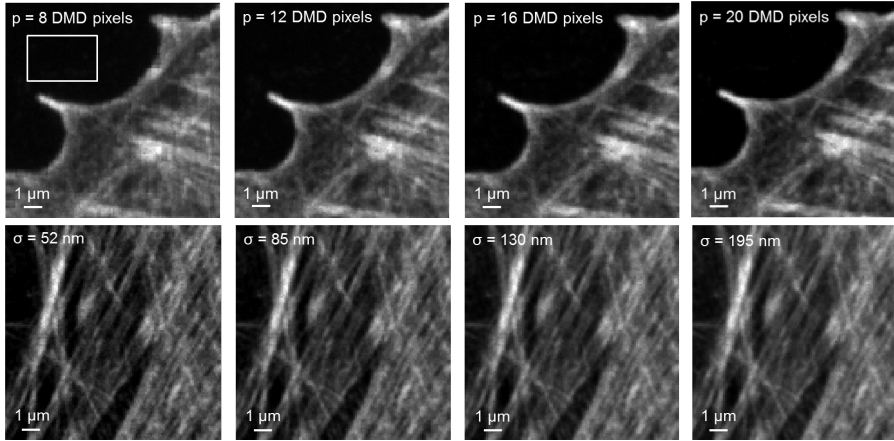


Figure 2.11: Top row: comparison of the images reconstructed using different values of the pinhole parameter σ . The images are acquired with the optimal value of the pitch $p = 16$ DMD pixels, and are displayed with linearly stretched contrast, since there is a large difference in the intensities of the images reconstructed using different σ values. The sectioning effect is enhanced with decreasing pinhole parameter σ . Bottom row: comparison of the images acquired with different pitch values p . The images are reconstructed using the optimal pinhole parameter $\sigma = 85$ nm and have the same contrast stretching. A small pinhole separation $p = 8$ DMD pixels results in artefacts in the reconstructed image. A pinhole separation of 12-16 DMD pixels provides optimal results. Further increase of the pitch size leads only to a minor sectioning improvement. The sectioning strength was assessed by the SBR in each image. The signal was estimated as the mean of the 1% highest intensity pixels and the background as the mean of the background area, which is shown as a white box in the bottom-left image.

2.6. OUTLOOK ON THE USE OF PSEUDO-RANDOM PATTERNS

PSEUDO-RANDOM sequences were first applied in a spinning disk microscope in 1996 by Juškaitis et al. [9] to address the issue of inefficient use of the available illumination light in confocal microscopy. Similar types of patterns have been later applied in dual-pass DMD-based microscopes [13, 24]. In both spinning disk and DMD-based microscopes the sectioning effect was obtained by illuminating the sample through the aperture mask and detecting the fluorescence light through the same aperture mask (dual-pass setup). The use of pseudo-random patterns in a single-pass configuration with wide-field detection is not straightforward, since it requires more elaborate reconstruction algorithms to retrieve a sectioned image. This is even more complicated when improved lateral resolution, as in SIM, is required. Nonetheless, this option might be advantageous over a dual-pass setup due to the simplified optical implementation. To our knowledge, pseudo-random patterns have not been applied in a single-pass DMD-based microscopes with widefield detection up to date. However, the improvement of lateral resolution by applying speckle illumination was recently demonstrated [25, 26], and optical sectioning with speckle illumination and widefield detection was obtained as well [27]. In case of speckle illumination the information about the illuminating patterns is not available, which leads to computationally demanding reconstruction algorithms and, hence, relatively slow reconstructions. We are aiming to apply pseudo-random il-

lumination patterns in a single-pass DMD-based microscope for both sectioning and lateral resolution improvement. A priori knowledge of the illumination patterns is expected to simplify and speed up the reconstruction. Furthermore, the DMD patterns can be designed in such a way that their sum results in a homogeneous intensity distribution, which is expected to reduce the overall noise level.

REFERENCES

- [1] N. Chakrova, B. Rieger, and S. Stallinga, "Development of a DMD-based fluorescence microscope," *Proc. SPIE* **9330**, 933008 (2015).
- [2] L. Schermelleh, R. Heintzmann, and H. Leonhardt, "A guide to super-resolution fluorescence microscopy," *J. Cell Biol.* **190**, 165–175 (2010).
- [3] J. Pawley, *Handbook of Biological Confocal Microscopy* (Springer US, 2010).
- [4] M. G. L. Gustafsson, "Surpassing the lateral resolution limit by a factor of two using structured illumination microscopy," *J. Microsc.* **198**, 82–87 (2000).
- [5] R. Heintzmann and C. Cremer, "Laterally modulated excitation microscopy: improvement of resolution by using a diffraction grating," *Proc. SPIE* **3568**, 185–196 (1999).
- [6] J. T. Frohn, H. F. Knapp, and A. Stemmer, "True optical resolution beyond the Rayleigh limit achieved by standing wave illumination," *Proc. Natl. Acad. Sci. USA* **93**, 7232–7236 (2000).
- [7] G. E. Cragg and P. T. So, "Lateral resolution enhancement with standing evanescent waves," *Opt. Lett.* **25**, 46–48 (2000).
- [8] M. G. L. Gustafsson, L. Shao, P. M. Carlton, C. J. R. Wang, I. N. Golubovskaya, W. Z. Cande, A. D. Agard, and J. W. Sedat, "Three-dimensional desolution doubling in wide-field fluorescence microscopy by structured illumination," *Biophys. J.* **94**, 4957–4970 (2008).
- [9] R. Juskaitis, T. Wilson, M. A. A. Neil, and M. Kozubek, "Efficient real-time confocal microscopy with white light sources," *Nature* **383**, 804–806 (1996).
- [10] W. Caarls, B. Rieger, A. H. B. De Vries, D. J. Arndt-Jovin, and T. M. Jovin, "Minimizing light exposure with the programmable array microscope," *J. Microsc.* **241**, 101–110 (2011).
- [11] M. Liang, R. L. Stehr, and A. W. Krause, "Confocal pattern period in multiple-aperture confocal imaging systems with coherent illumination," *Opt. Lett.* **22**, 751–753 (1997).
- [12] Q. S. Hanley, P. J. Verveer, M. J. Gemkow, and T. M. Jovin, "An optical sectioning programmable array microscope implemented with a digital micromirror device," *J. Microsc.* **196**, 317–331 (1999).

- [13] R. Heintzmann, Q. Hanley, D. Arndt-Jovin, and T. Jovin, "A dual path programmable array microscope (PAM): simultaneous acquisition of conjugate and non-conjugate images," *J. Microsc.* **204**, 119–135 (2001).
- [14] P. J. Verveer, Q. S. Hanley, P. W. Verbeek, L. J. v. Vliet, and T. M. Jovin, "Theory of confocal fluorescence imaging in the programmable array microscope (PAM)," *J. Microsc.* **189**, 192–198 (1998).
- [15] P. Křížek, I. Raška, and G. M. Hagen, "Flexible structured illumination microscope with a programmable illumination array," *Opt. Express* **20**, 24585–24599 (2012).
- [16] A. G. York, S. H. Parekh, D. Dalle Nogare, R. S. Fischer, K. Temprine, M. Mione, A. B. Chitnis, C. A. Combs, and H. Shroff, "Resolution doubling in live, multicellular organisms via multifocal structured illumination microscopy," *Nat. Methods* **9**, 749–754 (2012).
- [17] D. Dan, M. Lei, B. Yao, W. Wang, M. Winterhalder, A. Zumbusch, Y. Qi, L. Xia, S. Yan, Y. Yang, P. Gao, T. Ye, and W. Zhao, "DMD-based LED-illumination Super-resolution and optical sectioning microscopy," *Sci. Rep.* **3**, 1116 (2013).
- [18] T. Instruments, "Using Lasers with DLP DMD technology," p. TI DN 2509927 (2008).
- [19] P. A. A. De Beule, A. H. B. de Vries, D. J. Arndt-Jovin, and T. M. Jovin, "Generation-3 programmable array microscope (pam) with digital micro-mirror device (dmd)," *Proc. of SPIE* **7932**, 79320G1–10 (2011).
- [20] X. Chen, B.-b. Yan, F.-j. Song, Y.-q. Wang, F. Xiao, and K. Alameh, "Diffraction of digital micromirror device gratings and its effect on properties of tunable fiber lasers," *Appl. Opt.* **51**, 7214–7220 (2012).
- [21] J. M. Zwier, G. J. Van Rooij, J. W. Hofstraat, and G. J. Brakenhoff, "Image calibration in fluorescence microscopy," *J. Microsc.* **216**, 15–24 (2004).
- [22] G. Boreman, *Modulation transfer function in optical and electro-optical systems* (SPIE Press, 2001).
- [23] J. Goodman, *Introduction to Fourier Optics* (The McGraw-Hill Companies, 1996).
- [24] S. Jiang and J. Walker, "Differential high-speed digital micromirror device based fluorescence speckle confocal microscopy." *Appl. Opt.* **49**, 497–504 (2010).
- [25] E. Mudry, K. Belkebir, J. Girard, J. Savatier, E. Le Moal, C. Nicoletti, M. Allain, and A. Sentenac, "Structured illumination microscopy using unknown speckle patterns," *Nature Photon.* **6**, 312–315 (2012).
- [26] J. Min, J. Jang, D. Keum, S.-W. Ryu, C. Choi, K.-H. Jeong, and J. C. Ye, "Fluorescent microscopy beyond diffraction limits using speckle illumination and joint support recovery," *Sci. Rep.* **3**, 2075 (2013).
- [27] C. Ventalon and J. Mertz, "Quasi-confocal fluorescence sectioning with dynamic speckle illumination," *Opt. Lett.* **30**, 3350–3352 (2005).

3

STUDYING DIFFERENT ILLUMINATION PATTERNS FOR RESOLUTION IMPROVEMENT IN FLUORESCENCE MICROSCOPY

Various types of non-uniform illumination can be used for resolution improvement in fluorescence microscopy. Here we study the differences between several types of incoherent illumination patterns, such as multi-spot, line and pseudo-random patterns. This requires an imaging setup and an image reconstruction algorithm that are flexible enough to incorporate any type of illumination pattern. We employ fluorescence microscope with structured illumination generated by a Digital Micromirror Device (DMD) and the pattern-illuminated Fourier Ptychography reconstruction algorithm (piFP) to this end. The piFP method is modified and improved by identifying the algorithm as steepest descent optimization of a least squares function. We find that illumination patterns with regular structure are superior to those with irregular structure in terms of resolution enhancement and noise level in the reconstructed images.

Parts of this chapter have been published as N. Chakrova, R. Heintzmann, B. Rieger, and S. Stallinga, *Opt. Express* **23**, 31367–31383 (2015) [1].

3.1. INTRODUCTION

STRUCTURED illumination microscopy (SIM) can be used to improve lateral resolution and optical sectioning capabilities of a fluorescence microscope. In standard wide-field fluorescence microscopy the sample is illuminated uniformly and the resolution is limited by diffraction to typically 180–250 nm laterally and 500–700 nm axially. In contrast to wide-field microscopy, in structured illumination microscopy multiple non-uniform illuminations are combined to improve sectioning and lateral resolution.

The mechanism responsible for the resolution improvement in structured illumination microscopy can be understood by considering the spatial frequency distributions of the illumination pattern and the sample. Multiplication of the sample structure with the illumination pattern in the object domain is equivalent to a convolution of the sample spectrum with the illumination pattern spectrum in the Fourier domain. As a result of this convolution, sample frequencies beyond the diffraction limit are shifted into the detection passband of the microscope objective. As the excitation and emission passbands are equal in an epi-illumination setup up to a small correction due to the Stokes shift, a maximum resolution improvement by a factor of two can be reached.

In conventional SIM periodic line patterns, which are created by the interference of two or three parallel beams in the sample plane, are used to double the resolution. The final image is reconstructed from several images acquired at different positions and orientations of the line pattern. SIM has been implemented in various configurations [2–5] and has also been extended to 3D imaging [6] and live cell imaging [7]. Although several other super-resolution methods lead to a larger resolution improvement [8–11], SIM plays an increasingly important role in biological imaging due to its compatibility with live cell imaging and with the wide range of existing standard fluorescent dyes [12].

Image reconstruction in SIM requires an accurate knowledge of the shift between line pattern illuminations [13, 14], and thus, is sensitive to misalignments and distortions of the illumination pattern. In order to lower the requirements on the precise knowledge of the illumination pattern in the reconstruction process, structured illumination methods with speckle illumination patterns have been developed. In the so-called blind-SIM approach unknown illumination patterns are reconstructed alongside the sample using a conjugate gradient algorithm [15, 16] or other algorithm [17]. The recent advancements in blind-SIM methods allow processing of 2D slices acquired in thick samples [18]. These methods can use speckle patterns created by projecting the light transmitted by a diffuser onto the sample. This arrangement significantly simplifies the optical setup and lowers the requirements on the knowledge of the projected patterns. Moreover, the algorithms can be helpful in reconstructing images in classical SIM in case the illumination patterns are distorted. Nevertheless, the high computational demands of these methods may hamper their use in practice. A different, less computationally demanding technique to improve the resolution based on the speckle illumination was recently demonstrated by Zheng et al. [19]. The sample structure and shifted illumination speckle pattern are reconstructed using the pattern-illuminated Fourier Ptychography (piFP) algorithm, which is a Fourier Ptychography concept [20], modified for use in fluorescence microscopy. It is worth noting that besides the attempts to improve the lateral resolution, speckle illumination has also been applied in order to achieve optical sectioning in fluorescence microscopy [21–23]. Based on these studies the question

arises whether SIM with regular illumination patterns (lines, spot arrays) or with irregular illumination patterns (speckle) is superior in terms of image quality.

In this paper we address this question using a flexible fluorescence microscope with structured illumination generated by a digital-micro-mirror device (DMD). The DMD-based fluorescence microscope belongs to the family of fluorescence microscopes with spatial light modulators integrated in their optical path [24–30]. We use the so-called single-pass configuration, where the DMD is placed only in the illumination path and the detection is standard widefield. The flexibility of the DMD allows us to study SIM with various types of illumination patterns, such as multi-spot, line, and pseudo-random patterns. An integral part of the imaging system is the reconstruction algorithm. We use the piFP technique, which can be used for any type of illumination pattern, thus matching the flexibility of our imaging setup. We start our treatment of image reconstruction for structured illumination microscopy by linking the piFP algorithm to steepest descent optimization of a quadratic function. Next, we investigate how the convergence speed of the piFP algorithm may be improved by modifying the iterative update step size. We then test the performance of different illumination patterns in terms of noise enhancement and resolution improvement. Finally, we demonstrate the differences in the behaviour of the various illumination patterns on bead samples and fixed biological samples.

3.2. THEORY

3.2.1. FOURIER PTYCHOGRAPHY METHOD AS STEEPEST DESCENT OF A QUADRATIC FUNCTION

In this section we will draw parallels between the iterative piFP scheme and least squares optimization via the steepest descent method. We consider an object represented by M pixels with intensities x_i ($i = 1, 2, \dots, M$) that is illuminated by a set of N illumination patterns p_i^n ($n = 1, 2, \dots, N$). Notice that here we model the continuous object as a discretized set of points, which is expected to give rise to correct results provided the sampling density is sufficiently high, i.e. above Nyquist. The expected photon count for pixel i and image n is given by the convolution sum:

$$\mu^n(\vec{r}_i) = \sum_{j=1}^M h^{em}(\vec{r}_i - \vec{r}_j) x(\vec{r}_j) p^n(\vec{r}_j), \quad (3.1)$$

where $h^{em}(\vec{r})$ is the normalized emission point spread function (PSF) of the microscope. In the following we will use the shorthands $h_{ij}^{em} = h^{em}(\vec{r}_i - \vec{r}_j)$, $\mu_i^n = \mu^n(\vec{r}_i)$, $x_i = x(\vec{r}_i)$, and $p_j^n = p^n(\vec{r}_j)$ for conciseness. The illumination patterns at the sample plane p_i^n are obtained from the DMD patterns q_i^n by convolution with the excitation PSF $h^{ex}(\vec{r})$:

$$p_i^n = \sum_{j=1}^M h_{ij}^{ex} q_j^n. \quad (3.2)$$

Here, effects of partial coherence in the illumination are neglected. The actually measured images d_i^n differ from the expected model images μ_i^n due to noise. The object

pixels x_i are reconstructed by minimizing the quadratic function:

$$E = \frac{1}{2} \sum_{n=1}^N \sum_{i=1}^M (d_i^n - \mu_i^n)^2, \quad (3.3)$$

which is sometimes derived from the log likelihood of the image formation model given the observations in the presence of uniform Gaussian noise. The minimum may be found numerically using a local iterative update algorithm:

$$x'_i = x_i + \beta_x \frac{\partial E}{\partial x_i}, \quad (3.4)$$

which is the gradient descent update rule with step size β_x . The gradient w.r.t. the object is given by:

$$\frac{\partial E}{\partial x_i} = - \sum_{n=1}^N \sum_{j=1}^M h_{ji}^{em} p_i^n (d_j^n - \mu_j^n) = - \sum_{n=1}^N \sum_{j=1}^M h_{ji}^{em} p_i^n \left(d_j^n - \sum_{k=1}^M h_{jk}^{em} x_k p_k^n \right) \quad (3.5)$$

The connection to the piFP algorithm becomes clear via the introduction of a set of additional variables – the N emission intensities for the N illumination patterns:

$$y_i^n = p_i^n x_i. \quad (3.6)$$

The update rule for the object 3.4 can then be split in three consecutive steps with these variables:

$$\text{step 1: } y_i^n = p_i^n x_i, \quad (3.7)$$

$$\text{step 2: } y'^n_i = y_i^n + \beta_y \sum_{j=1}^M h_{ji}^{em} \left(d_j^n - \sum_{k=1}^M h_{jk}^{em} y_k^n \right), \quad (3.8)$$

$$\text{step 3: } x'_i = x_i + \frac{\beta_x}{\beta_y} \sum_{n=1}^N p_i^n (y'^n_i - p_i^n x_i) \quad (3.9)$$

In case the step sizes are chosen to be $\beta_x = \beta_y = 1$, Eqs. 3.7-3.9 constitute the set of updates of the piFP algorithm [18]. It should be noted, however, that in the piFP method the object is updated for each update of the variable y_i^n , whereas in the optimization of the quadratic function E the object is updated once after all N variables y_i^n have been updated. We have observed that this sequential update of the object in the piFP algorithm results in artefacts in the reconstructed image during the first several iterations, but does not significantly influence the image quality at the convergence point. Moreover, we found that updating an object sequentially may be beneficial for the stability of the piFP algorithm when multi-spot and line illumination patterns are used. Interestingly, Guizar-Sicairos and Fienup have also made a connection to least squares fitting in their treatment of the original ptychographical iterative engine targeting phase retrieval in coherent imaging [31]. They argue that one would expect a more robust algorithm w.r.t noise if all the measurements are used simultaneously when refining the object estimate. We did not observe such an improvement in robustness, which might be explained by the different – incoherent – imaging modality that is considered here.

The key advantage of splitting the optimization of the squared error E in parts as above is that the update for y_i^n (step 2), proportional to the gradient, is purely expressed as a convolution. The update for the y_i^n in Fourier space is then purely local:

$$Y_i^n = Y_i^n + \beta_y \cdot OTF^* (D_i^n - Y_i^n \cdot OTF), \quad (3.10)$$

where capital letters indicate the Fourier transform counterparts of the variables, OTF is the optical transfer function, i.e. the Fourier transform of h^{em} , and the $*$ indicates the complex conjugate. The subsequent update for the x_i is local in direct space to start with.

If the illumination patterns p_i^n are unknown, they can be reconstructed as well in a similar manner:

$$p_i^n = p_i^n + \beta_p \frac{\partial E}{\partial p_i^n} = p_i^n + \frac{\beta_p}{\beta_y} x_i (y_i^n - p_i^n x_i). \quad (3.11)$$

Although the recovery of the illumination patterns is not strictly necessary when a DMD is used, it is worth considering for the sake of development of more simple fluorescence microscopes that use *a priori* unknown speckle illumination. In the following set of simulations and reconstructions we have assumed that the illumination patterns at the sample were given by the convolution of the known DMD patterns with the excitation PSF, as in 3.2. At the end of our treatment we will shortly revisit the matter of illumination pattern retrieval.

3.2.2. FOURIER PTYCHOGRAPHY ALGORITHM WITH NEWTON-RAPHSON UPDATE

The steepest descent method is often not the most effective way to solve an optimization problem. Methods involving the second order derivative of the objective function, such as the Levenberg-Marquardt (LM) or the Newton-Raphson (NR) algorithms, usually result in faster convergence by tuning the step sizes β_x and β_y . Application of the LM algorithm implies the calculation of the Hessian matrix of the optimized function E as obtained using Eqs. 3.2 and 3.5:

$$L_{ij} = \frac{\partial^2 E}{\partial x_i \partial x_j} = \sum_{n=1}^N \sum_{k=1}^M h_{ki}^{em} h_{kj}^{em} p_i^n p_j^n = \left(\sum_{k=1}^M h_{ki}^{em} h_{kj}^{em} \right) \left(\sum_{l=1}^M \sum_{m=1}^M h_{il}^{ex} h_{jm}^{ex} \left(\sum_{n=1}^N q_l^n q_m^n \right) \right), \quad (3.12)$$

and multiplication of the gradient of the merit function with the inverse of $L + \kappa \text{diag}(L)$, with κ the LM-parameter, rather than with the constant step size β_x . Further simplification is possible if the DMD patterns q_i^n are designed such that their sums are:

$$\sum_{n=1}^N q_i^n = N \langle q \rangle, \quad (3.13)$$

$$\sum_{n=1}^N (q_i^n)^2 = N \langle q^2 \rangle, \quad (3.14)$$

independent of pixel location i . These conditions can be fulfilled by programming patterns of the DMD in such a way that each DMD pixel is switched “on” the same number of times and, hence, the overall illumination is uniform. In fact, these patterns are preferred over fully randomized patterns, since a uniform total illumination results in a reduced overall noise level. If furthermore we may neglect correlations between the on-off sequences at different DMD pixels then it holds that:

$$\sum_{n=1}^N q_i^n q_m^n \approx N \left(\langle q^2 \rangle - \langle q \rangle^2 \right) \delta_{lm} + N \langle q \rangle^2. \quad (3.15)$$

We are, however, aware that this assumption is only partly correct for our experimental setup. Assuming that the excitation PSF is normalized to unity we then find a Hessian:

$$L_{ij} = N \left(\langle q^2 \rangle - \langle q \rangle^2 \right) \sum_{k=1}^M h_{ki}^{em} h_{kj}^{em} \sum_{l=1}^M h_{il}^{ex} h_{jl}^{ex} + N \langle q \rangle^2 \sum_{k=1}^M h_{ki}^{em} h_{kj}^{em}. \quad (3.16)$$

Application of the LM-algorithm requires the inversion of the matrix $L + \kappa \text{diag}(L)$, a daunting task as this is an $M \times M$ matrix with M the total number of pixels. This could be done more efficiently by splitting the image in patches but nevertheless requires a substantial numerical effort in matrix inversion. The NR-algorithm, on the other hand, uses only the diagonal part of the Hessian, making the update local again:

$$x_i' = x_i - \frac{1}{L_{ii}} \frac{\partial E}{\partial x_i} \quad (3.17)$$

with:

$$L_{ii} = N \left(\langle q^2 \rangle - \langle q \rangle^2 \right) \sum_{k=1}^M (h_{ki}^{em})^2 \sum_{l=1}^M (h_{li}^{ex})^2 + N \langle q \rangle^2 \sum_{k=1}^M (h_{ki}^{em})^2. \quad (3.18)$$

Shift invariance of the illumination and imaging now imply that the sums:

$$K_i^{em} = \sum_{k=1}^M (h_{ki}^{em})^2 = K^{em}, \quad (3.19)$$

$$K_i^{ex} = \sum_{l=1}^M (h_{li}^{ex})^2 = K^{ex} \quad (3.20)$$

are also independent of pixel location. Then the diagonal part of the Hessian is simply proportional to the identity matrix:

$$L_{ii} = N \left(\langle q^2 \rangle - \langle q \rangle^2 \right) K^{em} K^{ex} + N \langle q \rangle^2 K^{em}, \quad (3.21)$$

for all pixels i . The crucial approximation in deriving this result is the neglect of the correlations between the on-off sequences of the different DMD pixels. We will apply the NR-algorithm under this approximation in the following.

3.3. SIMULATIONS

3.3.1. SIMULATION SETUP

THE original piFP algorithm was compared to the piFP algorithm with Newton-Raphson (NR) update step size in simulations. The performance of both image reconstruction algorithms was evaluated for various types of illumination patterns. A simulated resolution target, shown in Fig. 3.1(a), was used as test object. The imaging system was described by the scalar diffraction based Airy PSF with full width at half maximum $FWHM \approx 0.513\lambda_{em}/NA$, where $\lambda_{em} = 530$ nm is the emission wavelength and $NA = 1.4$ is the numerical aperture of the objective. A pixel of the simulated resolution target in the sample plane equals $\lambda_{em}/16NA$ and the numbers of line groups in Fig. 3.1(a) indicate the pitch of the group in units of $\lambda_{em}/8NA$. Hence, group 4 is at the limit of the widefield imaging and group 2 is at the limit of the structured illumination imaging.

We have tested three types of DMD patterns: multi-spot, pseudo-random and line patterns, as shown in Figs. 3.1(b-d). A multi-spot DMD pattern is generated as a square

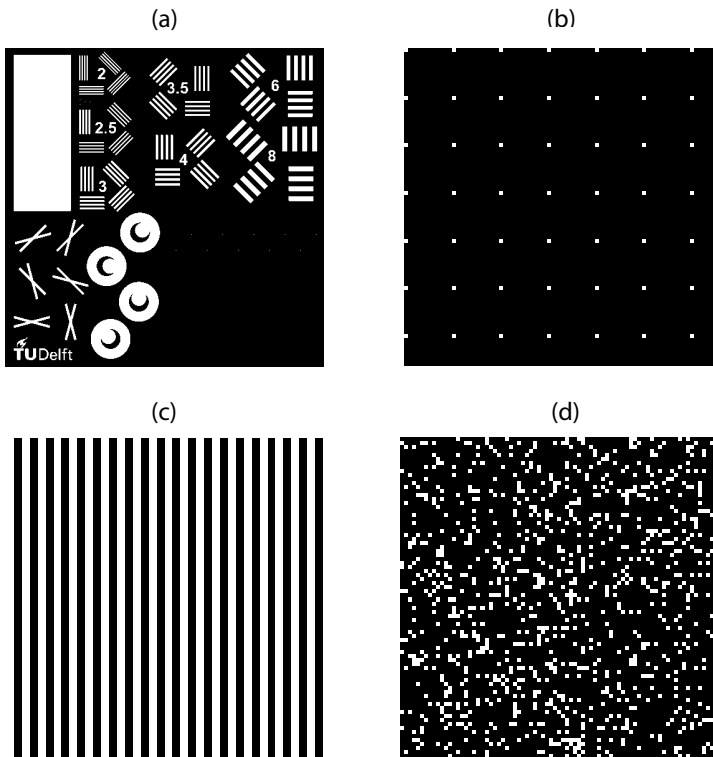


Figure 3.1: (a) Simulated resolution target. Line group 4 has the pitch of $\lambda_{em}/2NA$, corresponding to the limit of the widefield imaging. (b)-(d) Examples of illumination patterns generated at the DMD: multi-spot (b), line (c) and pseudo-random (d) patterns.

grid of spots with the size of one pixel. The pattern is then translated $N - 1$ times by one pixel in order to illuminate the whole object. Pseudo-random DMD patterns are gener-

ated in the following way. Suppose we have a set of N pseudo-random DMD patterns. Each pixel is switched “on” S times making the sum of the N patterns uniform. The S patterns for which any pixel is nonzero are randomly drawn from the total set of N patterns. In this way we can generate pseudo-random patterns with controlled sparsity and uniform total illumination. Finally, several shifts and rotations of a binary line grid are used to generate a set of line patterns. The maximum frequency of the projected patterns is limited to $f_{cutoff} = 2NA/\lambda_{ex}$ in an epi-fluorescence microscope setup. Hence, assuming totally incoherent DMD illumination, the generated illumination patterns are multiplied in the Fourier domain by the incoherent OTF of the optical system with a cutoff frequency f_{cutoff} in order to obtain the set of illumination patterns p_i^n in the sample plane. The N illumination patterns p_i^n are made to be uniform in their sum and the total intensity of N images d_i^n is taken equal for all the described pattern types. The illumination intensity per pixel summed over all patterns is set to 2.5×10^4 photons and Poisson noise is added to each simulated image. Although the quadratic error metric of Eq. 3.3 does not apply to Poisson noise, it nevertheless can be expected to minimize the misfit between the noisy observations and expected images based on the image formation model. The described image reconstruction algorithms were implemented in MATLAB (Mathworks, USA) using the DIPimage toolbox [32]. The reconstructions were carried out according to Eqs. 3.7–3.9, where an object with uniform intensity was used as an initial guess for the object variables x_i considered here.

3.3.2. STOPPING CRITERION

We have shown that the piFP-algorithm is equivalent to least squares optimization, which is known to be an ill-posed mathematical problem in the absence of regularization. We have indeed observed that letting the iteration run to reach the best possible numerical convergence tends to lead to undesirable graininess in the reconstruction, i.e. to noise amplification. This effect becomes apparent when examining the development of the modulation transfer function (MTF) with iterations (Fig. 3.2). In order to obtain the MTF curves we have simulated piFP imaging of a line object with a thickness of one pixel. The MTF was calculated as the Fourier transform of the line profile in the reconstructed image at each iteration of the piFP algorithm. As seen in Fig. 3.2, with the growing number of iterations the high frequency components are increasingly amplified, which simultaneously leads to the noise amplification. In addition, with the growing number of iterations the shape of the MTF curve becomes increasingly less smooth, causing ringing artefacts in the reconstructed image.

Clearly, some form of regularization is needed in order to prevent this problematic noise blowup and avoid ringing artefacts. We have found that abandoning numerical precision as criterion for terminating the iteration in favour of a more loose criterion on the error metric E defined in Eq. 3.3 can effectively serve as regularization for the optimization problem. It appears that E converges to a value following from the noise statistics only. In case there is only shot noise, this limiting value, which we term noise level NL , is:

$$NL = \sum_{n=1}^N \sum_{i=1}^M d_i^n, \quad (3.22)$$

We obtained satisfactory reconstructions when the iterative optimization was stopped if the error E is equal to NL or within a small fraction of it, say within 1%. This convergence criterion is reached within 3-60 iterations (we consider N updates of the object for N illumination patterns to be one iteration of the piFP algorithm), depending on the type of projected patterns and the choice of β .

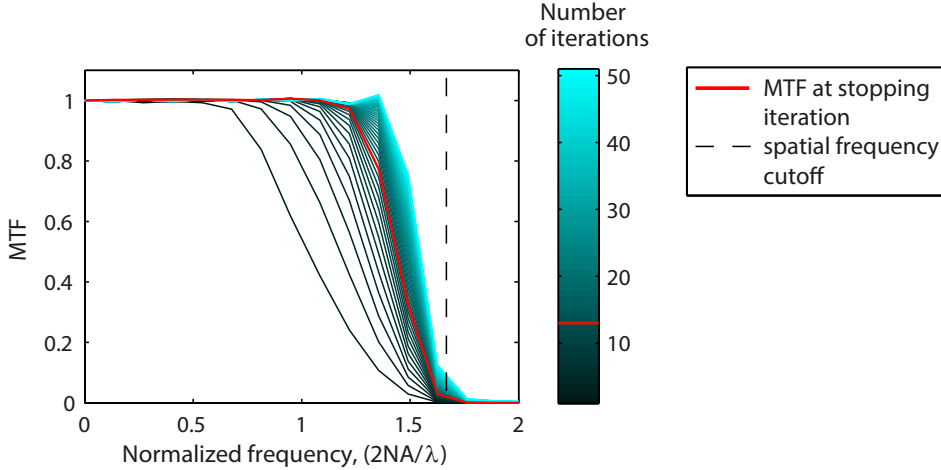


Figure 3.2: Change of the MTF curves during the piFP iterations. Multi-spot illumination patterns with a pitch of 12 pixels, which corresponds to a spatial frequency cutoff of 1.7 times the widefield bandwidth $2NA/\lambda$, were used to simulate the illumination of a line object. The MTF is calculated as the Fourier transform of the line profile at each iteration of the piFP reconstruction algorithm. The stopping iteration is highlighted in red. The vertical dashed line indicates the highest possible resolution improvement estimated from the pitch of the projected illumination patterns.

3.3.3. THE EFFECT OF SPARSITY AND NUMBER OF PSEUDO-RANDOM PATTERNS

Figure 3.3 shows a comparison of the image quality for pseudo-random patterns with different sparsity. The fill factor f – the percentage of non-zero DMD pixels per pattern – is the measure of sparsity of the projected patterns. Here we used a total number of illuminations $N = 144$ and the original piFP reconstruction algorithm [18]. The illumination dose is rescaled in order to keep the total illumination intensity of N images constant regardless of the sparsity. Figure 3.3(a) shows the relative difference between the error, calculated according to Eq. 3.3 and the noise level, calculated according to Eq. 3.22. The crossings of the curves with the horizontal dashed line indicate when the error reaches the noise level within 1%, the stopping condition for the iterative algorithm. A comparison of the signal-to-noise ratios (SNR) is given in Fig. 3.3(b). The SNR was measured as the mean signal of the uniform rectangle in the top-left corner of the resolution target divided by the standard deviation of the signal across that uniform area (background is zero). The horizontal dashed line shows the SNR in a uniformly illuminated widefield image with the same illumination dose as the cumulative dose of the N pseudo-random patterns. Figure 3.3(c) shows the resolution improvement as a function of the number of

iterations. The full width at half maximum (FWHM) was estimated by fitting a Gaussian function to point objects in the reconstructed images of the resolution target (not visible in Fig. 3.1(a)). The horizontal dashed line shows the FWHM of a widefield image.

The simulation results indicate that patterns with high fill factor, which imitate speckle illumination, are inferior to patterns with lower fill factor in terms of resolution improvement and noise suppression. However, the improvement in FWHM and SNR for lower fill factor comes at the expense of a reduced convergence speed. For the given number of illumination patterns $N = 144$, one iteration takes 2.2 seconds on an Intel Xeon E5-1620 v2 CPU with 3.70 GHz clock speed. Hence, the total reconstruction time increases from 6.6 seconds in case $f = 20\%$ to 2.2 minutes in case $f = 0.7\%$. Moreover, in order to obtain even lower sparsity, one has to increase the total number of illumination patterns, which will lead to further deceleration of the reconstruction process. In this sense, confocal imaging can be seen as a particular case of structured illumination, in which the lowest possible sparsity is achieved.

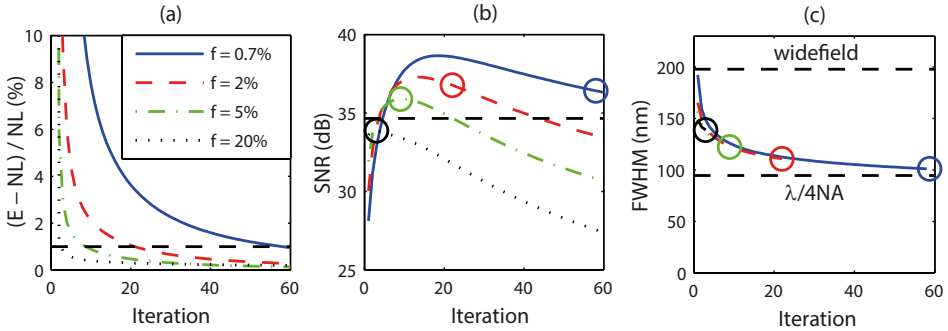


Figure 3.3: Comparison of the image SNR quality for pseudo-random patterns with different sparsity. (a) Illustration of the stopping condition. The crossings of the curves with the horizontal dashed line indicate when the error reaches the noise level within 1%. (b) Lower fill factor results in higher SNR. Horizontal dashed line shows the SNR in a widefield image. Round markers indicate the final iteration according to our stopping criterion. (c) Lower fill factor results in smaller FWHM. The dashed lines show the FWHM in a widefield image and the best possible resolution $\lambda/4NA$.

Another parameter influencing the quality of the reconstructed image in the case of pseudo-random illumination is the total number of illumination patterns N . Figure 3.4 shows that the resolution improves with increasing number of illumination patterns, probably because cross-talk effects from neighboring pixels are averaged out over multiple acquisitions. This differs from the situation with spatially periodic illumination, where the number of projected patterns plays a secondary role. When line or multi-spot illumination patterns are used, the resolution of the reconstructed image mainly depends on the spatial frequency content (pitch) of the projected illumination patterns.

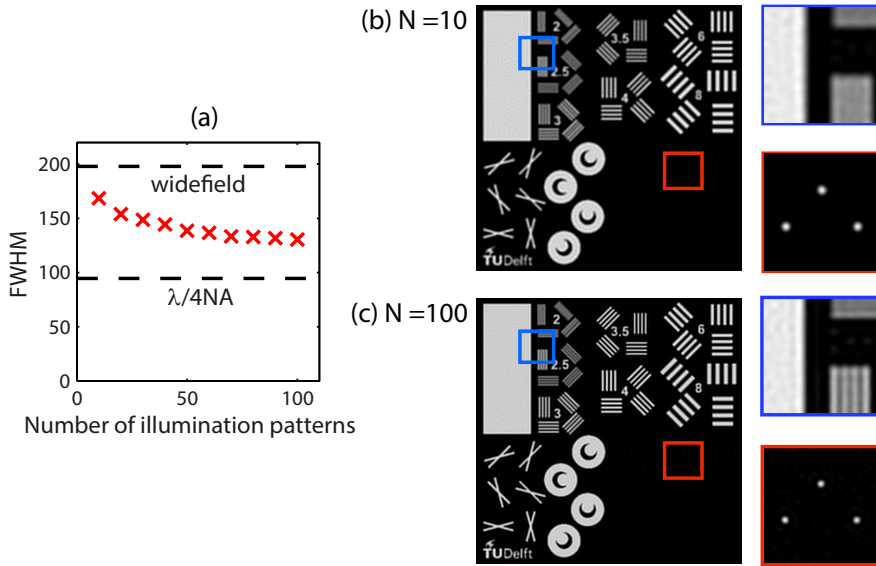


Figure 3.4: (a) In the case of pseudo-random illumination, the resolution of the reconstructed image improves with increasing number of illumination patterns N . We used 10 illumination patterns in (b) and 100 illumination patterns in (c). The sparsity of the patterns is kept constant ($f = 10\%$).

3.3.4. COMPARISON OF ILLUMINATION PATTERN TYPES

Theoretically, projecting a line or a multi-spot pattern with a spatial frequency as large as $2NA/\lambda_{ex}$ will result in the largest resolution improvement. However, due to the low modulation at the limit of the OTF in an incoherent illumination system and the presence of noise, a 10-30% smaller spatial frequency of the projected pattern is used in real imaging systems. We used a pitch of 12 pixels ($12 \text{ pixels} = 1.5 \times \lambda_{ex}/2NA$) for the multi-spot and line patterns and a sparsity of 0.7%, which results in an average distance of 12 pixels, for the pseudo-random patterns. These values for the pitch and the average distance correspond to a spatial frequency of the projected patterns that is 33% smaller than the cutoff frequency of the microscope. The total number of illuminations is kept at $N = 144$ for each pattern type, while keeping the total illumination dose constant. Since within a single piFP iteration the object is updated N times, the same number of illuminations for each pattern type is required in order to provide a fair comparison of the convergence speeds of the algorithm for different types of illumination patterns. The required number of line pattern illuminations was obtained by using 12 shifts and 12 rotations of the line grid. This is different from standard SIM acquisitions in which 3 to 5 shifts and 3 or 5 rotations are used.

The comparison of the performance of the two described algorithms and three types of illumination patterns is given in Fig. 3.5. The convergence speed is significantly higher when multi-spot and line patterns are used instead of pseudo-random illumination patterns. Furthermore, as predicted by theory, the convergence speed of the piFP algorithm with NR update rule is improved in comparison to the original piFP algorithm for all

types of illumination patterns. The effect is most evident in the case of pseudo-random patterns, where the number of iterations is reduced by a factor of two; for the multi-spot and line patterns the improvement is inessential. Furthermore, we observe that application of the NR update rule leads to a moderately reduced SNR and slightly improved FWHM at the stopping point of the iteration. In the case of pseudo-random illumination patterns the decrease in SNR and FWHM when NR update rule is used is negligible. In the case of multi-spot and line illumination patterns the SNR decrease is within 15% and the FWHM improvement is within 10%. This result reflects the trade-off between resolution improvement and noise amplification – sharper images typically exhibit more pronounced noise structures in the uniform areas.

The SNR and FWHM values of a conventional SIM image, reconstructed from 9 line grid illuminations using the generalized Wiener filter reconstruction [33], are given for comparison. It should be noted, that the illumination patterns do not reach maximum modulation, since they are projected from the DMD onto the sample fully incoherently via the objective lens, and are hence blurred by the illumination PSF. The modulation depth of the projected pattern is an important parameter, influencing the quality of the SIM image. A conventional SIM image reconstructed from acquisitions with larger modulation of the illumination pattern at the sample would have resulted in a smaller FWHM. Achieving improved modulation in DMD-generated illumination patterns is in principle possible by treating the DMD as a diffraction grating and filtering out the DC component in the Fourier plane. Another option would be to exploit the flexibility of the DMD to study the formation of three-dimensional illumination patterns.

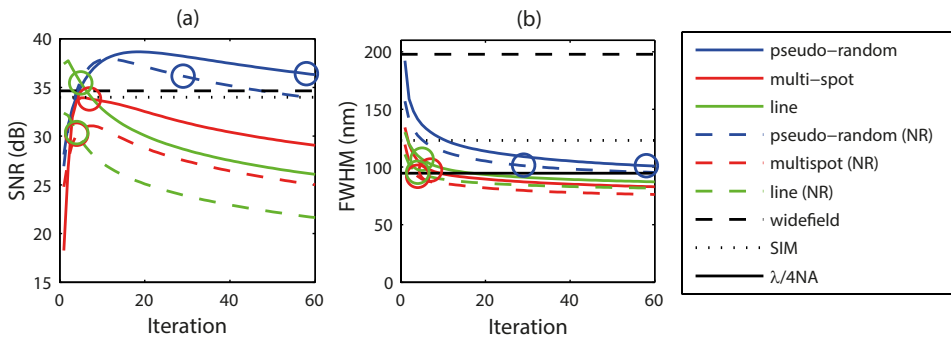


Figure 3.5: Performance of the original piFP algorithm compared to the performance of the piFP algorithm with NR update rule for different types of illumination patterns. SNR (a) and FWHM (b) curves display the trade-off between the sharpness of the structures and the noise appearance in the reconstructed images. Application of the NR update rule leads to faster convergence, reduced SNR and improved FWHM. Round markers indicate the final iteration according to our stopping criterion. The SNR and FWHM values of the widefield and conventional SIM images are given for comparison.

Finally, reconstruction with the piFP algorithm and the proposed stopping criterion is independent of the underlying sample structure and applied illumination type. In contrast to the generalized Wiener filter reconstruction, where the regularization parameter has to be set empirically, the proposed method does not require adjustment of

parameters with unclear impact on the final image quality. The novel stopping criterion we propose automatically provides for the needed regularization.

3.4. EXPERIMENT

3.4.1. EXPERIMENTAL SETUP

WE conducted a series of experiments in order to test the performance of the modified piFP algorithm with the different illumination pattern types. Our DMD-based microscope is built by complementing an inverted Olympus IX71 fluorescence microscope with an illumination branch that provides the projection of the DMD patterns onto the sample. An expanded and despeckled beam of a 488 nm laser is used to illuminate the DMD. The DMD pixels with physical size of $13.68 \mu\text{m}$ are then demagnified to 137 nm in the sample plane with the help of a 250:150 mm lens relay and a $60\times/0.7$ air objective (Fig. 3.6). Although higher resolution images can be produced with immersion objectives, this is not needed for the current comparison study. The actually measured NA of the excitation beam in the back focal plane of the objective lens amounts to 0.6, thus, illumination and detection NA slightly differ. The pixel sampling of the Orca Flash 4.0 camera corresponded to 108 nm at the sample, which provides slight undersampling ($\sim 10\%$) of the specimen compared to the maximum cutoff $2NA_{im}/\lambda_{em} + 2NA_{ill}/\lambda_{ex}$. A precise mapping of the DMD to the camera is required for accurate prediction of the illumination patterns from the patterns displayed on the DMD. We have used an earlier developed calibration procedure in order to establish the correspondence between each DMD pixel and its image on the camera. The details on the optical design of the setup and the calibration procedure are given in [34].

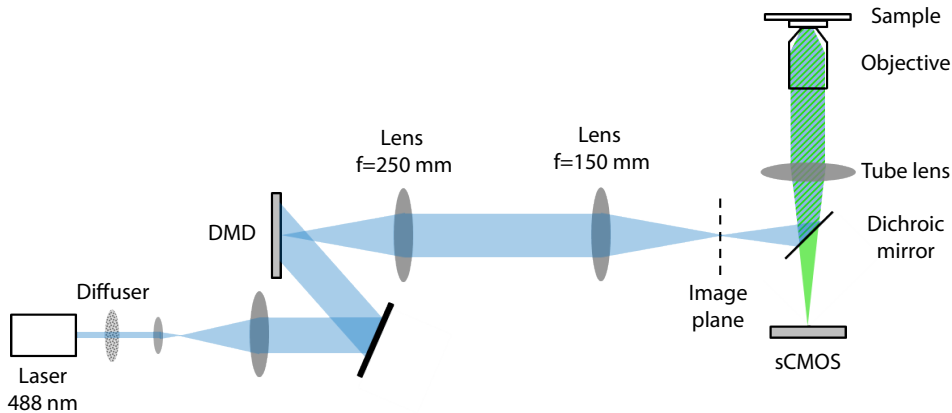


Figure 3.6: Schematic view of the DMD-based fluorescence microscope. The beam of the 488 nm diode laser is despeckled and expanded in order to provide illumination of the DMD surface. The DMD patterns, demagnified by the 250:150 mm optical relay and by the objective lens, are projected onto the sample. The sCMOS camera detects fluorescence from the sample. One camera frame is taken for each illumination pattern [34].

3.4.2. IMAGING FLUORESCENT BEADS

Multi-spot and pseudo-random illumination patterns were applied to a sample containing 100 nm diameter fluorescent microspheres (Invitrogen, CA, USA) deposited on a microscope coverslip. We have used a pitch of 10 DMD pixels for the multi-spot illumination patterns and a fill-factor of 1% and 10% for the pseudo-random illumination patterns. The total number of illuminations is $N = 100$ and the overall illumination dose is kept the same for all illumination types by adjusting the power of the laser.

The original piFP algorithm assumes reconstruction of 2D slices and does not take the background and the out-of-focus light into account. The background intensity is, however, always present in the acquired images. We found that the reconstruction can be improved by adding a background to the estimates of the emission intensities in step 1 of the algorithm. This background was estimated as the 20th percentile of the intensity in the set of N collected images. The expected noise level NL was estimated from the read-out noise of the camera and the Poisson statistics of light. The stopping criterion proposed in section 3.2 was reached within 8 iterations in case of the multi-spot illumination patterns. However, in case of the pseudo-random patterns the predicted noise level does not correspond to the convergence value of the error metric E . We assume that an additional noise source is present in the images acquired under pseudo-random illumination that hinders the correct noise level estimation in this case. Low fill factors lead to high additional noise, while high fill factors provide some averaging of the background intensity and lead to lower noise. Therefore, an alternative stopping criterion was used for pseudo-random illumination patterns: the convergence is reached when the change of E between two consecutive iterations is within a small fraction (we have taken 2%) of E . This criterion is reached for $f = 1\%$ and $f = 10\%$ within 17 and 4 iterations respectively.

The comparison of the images, acquired for the various illumination pattern types and reconstructed by the original piFP algorithm, is given in Fig. 3.7. The zoom-in area shows neighboring beads, which are not resolved in a widefield image (Fig. 3.7(a)), but are clearly resolved in the reconstructed image after multi-spot illumination (Fig. 3.7(c)). The resolution is also better than obtained from a standard Richardson-Lucy deconvolution of the widefield image (Fig. 3.7(b)). We observe that the relative intensities of the fluorescent beads are not preserved in the image reconstructed after the pseudo-random illumination patterns with low fill factor (Fig. 3.7(d)). This qualitative observation indicates that the pseudo-random illumination patterns with low fill factor, which would theoretically lead to higher resolution improvement than the patterns with high fill factor, cannot be reliably applied in practice. The piFP reconstruction after pseudo-random illumination patterns with higher fill factor displays correct relative intensities of the beads (Fig. 3.7(e)); however, as predicted by the theory, it shows weaker resolution improvement compared to the piFP reconstruction after the multispot illumination patterns.

We have observed that in case of multi-spot patterns and pseudo-random patterns with high fill factor, the piFP algorithm with NR update rule is only marginally faster than the original piFP algorithm; at the same time, it is less stable and occasionally leads to diverging solutions when applied to experimental data. Hence, for most practical cases in fluorescence microscopy the original piFP algorithm converges sufficiently fast and is

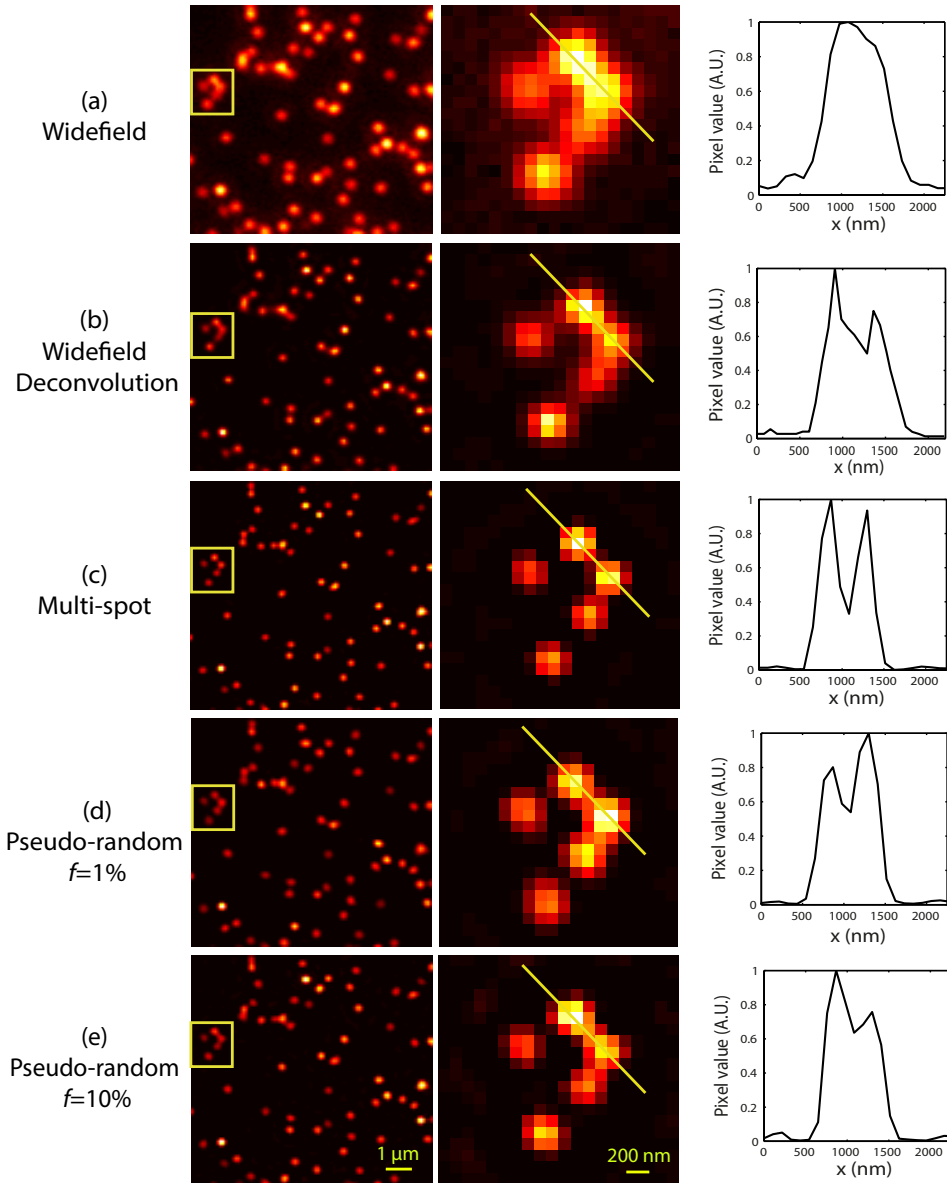


Figure 3.7: Comparison of piFP reconstructions for different illumination patterns. The sample containing 100 nm diameter fluorescent microspheres was imaged using a $60\times/0.7$ air objective. (a) Widefield image. The two neighboring beads shown in the zoom-in area are not resolved. (b) Widefield image deconvolved using the Richardson-Lucy algorithm shows slight resolution improvement. (c) piFP reconstruction for the multi-spot illumination patterns. The two neighboring beads are well resolved. (d) piFP reconstruction for the pseudo-random illumination patterns with fill factor $f = 1\%$. The neighboring beads are separated, however, the relative intensities of the beads are not preserved. (e) piFP reconstruction for the pseudo-random illumination patterns with fill factor $f = 10\%$ shows weaker resolution improvement compared to the multi-spot patterns.

preferred because of its stability. The NR update rule in piFP algorithm can be recommended when a large number of sparse pseudo-random illumination patterns is used.

3.4.3. IMAGING FILAMENTOUS SAMPLES

The same multi-spot and pseudo-random patterns as described in section 3.4.2 were tested on a test slide with bovine pulmonary artery endothelial (BPAE) cells (Invitrogen, CA, USA), in which F-actin is stained with Alexa Fluor 488 phalloidin. Estimation of the noise level is a demanding task for this sample, since its three-dimensional structure leads to high background and out-of-focus light. Therefore, we have used the stopping criterion based on the change of E between two consecutive iterations as described in section 3.4.2. In agreement with the results achieved on the bead sample, multi-spot illumination patterns produce the most visually satisfactory reconstruction (Fig. 3.8(d)), while pseudo-random patterns with 1% fill factor result in enhanced graininess in the reconstructed image (Fig. 3.8(e)). As can be seen in Fig. 3.7(d), this graininess leads to inaccurate representation of the relative intensities in the image. Finally, an image reconstructed for pseudo-random illumination patterns with 10% fill factor displays pronounced low frequency noise structures that are typical for SIM images reconstructed with insufficient apodization [35] (Fig. 3.8(f)).

3.4.4. RECONSTRUCTION OF ILLUMINATION PATTERNS

An obvious advantage of using a DMD compared to speckle illumination is having a priori knowledge about the projected illumination patterns, which significantly simplifies the reconstruction process in terms of speed and robustness. In the above we did not include the reconstruction of the illumination patterns p^n in the algorithm, since we use pre-designed patterns generated by the DMD and assume that these illumination patterns are mapped to the camera pixel grid with high accuracy. We have added the illumination pattern reconstruction step according to Eq. 3.11 in order to test the influence of this additional step in the algorithm on the final reconstruction. We have used N different illumination patterns, in contrast to the original piFP algorithm [18], where N shifts of a single DMD pattern are used. Hence, in our method each of the N illumination patterns has to be reconstructed separately. The initial estimate of each illumination pattern p^n is given by the expected illumination pattern, i.e. by the known DMD pattern blurred by the excitation PSF of the objective. As shown in Figs. 3.9(a) and 3.9(b), the algorithms with and without the p^n refinement step produce comparable sample reconstructions; however, the algorithm with the p^n refinement step takes several iterations longer to reach convergence. Reconstructed illumination patterns match the expected illumination patterns well, thereby confirming the high accuracy of the used calibration procedure.

We have also implemented an illumination pattern reconstruction taking the uniform sum illumination constraint of Eq. 3.13 into account using a Lagrange multiplier approach. This procedure gave rise to a similar outcome. It is necessary in the pattern estimation to use the prior knowledge of the DMD-patterns as starting point for the iteration in order to guarantee convergence. Taking uniform illumination patterns as starting point did not result in reasonable reconstructions. We may conclude that the piFP algorithm can work as a “semiblind SIM” deconvolution, in contrast to the fully “blind

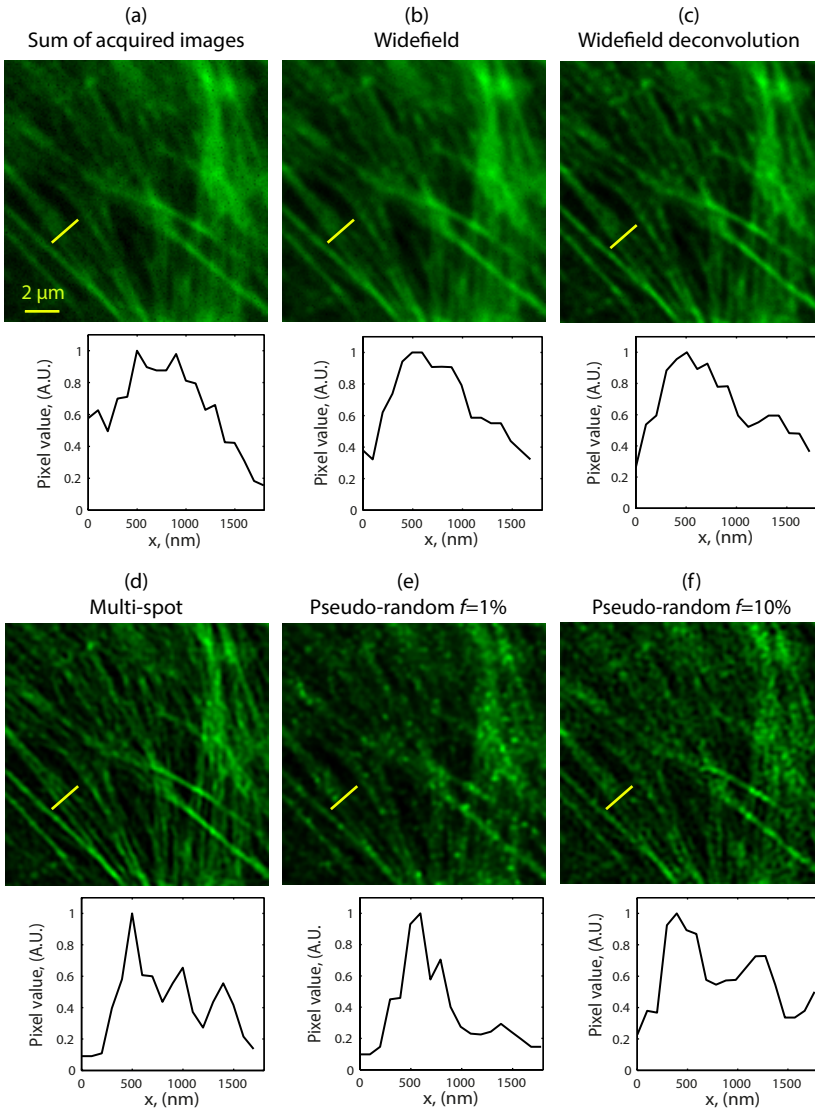


Figure 3.8: Comparison of piFP reconstructions for different illumination patterns. Images of the BPAE cells were acquired using a $60\times/0.7$ air objective. (a) The sum of all acquired frames is given to demonstrate the uniformity of the illumination. (b) Widefield image. (c) Deconvolution of the widefield image using Richardson-Lucy algorithm. (d) piFP reconstruction for the multi-spot illumination patterns. (e) piFP reconstruction for the pseudorandom illumination patterns with fill factor $f = 1\%$ showing enhanced graininess. (f) piFP reconstruction for the pseudo-random illumination patterns with fill factor $f = 10\%$ showing pronounced low frequent noise structures. The profile plots along the highlighted yellow line only show three distinct filaments for the multi-spot reconstruction in (d).

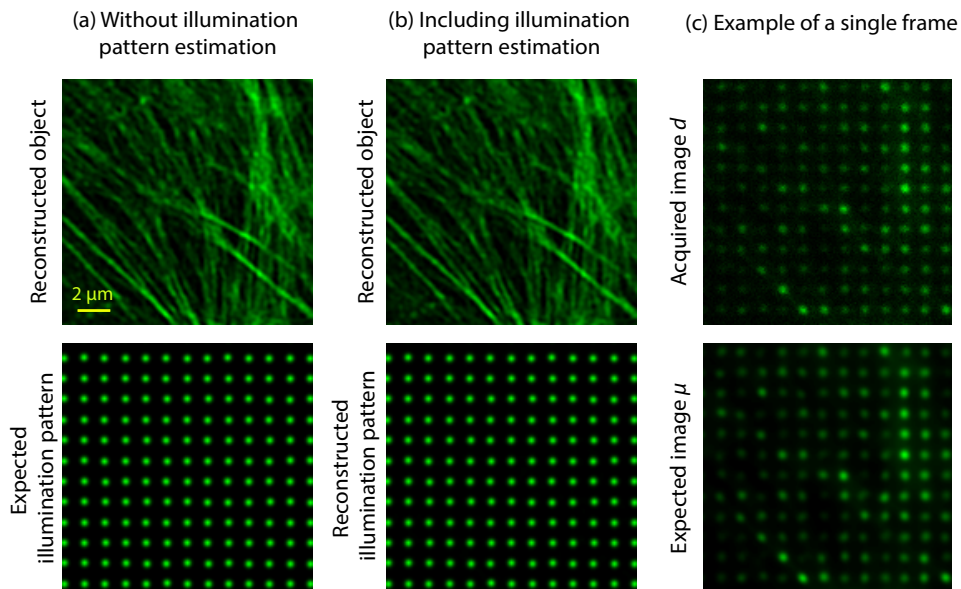


Figure 3.9: The algorithms with and without the reconstruction of the illumination patterns produce comparable results. (a) piFP reconstruction using known illumination patterns reaches convergence in 7 iterations. Images show the reconstructed object and an example of the known illumination pattern. (b) piFP reconstruction with estimation of the illumination patterns reaches convergence within 9 iterations. Images show the reconstructed object and an example of the estimated illumination pattern. (c) An example of the actually measured image d^n and the corresponding expected image μ^n in case the known illumination patterns are used.

SIM” deconvolution approach [13,14]. A comparison of the actually measured image d^n and the corresponding expected image μ^n is given for illustration in Fig. 3.9(c).

In order to further test the strength of the prior knowledge of the illumination patterns we have also compared the expected and reconstructed pseudo-random illumination patterns with higher fill-factor ($f = 10\%$). Figure 3.10 gives the representation of the difference between the reconstructed and expected illumination patterns and reveals good correspondence between the two with errors typically below 10%.

3.5. CONCLUSION

IN this paper we have shown that the piFP algorithm, which is the FP concept applied to fluorescence microscopy, can be interpreted as a steepest descent optimization of a quadratic function. This representation opens opportunities to modify, improve or specifically tailor the piFP algorithm to the details of the given optimization problem. We have demonstrated in simulations the improvement of the convergence speed of the piFP algorithm by modifying its update coefficients according to the Newton-Raphson rule.

We have used a DMD-based fluorescence microscope with widefield detection and

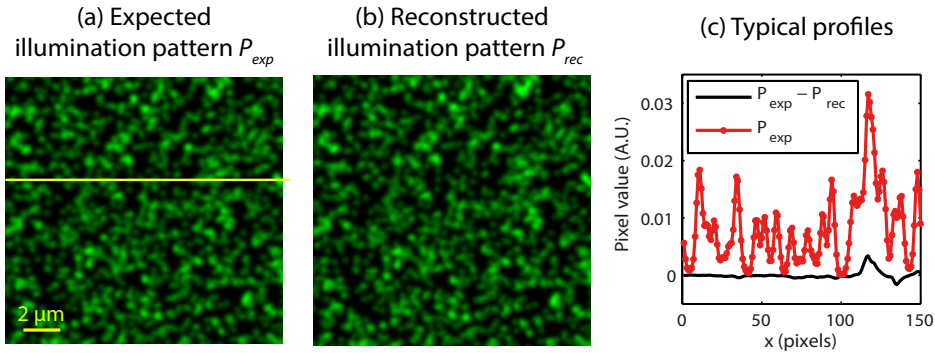


Figure 3.10: Comparison of the expected (a) and reconstructed (b) patterns in case of pseudo-random illumination with fill-factor $f = 10\%$. (c) The profile of the difference $P_{exp} - P_{rec}$ along the yellow line shown in (a) reveals good correspondence between the expected and reconstructed illumination patterns.

image reconstruction with the piFP algorithm to test various illumination patterns for resolution improvement and noise enhancement in fluorescence microscopy. We also show that accurate calibration of the microscope enables one to omit the step of reconstructing the illumination patterns in the algorithm. We demonstrate, both in simulations and in experiments, that the illumination patterns with a regular spatial structure, such as multi-spot or line patterns, are preferred over randomized patterns even when the illumination patterns are known. Regular illumination patterns do not have a sharply peaked spatial frequency content but instead a more smeared out spectrum. The reconstructed MTF in the region beyond the widefield cutoff can therefore be anticipated to be lower than for regular illumination patterns. In order to achieve the same sharpness this will come at the expense of significant noise enhancement.

According to our simulations, pseudo-random patterns with high sparsity provide better resolution improvement and noise suppression than pseudo-random patterns with low sparsity. However, in practice, there appears to be an additional noise source present in the images reconstructed from pseudo-random illuminations. This noise source plays a larger role in case the sparsity of the pseudo-random illumination patterns is high, resulting in grainy images. Tracking the root cause of this effect is the target of follow-up research. We speculate here that it may lie in imperfections of the imaging model. First of all, our two-dimensional imaging model does not take the three-dimensional structure of real samples and of the microscope PSF into account. Second, the scalar diffraction based Airy PSF model is a simplification at the moderately high $NA = 0.7$ at which the images were acquired. Finally, slight non-uniformities and correlations in the illumination patterns due to insufficiently suppressed spatial coherence in the illumination may also play a role. Extending the piFP method to incorporate these effects is an important next step in developing the piFP imaging technique. Regularization techniques may also be added into the mix to establish a form of noise suppression. Finally, an in-depth comparison of the piFP method with other reconstruction methods, notably the joint Richardson-Lucy deconvolution method [36, 37], would further serve to benchmark the algorithm.

3.6. ACKNOWLEDGMENTS

We would like to thank Guoan Zheng for kindly providing the original software for the piFP algorithm for comparison purposes, and Erik Manders and Ronald Breedijk for fruitful discussions. This research is supported by the Dutch Technology Foundation STW (<http://www.stw.nl/>), which is part of the Netherlands Organization for Scientific Research (NWO), which is partly funded by the Ministry of Economic Affairs, Agriculture and Innovation.

3

REFERENCES

- [1] N. Chakrova, R. Heintzmann, B. Rieger, and S. Stallinga, “Studying different illumination patterns for resolution improvement in fluorescence microscopy,” *Opt. Express* **23**, 31367–31383 (2015).
- [2] M. G. L. Gustafsson, “Surpassing the lateral resolution limit by a factor of two using structured illumination microscopy,” *J. Microsc.* **198**, 82–87 (2000).
- [3] R. Heintzmann and C. Cremer, “Laterally modulated excitation microscopy: improvement of resolution by using a diffraction grating,” *Proc. SPIE* **3568**, 185–196 (1999).
- [4] J. T. Frohn, H. F. Knapp, and A. Stemmer, “True optical resolution beyond the Rayleigh limit achieved by standing wave illumination,” *Proc. Natl. Acad. Sci. USA* **93**, 7232–7236 (2000).
- [5] G. E. Cragg and P. T. So, “Lateral resolution enhancement with standing evanescent waves,” *Opt. Lett.* **25**, 46–48 (2000).
- [6] M. G. L. Gustafsson, L. Shao, P. M. Carlton, C. J. R. Wang, I. N. Golubovskaya, W. Z. Cande, A. D. Agard, and J. W. Sedat, “Three-dimensional desolution doubling in wide-field fluorescence microscopy by structured illumination,” *Biophys. J.* **94**, 4957–4970 (2008).
- [7] L. Shao, P. Kner, E. H. Rego, and M. G. L. Gustafsson, “Super-resolution 3D microscopy of live whole cells using structured illumination,” *Nat. Methods* **8**, 1044–1046 (2011).
- [8] S. W. Hell and J. Wichmann, “Breaking the diffraction resolution limit by stimulated emission: stimulated-emission-depletion fluorescence microscopy,” *Opt. Lett.* **19**, 780–782 (1994).
- [9] E. Betzig, G. H. Patterson, R. Sougrat, O. W. Lindwasser, S. Olenych, J. S. Bonifacino, M. W. Davidson, J. Lippincott-Schwartz, and H. F. Hess, “Imaging intracellular fluorescent proteins at nanometer resolution,” *Science* **313**, 1642–1645 (2006).
- [10] M. J. Rust, M. Bates, and X. Zhuang, “Sub-diffraction-limit imaging by stochastic optical reconstruction microscopy (STORM),” *Nat. Methods* **3**, 793–795 (2006).

- [11] S. T. Hess, T. P. K. Girirajan, and M. D. Mason, “Ultra-high resolution imaging by fluorescence photoactivation localization microscopy,” *Biophys. J.* **91**, 4258–4272 (2006).
- [12] D. Li, L. Shao, B.-C. Chen, X. Zhang, M. Zhang, B. Moses, D. E. Milkie, J. R. Beach, J. A. Hammer, M. Pasham, T. Kirchhausen, M. A. Baird, M. W. Davidson, P. Xu, and E. Betzig, “Extended-resolution structured illumination imaging of endocytic and cytoskeletal dynamics,” *Science* **349**, aab3500 (2015).
- [13] K. Wicker, O. Mandula, G. Best, R. Fiolka, and R. Heintzmann, “Phase optimisation for structured illumination microscopy,” *Opt. Express* **21**, 2032–2049 (2013).
- [14] K. Wicker, “Non-iterative determination of pattern phase in structured illumination microscopy using auto-correlations in Fourier space,” *Opt. Express* **21**, 24692–24701 (2013).
- [15] E. Mudry, K. Belkebir, J. Girard, J. Savatier, E. Le Moal, C. Nicoletti, M. Allain, and A. Sentenac, “Structured illumination microscopy using unknown speckle patterns,” *Nature Photon.* **6**, 312–315 (2012).
- [16] R. Ayuk, H. Giovannini, A. Jost, E. Mudry, J. Girard, T. Mangeat, N. Sandeau, R. Heintzmann, K. Wicker, K. Belkebir, and A. Sentenac, “Structured illumination fluorescence microscopy with distorted excitations using a filtered blind-SIM algorithm,” *Opt. Lett.* **38**, 4723–6 (2013).
- [17] J. Min, J. Jang, D. Keum, S.-W. Ryu, C. Choi, K.-H. Jeong, and J. C. Ye, “Fluorescent microscopy beyond diffraction limits using speckle illumination and joint support recovery,” *Sci. Rep.* **3**, 2075 (2013).
- [18] A. Jost, E. Tolstik, P. Feldmann, K. Wicker, A. Sentenac, and R. Heintzmann, “Optical sectioning and high resolution in single-slice Structured Illumination Microscopy by thick slice blind-SIM reconstruction,” *PloS One* **10**, e0132174 (2015).
- [19] S. Dong, P. Nanda, R. Shiradkar, K. Guo, and G. Zheng, “High-resolution fluorescence imaging via pattern-illuminated Fourier ptychography,” *Optics Express* **22**, 20856–20870 (2014).
- [20] G. Zheng, R. Horstmeyer, and C. Yang, “Wide-field, high-resolution Fourier ptychographic microscopy,” *Nat. Photon.* **7**, 739–745 (2013).
- [21] M. G. Somekh, C. W. See, and J. Goh, “Wide field amplitude and phase confocal microscope with speckle illumination,” *Opt. Commun.* **174**, 75–80 (2000).
- [22] C. Ventalon and J. Mertz, “Quasi-confocal fluorescence sectioning with dynamic speckle illumination,” *Opt. Lett.* **30**, 3350–3352 (2005).
- [23] J. G. Walker, “Non-scanning confocal fluorescence microscopy using speckle illumination,” *Opt. Commun.* **189**, 221–226 (2001).

- [24] M. Liang, R. L. Stehr, and A. W. Krause, "Confocal pattern period in multiple-aperture confocal imaging systems with coherent illumination," *Opt. Lett.* **22**, 751–753 (1997).
- [25] Q. S. Hanley, P. J. Verveer, M. J. Gemkow, and T. M. Jovin, "An optical sectioning programmable array microscope implemented with a digital micromirror device," *J. Microsc.* **196**, 317–331 (1999).
- [26] R. Heintzmann, Q. Hanley, D. Arndt-Jovin, and T. Jovin, "A dual path programmable array microscope (PAM): simultaneous acquisition of conjugate and non-conjugate images," *J. Microsc.* **204**, 119–135 (2001).
- [27] P. J. Verveer, Q. S. Hanley, P. W. Verbeek, L. J. v. Vliet, and T. M. Jovin, "Theory of confocal fluorescence imaging in the programmable array microscope (PAM)," *J. Microsc.* **189**, 192–198 (1998).
- [28] P. Křížek, I. Raška, and G. M. Hagen, "Flexible structured illumination microscope with a programmable illumination array," *Opt. Express* **20**, 24585–24599 (2012).
- [29] A. G. York, S. H. Parekh, D. Dalle Nogare, R. S. Fischer, K. Temprine, M. Mione, A. B. Chitnis, C. A. Combs, and H. Shroff, "Resolution doubling in live, multicellular organisms via multifocal structured illumination microscopy," *Nat. Methods* **9**, 749–754 (2012).
- [30] D. Dan, M. Lei, B. Yao, W. Wang, M. Winterhalder, A. Zumbusch, Y. Qi, L. Xia, S. Yan, Y. Yang, P. Gao, T. Ye, and W. Zhao, "DMD-based LED-illumination Super-resolution and optical sectioning microscopy," *Sci. Rep.* **3**, 1116 (2013).
- [31] M. Guizar-Sicairos and J. R. Fienup, "Phase retrieval with transverse translation diversity : a nonlinear optimization approach," *Opt. Express* **16**, 9954–9962 (2008).
- [32] C. L. Luengo Hendriks, B. Rieger, M. van Ginkel, G. M. P. van Kempen, and L. J. van Vliet, *DIPimage: a scientific image processing toolbox for MATLAB* (Delft University of Technology, 1999).
- [33] S. A. Shroff, J. R. Fienup, and D. R. Williams, "Phase-shift estimation in sinusoidally illuminated images for lateral superresolution," *J. Opt. Soc. Am. A* **26**, 413–424 (2009).
- [34] N. Chakrova, B. Rieger, and S. Stallinga, "Development of a DMD-based fluorescence microscope," *Proc. SPIE* **9330**, 933008 (2015).
- [35] C. H. Righolt, J. A. Slotman, I. T. Young, S. Mai, L. J. van Vliet, and S. Stallinga, "Image filtering in structured illumination microscopy using the Lukosz bound," *Opt. Express* **21**, 24431–24451 (2013).
- [36] M. Ingaramo, A. G. York, E. Hoogendoorn, M. Postma, H. Shroff, and G. H. Patterson, "Richardson–Lucy Deconvolution as a General Tool for Combining Images with Complementary Strengths," *ChemPhysChem* **15**, 794–800 (2014).

- [37] E Ströhl and C. F. Kaminski, “A joint Richardson–Lucy deconvolution algorithm for the reconstruction of multifocal structured illumination microscopy data,” *Methods and Applications in Fluorescence* **3**, 014002 (2015).

4

DECONVOLUTION METHODS FOR STRUCTURED ILLUMINATION MICROSCOPY

We compare two recently developed multiple-frame deconvolution approaches for reconstruction of structured illumination microscopy (SIM) data: the pattern-illuminated Fourier Ptychography algorithm (piFP) and the joint Richardson-Lucy deconvolution (jRL). The quality of the images reconstructed by these methods is compared in terms of the achieved resolution improvement, noise enhancement and inherent artefacts. Furthermore, we study the issue of object-dependent resolution improvement by considering the modulation transfer functions derived from different types of objects. The performance of the considered methods is tested in experiments and benchmarked with that of a commercial SIM microscope. We find that the piFP method resolves equally well periodic and isolated structures, whereas the jRL method provides significantly higher resolution for isolated objects compared to the periodic ones. Images reconstructed by the piFP and jRL algorithms are comparable to the images reconstructed using the generalized Wiener filter applied in most commercial SIM microscopes. An advantage of the discussed algorithms is that they allow reconstruction of SIM images acquired under different types of illumination, such as multi-spot or random illumination.

Parts of this chapter have been published as N. Chakrova, B. Rieger, and S. Stallinga, JOSA A **33**, 12–20 (2016) [1].

4.1. INTRODUCTION

THE two main factors deteriorating image resolution in fluorescence microscopy are noise and the fundamental limitation of the optical system posed by diffraction. The blurring of an object caused by the Abbe diffraction limit is mathematically described as a convolution of this object with the point spread function (PSF) of the microscope, which is limited in bandwidth to spatial frequencies smaller than $2NA/\lambda$ (where λ is the fluorescence wavelength and NA is the numerical aperture of the microscope objective). The process of partially inverting this blur is referred to as deconvolution. Deconvolution has long remained one of the most popular methods to improve the quality of fluorescence microscopy images. Since the 1980s, numerous deconvolution microscopy methods were developed and extensive literature is available for their comparison [2–4]. In practice, the improvement in image quality achieved by 3D deconvolution of wide-field images can be on par with the improvement achieved in confocal microscopy.

Recent developments in fluorescence microscopy lead to a number of super-resolution techniques, which can provide substantially larger resolution improvement compared to widefield deconvolution microscopy [5]. One of these advanced methods is Structured Illumination Microscopy (SIM) [6–10]. SIM offers sectioning comparable to confocal microscopy and a resolution which is up to a factor of two better than the resolution in widefield microscopy. The set of raw images from which the final SIM image is reconstructed is generated by exposing the sample with a sequence of non-uniform illuminations. The acquired images are processed by a reconstruction algorithm, which depends on the type of applied non-uniform illumination, for providing the final high resolution SIM image.

In this study we compare two newly emerged reconstruction methods for SIM data: the joint Richardson-Lucy deconvolution (jRL) [11, 12] and the pattern-illuminated Fourier Ptychography (piFP) [13, 14]. Both methods can process SIM data acquired under any type of structured illumination and widefield detection. However, here we focus solely on the two most frequently used types - sinusoidal (line) and multi-spot illumination.

The sinusoidal excitation was used for the first demonstration of SIM and it still remains the most commonly used illumination mode due to its time efficiency. It provides the fastest SIM imaging, since only 15 sinusoidal illuminations are required for conventional 3D SIM reconstruction by the generalized Wiener filter. The accurate knowledge of the shift between the illuminations is essential for the generalized Wiener filter reconstruction [15]. Unfortunately, the noise in the images hampers precise estimation of this shift, which often leads to artefacts in the reconstructed image. Alternative reconstruction methods, which are based on a Bayesian treatment of the given inverse problem, may help to avoid the artefacts associated with the inaccurate shift of the spectral components [16–19]. The jRL and piFP algorithms applied to SIM measurements also fit within the Bayesian inversion framework. In fact, if only 2D imaging is considered, the piFP algorithm is identical to the maximum a posteriori probability image estimation algorithm described in Ref.[18], with the only difference in sequential instead of the simultaneous update of the images, and the form of applied regularization.

SIM with multi-spot illumination requires a larger number of excitation patterns, however, it provides better depth discrimination and, thereby, enables the imaging of thicker samples [20]. This variety of super-resolution SIM is closely related to the Image

Scanning Microscopy (ISM) – a method that is based on the combination of confocal microscopy and widefield detection [21, 22]. In order to speed up the acquisition and processing, ISM with multi-spot illumination was developed [20], and several different all-optical implementations of the ISM principle were realized [23–25]. In practice, ISM methods offer the lateral resolution which is about a factor of $\sqrt{2}$ better than the resolution in widefield microscopy, although in principle the spatial frequency bandwidth is increased with a factor of two. Deconvolution of the multi-spot SIM measurements by the jRL and piFP algorithms may be expected to yield the full factor of 2 resolution improvement over widefield microscopy, which is comparable to SIM. In this paper we formulate the generalized maximum likelihood estimation (MLE) treatment of the image reconstruction problem in SIM. Furthermore, we consider several particular cases of MLE applied in SIM, including the above mentioned jRL and piFP methods. The quality of the images reconstructed by these methods is compared in terms of the achieved resolution improvement, noise enhancement and inherent artefacts. One of the major differences between the piFP and jRL is in the underlying noise model: the piFP algorithm is derived assuming a read-out noise only model, whereas the jRL algorithm is derived assuming a shot noise only model. At the same time, the increasingly popular sCMOS cameras exhibit both types of noise. We study which of the algorithms would be best suited for these cameras. Finally, we benchmark the performance of the jRL and piFP algorithms with the generalized Wiener reconstruction from a state-of-the-art commercial SIM microscope.

4.2. THEORY

4.2.1. IMAGE RECONSTRUCTION IN SIM WITH MLE

IN SIM an object \hat{x} is imaged under a number of non-uniform illuminations p_i ($i = 1..N$). We model the image formation in SIM as a linear, shift-invariant process occurring in the presence of mixed Poisson-Gaussian noise. Each expected diffraction-limited image μ_i corresponding to illumination pattern p_i is described as follows:

$$\mu_i = (\hat{x} \cdot p_i) \otimes h, \quad (4.1)$$

where h is the PSF of the microscope and \otimes denotes the convolution operator. The actual acquired image d_i differs from the expected image by noise n :

$$d_i = (\hat{x} \cdot p_i) \otimes h + n. \quad (4.2)$$

We assume that the PSF is normalized to unity and that the sum of all illumination patterns is uniform:

$$\sum_{i=1}^N p_i = 1. \quad (4.3)$$

Image reconstruction in SIM can then be formulated as an inverse problem, where a high resolution object estimate x is calculated from a set of lower resolution object observations d_i ($i = 1..N$). The presence of noise and the finite spatial frequency bandwidth of the microscope's Optical Transfer Function (OTF) make this problem ill-posed and, hence, direct inversion of equation 4.2 does not lead to a unique solution. One of

the ways to handle such an ill-posed inverse problem is to apply a statistical approach in the form of maximum likelihood estimation (MLE). MLE has been previously used for SIM reconstruction under the assumption that only Gaussian noise [17–19] or only Poisson noise [12] is present in the acquired images. Here we formulate a generalized MLE treatment for the reconstruction in SIM, which takes into account both Poisson and Gaussian noise.

According to Bayes' theorem, the probability of an estimate x being the origin of the acquired data d_i is given by:

$$P(x|d_1, d_2, \dots, d_N) = \frac{P(d_1, d_2, \dots, d_N|x) \cdot P(x)}{P(d_1, d_2, \dots, d_N)}. \quad (4.4)$$

The sought-for high resolution SIM image is the estimate x which maximizes this probability, or, equivalently, minimizes its negative logarithm:

$$E = -\log P(d_1, d_2, \dots, d_N|x) - \log P(x) = L + F, \quad (4.5)$$

where we have omitted the logarithm of $P(d_1, d_2, \dots, d_N)$, since it does not depend on x . The first term of the error function E is the log-likelihood function L , which we will derive from the corresponding probability distribution. The probability distribution can be calculated as a convolution of the Poisson distribution, representing the shot noise, and the Gaussian distribution, representing the camera read-out noise. In order to simplify the calculations we use an analytical approximation to the mixed noise probability distribution, which was proposed by Huang et al. [26]:

$$P(d|\mu, \sigma^2) = \frac{e^{-(\mu+\sigma^2)} (\mu+\sigma^2)^{d+\sigma^2}}{\Gamma(d+\sigma^2+1)}. \quad (4.6)$$

Equation 4.6 describes the probability of observing an image d given the expected image μ and the variance of the read-out noise σ^2 . $\Gamma(t)$ stands for the Gamma function. Taking into account the whole set of acquired images d_i , the corresponding joint log-likelihood, which includes both noise types, is expressed as:

$$L = \sum_{i=1}^N [(\mu_i + \sigma^2) - (d_i + \sigma^2) \log(\mu_i + \sigma^2) + \log(\Gamma(d_i + \sigma^2 + 1))]. \quad (4.7)$$

The second term of equation 4.5 is the regularization function F that represents prior knowledge of the object. In practice it is used to overcome the ill-posed nature of the optimization problem in view of the band-limited OTF. Regularization functions can take various forms, depending on the available prior information about the object.

In order to find the ML estimate x , the error function E is minimized by a local iterative algorithm according to the following equation:

$$x^{k+1} = x^k - \beta^k \frac{\partial E}{\partial x^k}. \quad (4.8)$$

In case $F = 0$, the derivative of the error function with respect to x is calculated as:

$$\frac{\partial E}{\partial x} = \frac{\partial L}{\partial x} = 1 - \sum_{i=1}^N \left(\frac{d_i + \sigma^2}{\mu_i + \sigma^2} \otimes h^T \cdot p_i \right), \quad (4.9)$$

where it is used that the sum of all illumination patterns is uniform and that the PSF is normalized to unity. The transpose of the PSF is denoted as h^T .

The general MLE approach presented above can be transformed into different reconstruction algorithms depending on the noise characteristics of the acquired images, the choice of the regularization function F and the update step β . Despite having a common origin, these algorithms give rise to considerably different reconstructions. In the following sections we will discuss several particular cases of MLE applied to SIM reconstruction, which are derived for different noise models and various forms of the update β . In this work we restrict our considerations to non regularized problems ($F = 0$) and use early termination of the iterative reconstruction algorithms to obtain regularization.

4.2.2. PATTERN-ILLUMINATED FOURIER PTYCHOGRAPHY

Under the assumption of Gaussian noise the error function E takes the simplified least-squares form:

$$E = \frac{1}{2\sigma^2} \sum_{i=1}^N (d_i - \mu_i)^2. \quad (4.10)$$

The optimization of a least-squares function carried out according to equation 4.8 and using a constant step size β is nothing else than the steepest descent method.

If the update step of the steepest descent algorithm is split into three separate steps and the object is updated sequentially for each illumination pattern, one arrives at the pattern-illuminated Fourier Ptychography (piFP) algorithm [13]. The sequential update is expected to accelerate the convergence of the algorithm by a factor of N [27, 28]. In our earlier work we explained the connection between the steepest descent and the piFP algorithms and experimentally demonstrated the resolution improvement in 2D SIM by piFP [14]. The piFP algorithm can be also seen as a particular case of the Landweber method [29], extended for the case of multiple-image deconvolution. As a non regularized linear least squares method piFP provides a computationally simple solution to the given inverse problem.

4.2.3. JOINT RICHARDSON-LUCY DECONVOLUTION

The Richardson-Lucy (RL) algorithm was originally developed for restoration of a single blurred image, corrupted by Poisson noise [30, 31]. An update rule for the conventional RL algorithm is obtained by taking the step size β_{RL} equal to the local value of the sought-for object x :

$$x^{k+1} = x^k \cdot \left(\frac{d}{\mu} \otimes h^T \right). \quad (4.11)$$

Recently, Ingaramo et al. proposed to combine multiple images with complementary strengths through a joint Richardson-Lucy algorithm (jRL) [11]. This multiple-image jRL deconvolution was first used to reconstruct images in multi-spot SIM by Strhlohl et al. [12].

The update rule for the jRL algorithm in case of mixed Poisson-Gaussian noise is found by setting $\beta_{RL} = x$ in equations 4.8 and 4.9:

$$x^{k+1} = x^k \cdot \sum_{i=1}^N \left(\frac{d_i + \sigma^2}{\mu_i + \sigma^2} \otimes h^T \cdot p_i \right). \quad (4.12)$$

An advantage of using the mixed noise model instead of the Poisson noise model becomes apparent when acquired images have small photon counts, i.e. $d_i \ll \sigma^2$. In this case the update step 4.12 becomes idle and noise amplification for low signal levels is suppressed.

4.2.4. NEWTON-RAPHSON UPDATE STEP

The step size β can be modified in order to improve convergence speed of the steepest descent method. Such an improvement has been demonstrated in MLE SIM reconstruction with Barzilai-Borwein [18] and Newton-Raphson (NR) [14] approaches. According to the NR rule, the step size should be taken as the inverse of the diagonal part of the Hessian matrix: $\beta_{NR} = H^{-1}$. In case of mixed noise, the diagonal elements of the Hessian matrix are:

$$H = \frac{\partial^2 E}{\partial x^2} = \sum_{i=1}^N \left(\frac{d_i + \sigma^2}{(\mu_i + \sigma^2)^2} \otimes (h^T)^2 \cdot p_i^2 \right). \quad (4.13)$$

It is also possible to interpolate between the NR and jRL algorithms by choosing a diagonal update matrix which has different entries for each pixel:

$$\beta_{RLNR} = \frac{x}{\sqrt{1 + H^2 x^2}}. \quad (4.14)$$

In limiting cases this mixed step size reduces to NR and jRL updates:

$$\beta_{RLNR} = \begin{cases} x = \beta_{RL}, & \text{when } Hx \ll 1 \\ H^{-1} = \beta_{NR}, & \text{when } Hx \gg 1. \end{cases} \quad (4.15)$$

The interpolation algorithm deliberately uses a smaller step size than the jRL algorithm. Therefore, this interpolation algorithm is anticipated to be slower than the jRL algorithm, but is expected to outperform it in terms of noise suppression when acquired images are highly distorted by both Poisson and Gaussian noise.

4.3. SIMULATION RESULTS

IN order to test the performance of various MLE algorithms in simulations, we use a resolution target of 512×512 pixels containing different objects, such as points, crossing lines, uniform areas and periodic structures. The pixel size of the resolution target is taken equal to $\lambda/16NA$, where λ is the emission wavelength and NA - numerical aperture of the objective. The simulation is performed using a vectorial PSF [32, 33] which is calculated for $NA = 1.4$ and excitation/emission wavelengths of 488/518 nm.

Illumination patterns at the sample plane p_i are obtained by convolving the binary multi-spot patterns with the excitation PSF. A single binary multi-spot pattern is designed as an array of one-pixel spots arranged in a square lattice with periodicity of 12

pixels, which corresponds to a spatial frequency that is $2/3$ times the widefield diffraction limit at $2NA/\lambda$. This pattern is translated in steps of one pixel in order to form the full set of 144 multi-spot patterns and provide the uniform object illumination. The total intensity accumulated over all illuminations amounts to 2.5×10^4 photons per pixel. Gaussian read-out noise with equivalent variance of $\sigma^2 = 7$ photons and Poisson noise corresponding to the photon counts are added to each simulated image d_i . A separate widefield image is used as an initial estimate of the object under reconstruction. We found that a uniform object can also be used as initial estimate and leads to only minor changes in the outcome of the simulations.

In order to regularize the considered MLE problem, we terminate the iterative process before convergence to numerical precision. In the case of linear algorithms with the Gaussian noise approximation (piFP and NR with Gaussian noise model), we found 5 – 25 iterations to be optimal, since further increase of the number of iterations N_{iter} leads to highly visible noise amplification in the reconstructed images. The absolute error, calculated as the difference between the reconstructed image and the ground truth (averaged over all pixels), reaches $\sim 1.5 \times 10^3$ photons per pixel at the chosen stopping iteration. The algorithms which are based on the assumption of Poisson or mixed Poisson-Gaussian noise (jRL, interpolated jRL-NR, NR with mixed noise model) converge considerably slower. In order to reach absolute error levels similar to the one achieved in piFP algorithm, about 100-300 iterations have to be applied. We have chosen a fixed number of 200 iterations as stopping criterion for these algorithms. The computation takes on the order of 3-7 seconds per iteration (3.3 s for piFP, 4 s for jRL, and 7 s for jRL-NR) on an Intel Xeon E5-1620 v2 CPU with 3.70 GHz clock speed. The simulation is implemented in MATLAB (Mathworks, USA), the corresponding software package can be found at <http://www.diplib.org/add-ons>.

Examples of the images reconstructed using jRL and piFP algorithms are given in Fig. 4.1. The jRL reconstruction provides higher resolution improvement for point objects compared to the piFP reconstruction. However, the piFP reconstruction exhibits higher resolution in periodic structures. A major advantage of the jRL algorithm is the positivity constraint - the reconstructed image is always positive provided that the initial estimate did not have any negative values. The piFP reconstruction, on the contrary, results in a considerable number of non-physical negative values. Additionally, reconstruction artefacts in the form of amplified noise are more pronounced in piFP reconstruction. Ringing artefacts are characteristic to both methods, but are more expressed in jRL reconstruction. A combination of piFP and jRL methods can help to utilize the strengths of both algorithms. As seen in Fig. 4.1(e), by using an output of several piFP iterations as an initial estimate for the jRL algorithm, one can achieve higher resolution for both isolated and periodic objects.

4.3.1. QUANTITATIVE ASSESSMENT OF THE RECONSTRUCTED IMAGES

Quantitatively the quality of reconstructed images was evaluated by two parameters - the signal-to-noise ratio (SNR) in the uniform white area and the full width at half maximum (FWHM) of the point objects. The FWHM is calculated from the standard deviation of the Gaussian function fitted to the isolated point objects in the reconstructed images. It is important to note that the FWHM measure does not provide a complete representation

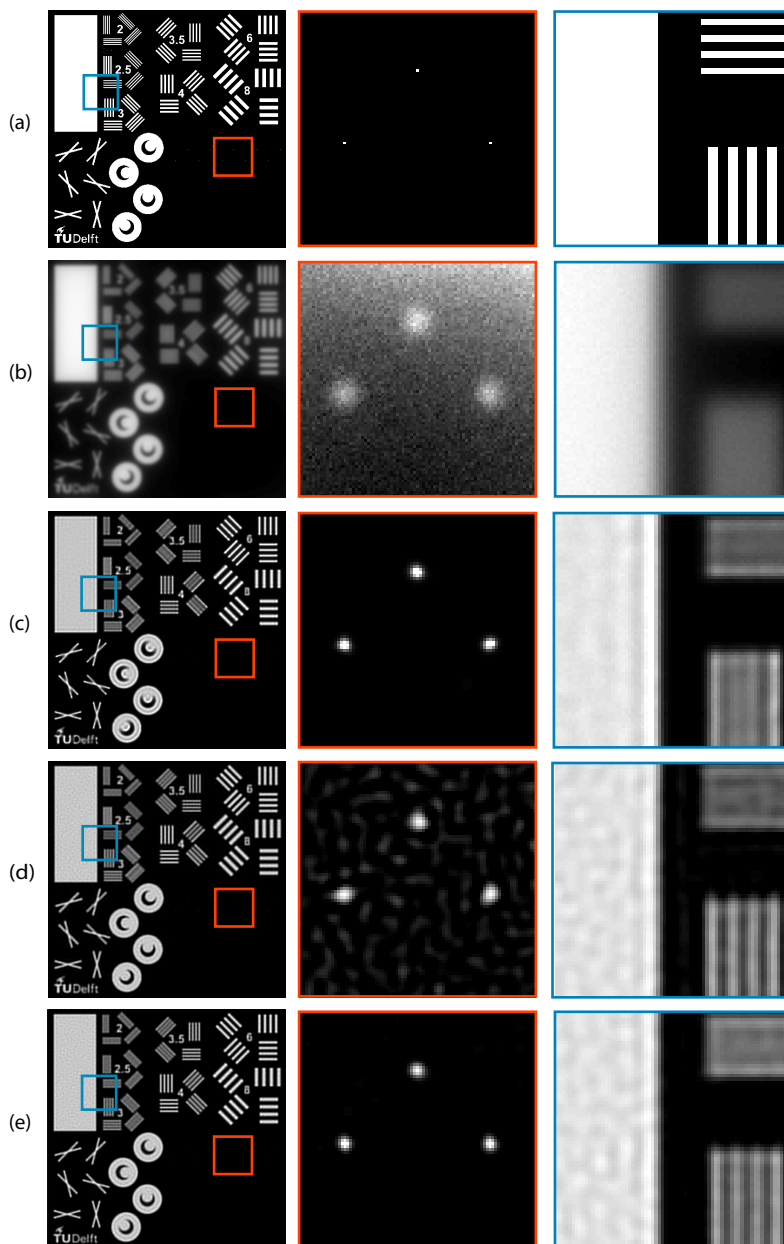


Figure 4.1: Comparison of the jRL and piFP algorithms in simulations. a) Simulated resolution target with 512×512 pixels of 23 nm. b) Widefield image. c) jRL reconstruction (200 iterations). d) piFP reconstruction (20 iterations), negative pixels are clipped. e) Combination of the jRL and piFP methods: the outcome of the 20 piFP iterations was used as an initial estimate for the 100 iterations of the jRL algorithm.

of resolution in the reconstructed image [34]; it can only be used as a resolution indicator for very sparse samples or well-isolated objects. The results for several MLE methods are summarized in Fig. 4.2.

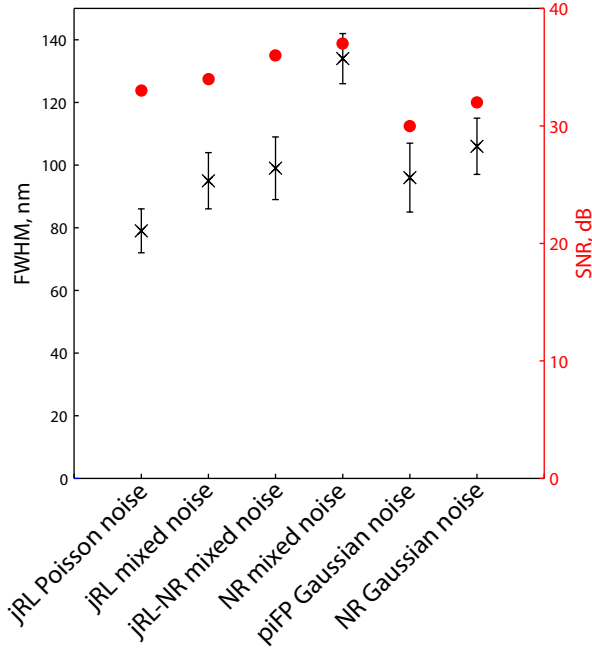


Figure 4.2: Quantitative comparison of various MLE methods. The FWHM is measured for point objects of the reconstructed resolution target and the SNR is measured in the bright uniform area of the reconstructed resolution target (shown in Fig. 4.1a). The relation between the SNR and the FWHM displays the trade-off between the image sharpening and noise amplification.

Assessment of the quality of reconstructed images is not a trivial task. There is no standard procedure that estimates how well the reconstructed image corresponds to the ground truth and how severe the reconstruction artefacts are. In this work we have chosen the so-called relative energy regain G [35] to further assess the performance of the reconstructions. The relative energy regain is calculated from the Fourier transforms of the ground truth of the object ($Object$) and the reconstructed image ($Estimate$), using the Holmes error energy ΔE [36]:

$$\Delta E = |Object - Estimate|^2, \quad (4.16)$$

$$G = \frac{|Object|^2 - \Delta E}{|Object|^2}. \quad (4.17)$$

The curves shown in Fig. 4.3 correspond to the profiles of the relative energy regain (vertical profiles at the horizontal spatial frequency component equal to zero). The shaded error bars show the standard deviation over the 50 different noise realizations. The

value of $G = 1$ corresponds to the ideal reconstruction, whereas negative values of the G profiles indicate artefact formation. As a linear method, piFP can not produce non-zero values beyond the theoretical frequency cutoff, therefore, the G function in case of the piFP reconstruction is close to zero in the region of spatial frequencies above $f_{cutoff} = 4NA/\lambda$. The nonlinear jRL method is not band-limited and will produce values above the theoretical frequency cutoff; some of these values will lead to errors, which results in a less smooth profile of the G function.

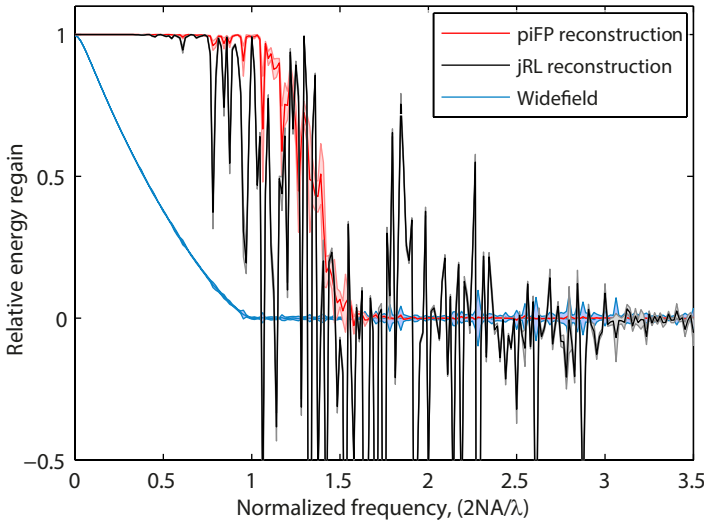


Figure 4.3: Profiles of the relative energy regain function in case of the piFP and jRL reconstructions are used for assessment of the reconstruction quality.

4.3.2. OBJECT-DEPENDENT RESOLUTION IMPROVEMENT

Simulated reconstructions of the resolution target indicate that the resolution improvement achieved with MLE methods can be object dependent. In order to study this phenomenon we have computed the Modulation Transfer Function (MTF), which characterizes the frequency content of the reconstructed image, in two distinct cases. First, a line with a thickness of one pixel ($\lambda/16NA$) was used as an object. The MTF was measured by taking the Fourier transform of a line profile in the reconstructed images. Figure 4.4 displays the resulting MTF curves for each iteration of the piFP(Fig.4.4a) algorithm and each 4th iteration of the jRL(Fig.4.4b) algorithm. These MTF curves represent the frequency content of isolated objects in the reconstructed images. The MTFs at the corresponding stopping iterations are shown in red. The dotted line indicates the theoretical frequency cut-off calculated from the pitch of the multi-spot illumination patterns and corresponding to 5/3 times the widefield diffraction limit of $2NA/\lambda$. In jRL reconstructions we observe non-zero MTF values beyond the theoretical frequency cut-off of SIM imaging ($f_{cutoff} = 4NA/\lambda$). Hence, out-of-band frequency recovery is possible for well-

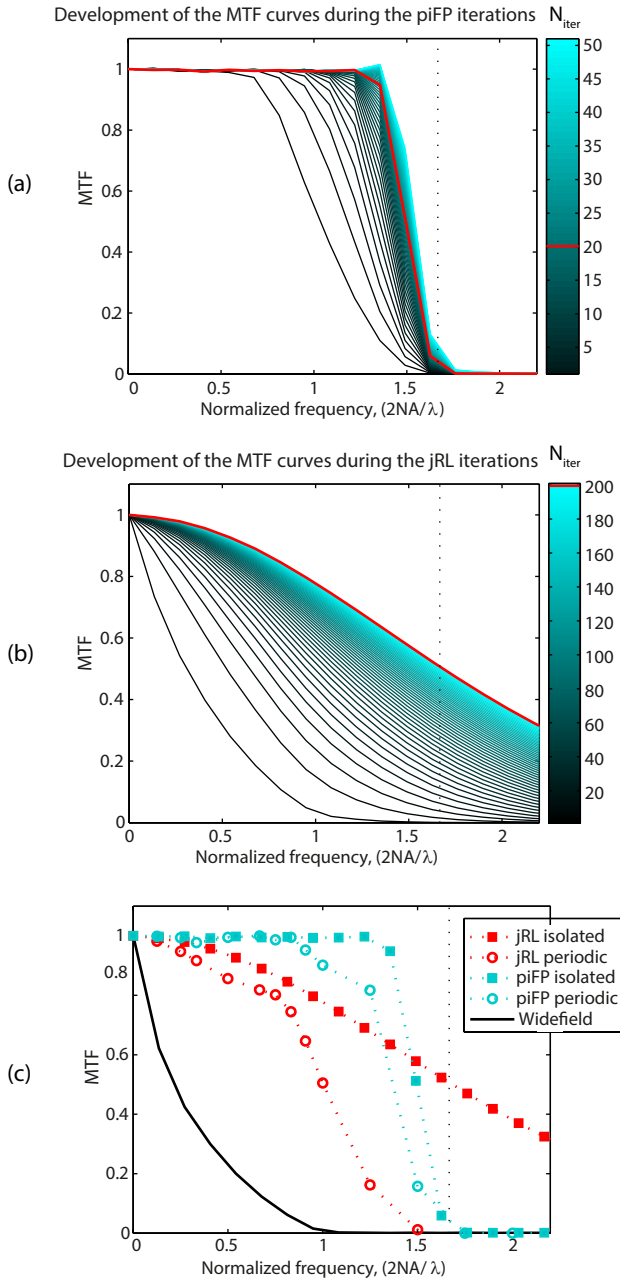


Figure 4.4: Development of the MTF curves which represent the frequency content of isolated objects during the piFP(a) and jRL(b) iterations. MTFs at the stopping iterations are shown in red. The dotted line indicates the theoretical frequency cut-off corresponding to the periodicity of the multi-spot illumination patterns. c) Object-dependent resolution improvement is visualized in the comparison of the "isolated" and "periodic" MTFs for jRL and piFP algorithms. MTF of the widefield image is given for reference.

separated objects. The reconstruction of out-of-band information has been previously described in the context of maximum likelihood deconvolution of widefield images, and originates from the available prior knowledge of the object [35].

Next, sine patterns with different spatial frequencies in the interval $[0, 4NA/\lambda]$ were used as objects. The modulation of sine patterns in the reconstructed images was measured at the stopping iteration. The resulting MTF curves represent the frequency content of periodic objects in the reconstructed images. The "periodic" MTF curves for jRL and piFP methods are compared to their "isolated" counterparts in Figure 4.4c. The piFP method resolves equally well periodic and isolated structures, whereas the jRL method provides considerably higher resolution in isolated objects compared to the periodic ones. The difference between the two MTF curves of the jRL method is particularly evident in the region above the widefield imaging frequency cut-off $f > 2NA/\lambda$. The shoulder at the normalized frequency of 0.6-0.9 in the "periodic" MTF curve of the jRL method is due to the artefact that appears as edge corrosion and sharpening of the peaks of the sine pattern.

4.4. EXPERIMENTAL RESULTS

EXPERIMENTAL data sets were acquired on a custom-built SIM setup - an inverted Olympus IX71 microscope complimented with a digital micro-mirror device (DMD) in the illumination path. Structured illumination is provided by the fast and flexible DMD, and fluorescence from the sample is recorded in a widefield mode by the sCMOS camera (Orca Flash 4.0, Hamamatsu Photonics, Japan). Further technical details about the optical design of the microscope can be found in our earlier work [37]. The following experimental parameters were used for imaging: $60\times/0.7$ objective, 488/520 nm excitation/emission wavelength, 108 nm camera pixel size and 137 nm DMD pixel size (back-projected to the sample plane). A fixed sample containing bovine pulmonary artery endothelial (BPAE) cells, in which F-actin is stained with Alexa Fluor 488 phalloidin (Invitrogen, CA, USA), is chosen as a test object. Multi-spot patterns with periodicity of 10 DMD pixels were used to illuminate the sample. The widefield image obtained by summing up the 100 raw images acquired by the sCMOS camera contains significant fixed pattern noise, which is found to have a negative impact on the reconstruction. In order to prevent this effect a uniform object was used as an initial estimate of the high resolution reconstruction. A comparison of the images reconstructed by the piFP (15 iterations) and the jRL (100 iterations) algorithms is given in Fig.4.5. Both reconstructed images display resolution improvement compared to the widefield image. At the same time, since the structure of the sample is fairly dense, the piFP method provides slightly higher resolution improvement than the jRL method.

4.4.1. READ-OUT NOISE OF THE sCMOS CAMERA

One of the properties of sCMOS cameras is the presence of pixel-dependent gain, read-out noise and offset. We measured the variance of the pixel-dependent read-out noise by taking the variance of the intensities for each pixel over 10^3 dark images. The standard deviation of the pixel-dependent read-out noise has a fixed pattern with mean value of $\sigma = 1$ photo-electron and a number of "hot" pixels ($\sim 0.3\%$ of all camera pixels) with a

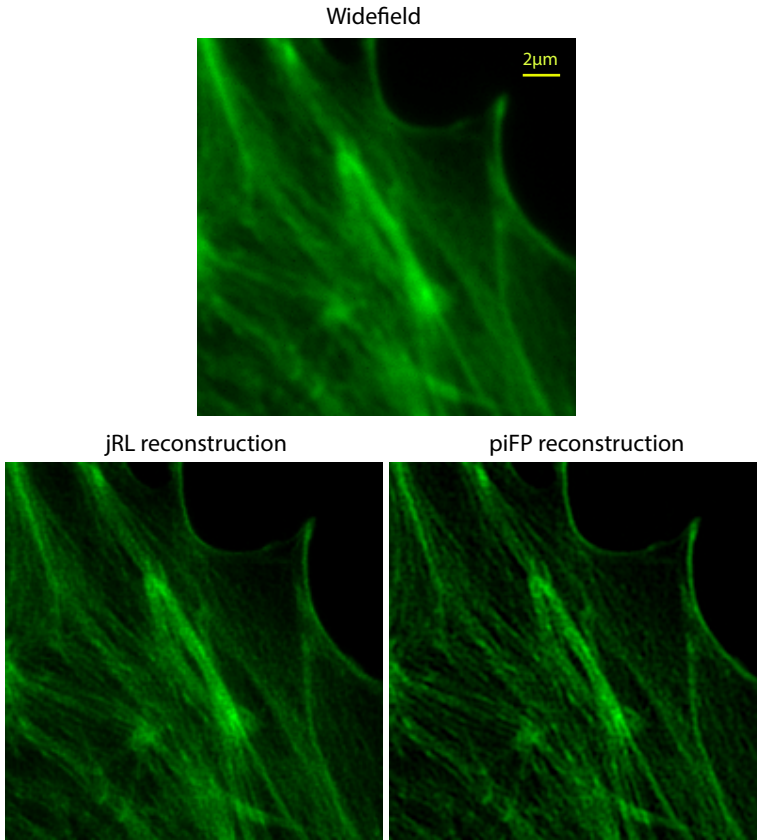


Figure 4.5: Comparison of SIM images reconstructed by jRL and piFP algorithms. A fixed sample containing BPAE cells, in which F-actin is stained with Alexa Fluor 488 phalloidin, was imaged using a $60\times/0.7$ air objective with DMD-based multi-spot illumination and sCMOS based image acquisition.

read-out noise on the order of $\sigma = 8 - 10$ photo-electrons. In order to examine to what extent the measured read-out noise standard deviation pattern of the sCMOS camera influences the reconstruction, we have tested the performance of the MLE algorithms with the mixed noise model (jRL and NR), where the uniform Gaussian noise variance was replaced by the measured fixed Gaussian noise variance pattern. As can be seen in Fig.4.6, applying the measured fixed noise pattern does not improve the reconstruction. On the contrary, the overall signal-to-noise ratio is deteriorated and, moreover, "hot" pixels of the read-out noise variance pattern result in circular artefacts. Hence, the spatially varying readout noise for sCMOS cameras is preferably not taken into account in the jRL or NR type of MLE algorithms.

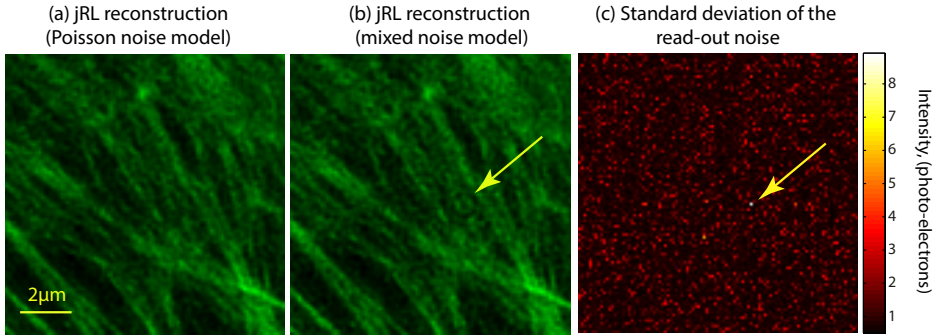


Figure 4.6: jRL reconstructions taking the spatially dependent readout noise variance of the sCMOS camera into account. a) Reconstruction with Poisson noise assumption. b) Reconstruction using the mixed noise assumption with the measured read-out noise variance pattern. Reconstructed image displays an overall deterioration of the SNR and circular artefacts caused by "hot" pixels in the read-out noise variance pattern (examples indicated by the yellow arrows). c) The measured read-out noise standard deviation pattern of the sCMOS camera.

4

4.4.2. COMPARISON TO THE PERFORMANCE OF COMMERCIAL SIM MICROSCOPE

Fixed BPAE cells stained with an anti- β -tubulin mouse monoclonal antibody for labeling microtubules (Invitrogen, CA, USA) were imaged with a Nikon N-SIM microscope. Imaging was performed using the 2D SIM mode, 488 nm excitation laser, $100\times/1.49$ objective and an EM-CCD camera with zero read-out noise (Andor iXon 897, Andor Technology, UK). The raw data from a Nikon N-SIM microscope was processed by the jRL and piFP algorithms and compared to the generalized Wiener reconstruction provided by the manufacturer. As can be seen in Fig.4.7, the performance of the presented MLE algorithms is comparable to the performance of the original N-SIM reconstruction. However, piFP and jRL algorithms produce slightly more noisy images with visible edge ringing, since no regularization or apodization was applied in these algorithms. The quality of SIM reconstructions depends on the sparsity of the sample, with dense parts of the sample being more strongly affected by noise amplification.

Although from this experiment there is no apparent advantage of using piFP or jRL algorithms for reconstruction of the line-SIM data, the benefit of these methods is that they allow reconstruction of SIM images acquired under different types of illumination, such as multi-spot or random (speckle) illumination.

4.5. CONCLUSION

WE formulated a generalized MLE approach to the image reconstruction problem in SIM, which takes into account both Poisson and Gaussian noise. The choice of update form in the iterative solution to the MLE problem, the noise model and the regularization function defines the exact form of the MLE algorithm. In this work we focused on two special cases - the recently developed piFP and jRL methods. These algorithms are based on different noise models and employ different update steps, which leads to

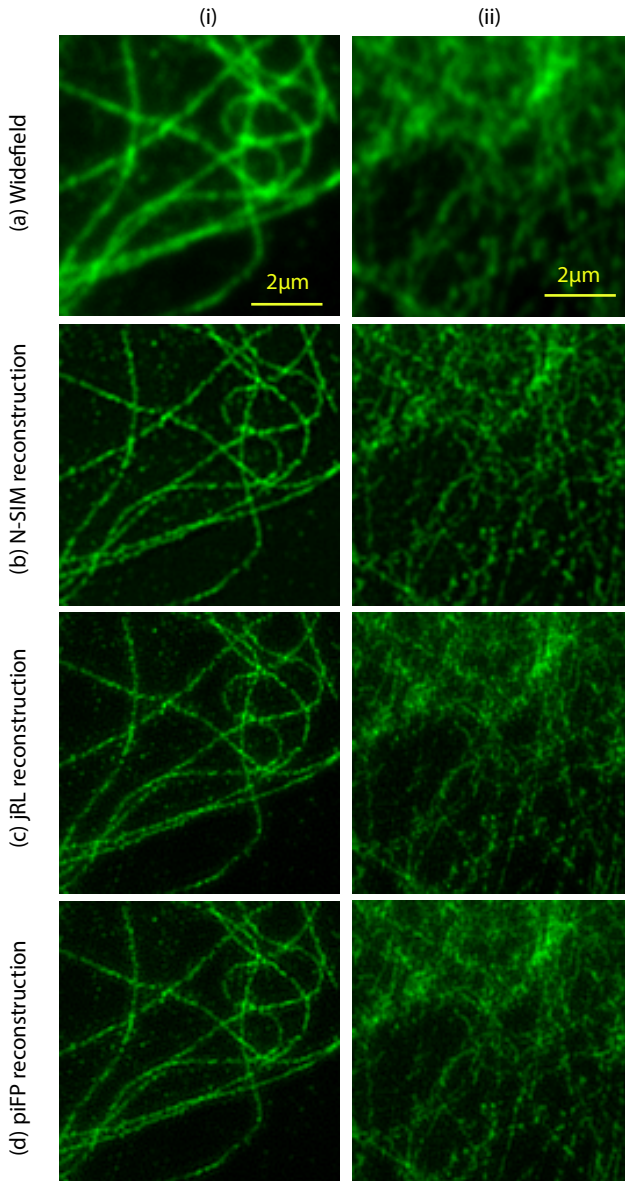


Figure 4.7: The performance of jRL (c) and piFP (d) algorithms is comparable to the performance of commercial Nikon N-SIM reconstruction (b). A fixed sample containing BPAE cells with labeled microtubules was imaged using a $100\times/1.49$ objective and an EM-CCD camera with zero readout noise. Top row (i) displays sparse part of the image, bottom row (ii) displays dense part of the image. A widefield image (a) is given for comparison.

substantial differences in the characteristics of the reconstructed images.

When jRL is applied, the apparent resolution improvement in periodic or dense objects is much smaller than the resolution improvement in well isolated objects, such as sparsely distributed points. This object-dependent resolution improvement is confirmed by studies of the MTF curves corresponding to these different types of objects. The MTF curve derived from the line response has higher values than the MTF curve derived from periodic objects. The difference is especially pronounced in the region beyond the widefield frequency cut-off, where jRL provides only marginal resolution improvement for periodic objects. At the same time, in sparse/isolated objects we observed the reconstruction of spatial frequencies beyond the theoretically predicted SIM cut-off frequency. Such reconstruction of out-of-band information is made possible by the prior information about the object.

4

In the case of piFP MTF curves for isolated and periodic objects are similar to each other, which leads to the conclusion that piFP provides uniform resolution improvement. In comparison to the jRL method, the resolution improvement achieved by applying piFP is lower in isolated objects and higher in periodic/dense objects.

Reconstruction artefacts are present in both methods. The piFP method produces a large amount of non-physical negative values and, additionally, results in higher noise amplification, since its MTF curves display higher values in the region between the widefield and SIM cut-off frequencies. The ringing artefact, which is inherent to both methods, can be explained by the sharp drop in the shape of the piFP MTF curves and jRL "periodic" MTF curve [38]. Early termination of the iterative process can be used to reduce the ringing effect at the expense of a smaller resolution improvement. Alternatively, a regularization function can be added to the iterative update algorithm.

Computationally, jRL reconstructions take approximately 5-10 times longer than piFP reconstructions, since on the order of 100-300 iterations are required for jRL, whereas 5-25 iterations are typically sufficient for piFP.

The final choice of the reconstruction algorithm depends on the object under study and on the type of noise that is dominant in the images. In case of very low photon counts, when the read-out noise becomes more significant, the algorithms based on the assumption of the Poisson noise will not perform well and algorithms with the Gaussian or mixed noise models should be applied. Finally, a well-matched regularization can enhance the reconstruction, reduce noise amplification and eliminate artefacts.

4.6. ACKNOWLEDGMENTS

We would like to thank Jan Keller-Findeisen for useful comments on this work and Jeremie Capoulade for assistance in acquiring N-SIM data. We also thank the reviewers of this paper for valuable suggestions. This research is supported by the Dutch Technology Foundation STW (<http://www.stw.nl/>).

REFERENCES

- [1] N. Chakrova, B. Rieger, and S. Stallinga, "Deconvolution methods for structured illumination microscopy," *J. Opt. Soc. Am. A* **33**, 12–20 (2016).

- [2] P. J. Verveer, M. J. Gemkow, and T. M. Jovin, "A comparison of image restoration approaches applied to three-dimensional confocal and wide-field fluorescence microscopy," *J. Microsc.* **193**, 50–61 (1999).
- [3] P. Sarder and A. Nehorai, "Deconvolution methods for 3-D fluorescence microscopy images," *IEEE Trans. Signal Process.* **23**, 32–45 (2006).
- [4] W. Wallace, L. H. Schaefer, and J. R. Swedlow, "A workingperson's guide to deconvolution in light microscopy," *BioTechniques* **31**, 1076–1097 (2001).
- [5] L. Schermelleh, R. Heintzmann, and H. Leonhardt, "A guide to super-resolution fluorescence microscopy," *J. Cell Biol.* **190**, 165–175 (2010).
- [6] M. G. L. Gustafsson, "Surpassing the lateral resolution limit by a factor of two using structured illumination microscopy," *J. Microsc.* **198**, 82–87 (2000).
- [7] R. Heintzmann and C. Cremer, "Laterally modulated excitation microscopy: improvement of resolution by using a diffraction grating," *Proc. SPIE* **3568**, 185–196 (1999).
- [8] J. T. Frohn, H. F. Knapp, and A. Stemmer, "True optical resolution beyond the Rayleigh limit achieved by standing wave illumination," *Proc. Natl. Acad. Sci. USA* **93**, 7232–7236 (2000).
- [9] G. E. Cragg and P. T. So, "Lateral resolution enhancement with standing evanescent waves," *Opt. Lett.* **25**, 46–48 (2000).
- [10] M. G. L. Gustafsson, L. Shao, P. M. Carlton, C. J. R. Wang, I. N. Golubovskaya, W. Z. Cande, A. D. Agard, and J. W. Sedat, "Three-dimensional desolution doubling in wide-field fluorescence microscopy by structured illumination," *Biophys. J.* **94**, 4957–4970 (2008).
- [11] M. Ingaramo, A. G. York, E. Hoogendoorn, M. Postma, H. Shroff, and G. H. Patterson, "Richardson–Lucy Deconvolution as a General Tool for Combining Images with Complementary Strengths," *ChemPhysChem* **15**, 794–800 (2014).
- [12] F. Ströhl and C. F. Kaminski, "A joint Richardson–Lucy deconvolution algorithm for the reconstruction of multifocal structured illumination microscopy data," *Methods and Applications in Fluorescence* **3**, 014002 (2015).
- [13] S. Dong, P. Nanda, R. Shiradkar, K. Guo, and G. Zheng, "High-resolution fluorescence imaging via pattern-illuminated Fourier ptychography," *Optics Express* **22**, 20856–20870 (2014).
- [14] N. Chakrova, R. Heintzmann, B. Rieger, and S. Stallinga, "Studying different illumination patterns for resolution improvement in fluorescence microscopy," *Opt. Express* **23**, 31367–31383 (2015).
- [15] K. Wicker, O. Mandula, G. Best, R. Fiolka, and R. Heintzmann, "Phase optimisation for structured illumination microscopy," *Opt. Express* **21**, 2032–2049 (2013).

- [16] F. Orieux, E. Sepulveda, V. Lorient, B. Dubertret, and J. C. Olivo-Marin, "Bayesian estimation for optimized structured illumination microscopy," *IEEE Trans. Image Process.* **21**, 601–614 (2012).
- [17] E. Mudry, K. Belkebir, J. Girard, J. Savatier, E. Le Moal, C. Nicoletti, M. Allain, and A. Sentenac, "Structured illumination microscopy using unknown speckle patterns," *Nature Photon.* **6**, 312–315 (2012).
- [18] T. Lukeš, P. Křížek, Z. Švindrych, J. Benda, M. Ovesný, K. Fliegel, M. Klíma, and G. M. Hagen, "Three-dimensional super-resolution structured illumination microscopy with maximum a posteriori probability image estimation," *Opt. Express* **22**, 29805–29817 (2014).
- [19] A. Jost, E. Tolstik, P. Feldmann, K. Wicker, A. Sentenac, and R. Heintzmann, "Optical sectioning and high resolution in single-slice Structured Illumination Microscopy by thick slice blind-SIM reconstruction," *PloS One* **10**, e0132174 (2015).
- [20] A. G. York, S. H. Parekh, D. Dalle Nogare, R. S. Fischer, K. Temprine, M. Mione, A. B. Chitnis, C. A. Combs, and H. Shroff, "Resolution doubling in live, multicellular organisms via multifocal structured illumination microscopy," *Nat. Methods* **9**, 749–754 (2012).
- [21] C. J. R. Sheppard, "Super-resolution in confocal imaging," *Optik* **80**, 53–54 (1988).
- [22] C. B. Muller and J. Enderlein, "Image Scanning Microscopy," *Phys. Rev. Lett.* **104**, 198101 (2010).
- [23] G. M. R. De Luca, R. M. P. Breedijk, R. Brandt, C. H. C. Zeelenberg, B. E. de Jong, W. Timmermans, L. N. Azar, R. Hoebe, S. Stallinga, and E. M. M. Manders, "Re-scan confocal microscopy: scanning twice for better resolution." *Biomed. Opt. Express* **4**, 2644–2656 (2013).
- [24] S. Roth, C. J. Sheppard, K. Wicker, and R. Heintzmann, "Optical photon reassignment microscopy (OPRA)," *Optical Nanoscopy* **2**, 1–6 (2013).
- [25] A. G. York, P. Chandris, D. D. Nogare, J. Head, P. Wawrzusin, R. S. Fischer, A. Chitnis, and H. Shroff, "Instant super-resolution imaging in live cells and embryos via analog image processing." *Nat. Methods* **10**, 1122–1126 (2013).
- [26] F. Huang, T. M. P. Hartwich, F. E. Rivera-Molina, Y. Lin, W. C. Duim, J. J. Long, P. D. Uchil, J. R. Myers, M. a. Baird, W. Mothes, M. W. Davidson, D. Toomre, and J. Bewersdorf, "Video-rate nanoscopy using sCMOS camera-specific single-molecule localization algorithms." *Nat. Methods* **10**, 653–658 (2013).
- [27] H. M. Hudson and R. S. Larkin, "Ordered Subsets of Projection Data," *IEEE Trans. Med. Imaging* **13**, 601–609 (1994).
- [28] F. Benvenuto, A. La Camera, C. Theys, A. Ferrari, H. Lanteri, and M. Bertero, "The study of an iterative method for the reconstruction of images corrupted by Poisson and Gaussian noise," *Inverse Probl.* **24**, 035016 (2008).

- [29] B. Eicke, "Iteration methods for convexly constrained ill-posed problems in Hilbert space," *Numer. Funct. Anal. and Optim.* **13**, 413–429 (1992).
- [30] W. Richardson, "Bayesian-based iterative method of image restoration," *J. Opt. Soc. Am.* **62**, 55–59 (1972).
- [31] L. Lucy, "An iterative technique for the rectification of observed distributions," *Astron. J.* **79**, 745–754 (1974).
- [32] T. Wilson, R. Juskaitytis, and P. D. Higdon, "The imaging of dielectric point scatterers in conventional and confocal polarisation microscopes," *Opt. Commun.* **141**, 298–313 (1997).
- [33] P. Török, P. D. Higdon, and T. Wilson, "Theory for confocal and conventional microscopes imaging small dielectric scatterers," *J. Mod. Opt.* **45**, 1681–1698 (1998).
- [34] R. P. J. Nieuwenhuizen, K. A. Lidke, M. Bates, D. L. Puig, D. Grünwald, S. Stallinga, and B. Rieger, "Measuring image resolution in optical nanoscopy," *Nat. Methods* **10**, 557–562 (2013).
- [35] R. Heintzmann, "Estimating missing information by maximum likelihood deconvolution." *Micron* **38**, 136–144 (2007).
- [36] T. J. Holmes, "Maximum-likelihood image restoration adapted for noncoherent optical imaging," *J. Opt. Soc. Am. A.* **5**, 666–673 (1988).
- [37] N. Chakrova, B. Rieger, and S. Stallinga, "Development of a DMD-based fluorescence microscope," *Proc. SPIE* **9330**, 933008 (2015).
- [38] C. H. Righolt, J. A. Slotman, I. T. Young, S. Mai, L. J. van Vliet, and S. Stallinga, "Image filtering in structured illumination microscopy using the Lukosz bound," *Opt. Express* **21**, 24431–24451 (2013).

5

ADAPTIVE STRUCTURED ILLUMINATION MICROSCOPY FOR PHOTBLEACHING REDUCTION

Photobleaching is a major factor limiting the observation time in fluorescence microscopy. We achieve photobleaching reduction in Structured Illumination Microscopy (SIM) by locally adjusting the illumination intensities according to the sample. Adaptive SIM is enabled by a digital micro-mirror device (DMD), which provides a projection of the grayscale illumination patterns. We demonstrate a reduction in photobleaching by a factor of three in adaptive SIM compared to the non-adaptive SIM based on a spot grid scanning approach. Our proof-of-principle experiments show great potential for DMD-based microscopes to become a more useful tool in live-cell SIM imaging.

Parts of this chapter have been submitted as N. Chakrova, A. Soler Canton, C. Danelon, S. Stallinga and B. Rieger to Biomed. Opt. Express (2016) [1].

5.1. INTRODUCTION

THE field of fluorescence microscopy experienced rapid development in the past two decades. A number of techniques that outperform standard widefield fluorescence microscope in terms of resolution were developed. These super-resolution methods can be roughly divided in three groups: localization microscopy, which relies on photo-switchable fluorophores and localization of single molecules [2–4], structured illumination microscopy, which employs a non-uniform illumination [5–10], and stimulated emission depletion microscopy (STED), which uses partial quenching of the fluorophores to narrow down the point spread function [11]. An ideal super-resolution fluorescence microscopy technique should allow biologists to observe live cells with improved resolution over extended periods of time. In reality, however, the resolution improvement is achieved at the cost of longer acquisition times, higher illumination intensities, or higher cumulative illumination doses. These conditions lead to enhanced photobleaching of the fluorophores and increased phototoxicity for the cells under study, which poses limitations on live-cell imaging. Therefore, deceleration of the photobleaching process is an important step for improvement of super-resolution microscopy.

In this work we address the issue of photobleaching reduction in Structured Illumination Microscopy (SIM). SIM is one of the most promising candidates for live-cell imaging amongst the super-resolution techniques [12–14]. It offers a rather modest resolution improvement of up to $2\times$ compared to standard widefield imaging (for linear SIM), however, it is compatible with most of the standard fluorescent dyes and requires less illumination light than localization microscopy or STED [15].

Unlike widefield microscopy, where the sample illumination is uniform, in SIM the sample is exposed to a series of non-uniform illumination patterns. The spatial frequency spectrum of the illumination patterns is convolved with that of the sample, which makes the high spatial frequency components of the sample observable. The final high resolution SIM image is reconstructed from the entire series of acquired images corresponding to the different illumination patterns used. Besides the classic line grid patterns, speckle[16] and multi-spot[17] patterns have been applied in various realizations of the resolution-doubling SIM.

In one of the SIM implementations a spatial light modulator (SLM) – it may be either a digital micro-mirror device (DMD) or a liquid-crystal-on-silicon SLM (LCOS-SLM) – is used for projection of the illumination patterns [17–19]. The SLM provides full spatial and temporal control over the illumination intensity. Although technically SLM also allows the projection of grayscale patterns, only binary SLM patterns have been used in SIM until now. Here we demonstrate how grayscale patterns can be used for reduction of the illumination intensity in DMD-based SIM microscopes.


The idea to reduce photobleaching and phototoxicity by locally adjusting the illumination intensity dose based on the sample structure was first implemented in confocal microscopy. An acoustic optical modulator was introduced into the illumination path of the confocal microscope to reduce the exposure time (and, hence, the illumination intensity) in the background and bright foreground areas of the sample [20, 21]. Another implementation was made in the Programmable Array Microscope (PAM) [22], a microscope which is equipped with an SLM in its primary image plane. PAM has a double-pass optical configuration, which means that both excitation and emission light pass through

the SLM [23, 24]. Multiple SLM illumination patterns are projected onto the sample during one camera exposure time. By applying binary masks to the projected SLM patterns, one can reduce the exposure time in certain areas of the sample. Both confocal and PAM implementations provide optically sectioned images with reduced photobleaching. Additionally, variations of adaptive illumination were used for improving the sensitivity in two-photon microscopy [25] and for photobleaching reduction in STED microscopy [26].

We bring the idea of reducing the photobleaching by locally adjusting the illumination intensity one step further and apply it to the resolution-doubling SIM microscopy. In our custom-built DMD-based microscope multi-spot illumination patterns are used together with a maximum-likelihood estimation reconstruction [27]. In order to regulate the illumination intensity dose, the multi-spot illumination patterns are weighed with a grayscale mask, which is calculated from an initial widefield image. We describe two grayscale mask designs and demonstrate experimentally the corresponding reduction in photobleaching. Our proof-of-principle experiments were conducted on fixed cells as a first step towards live-cell SIM imaging with reduced photobleaching.

5.2. PRINCIPLES OF ADAPTIVE SIM

THE problem of photobleaching in fluorescence microscopy can be addressed from two sides. At the stage of sample preparation, the robustness of fluorophores can be improved by suppressing their photobleaching pathways. This approach is fluorophore-specific and requires the understanding of photobleaching kinetics, which can easily become a rather complex problem [28]. Another way to address the issue is to reduce the overall illumination dose received by the sample. This approach is a universal measure that can be applied to all types of samples, regardless of the fluorescent dye and its photobleaching pathways. In this work we do not attempt to study the photobleaching behavior of the fluorophores, but seek to improve SIM by making it less aggressive for biological samples in terms of the amount of illumination light.

In order to reduce the overall illumination dose one can locally adjust either the exposure time or the illumination intensity. In our implementation the exposure time remains uniform over the whole field of view  the illumination intensity is adjusted by applying grayscale masks to the illumination patterns. Technically, this is performed by projecting grayscale images with the DMD. The intensities of the illumination patterns should have an inverse dependency on the sample brightness: the brighter the sample area, the lower the illumination intensity that will be applied to this area. Such an approach results in a more uniform signal-to-noise ratio (SNR) across the whole image (except for the background areas, where $\text{SNR} = 0$). In other words, SNR in bright regions of the image is sacrificed for the possibility to image the sample longer.

SIM images with adaptive grayscale illumination patterns are acquired in the following way. First, a widefield snapshot is taken at low intensity. A grayscale mask is calculated from this widefield image according to one of the schemes that will be described in section 5.2.1. The standard binary multi-spot illumination patterns are weighed with this mask image, and the SIM data is acquired with the resulting grayscale multi-spot illumination. The final SIM image is reconstructed using the pattern-illuminated Fourier Ptychography (piFP) algorithm, which is equivalent to non-regularized linear least-squares [27, 29]. For each time point in time-lapse SIM imaging a new widefield image is taken

and a new mask is calculated, in order to adapt the mask for possible changes and movements in the sample. A block diagram describing time-lapse adaptive SIM is shown in Fig.5.1.

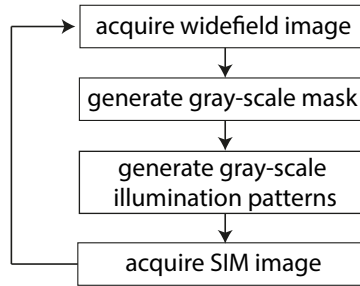


Figure 5.1: Block diagram of time-lapse adaptive SIM.

5

5.2.1. CALCULATION OF THE ILLUMINATION MASK

Various schemes can be used to generate grayscale masks for the illumination patterns. One of the most straightforward ways is to use a linear relationship between the intensities in the widefield image I and the weight of the grayscale mask w , as shown in Fig.5.2(a). The areas of the widefield image with intensities lower than I_{min} are identified as background, and the corresponding areas in the sample are not illuminated, i.e. weight of zero is applied in these areas. At the same time, lower limit for the weight w_{min} has to be set in order to avoid insufficient illumination of the brightest areas of the sample, corresponding to areas in the widefield image with intensities higher than I_{max} . The upper and lower boundary values for the intensity and weight have to be set empirically for a given sample.

In reality the relationship between the illumination intensity and the photobleaching rate is often nonlinear. An improved method for calculating the grayscale mask takes this fact into account by establishing inverse proportionality between the intensities in the widefield image and the weight of the grayscale mask as shown in Fig.5.2(b).

5.3. MATERIALS AND METHODS

5.3.1. EXPERIMENTAL SETUP

THE key element of our home-built SIM microscope is the DMD (Vialux, Germany). The DMD supports projection of 8-bit grayscale images at 290 Hz frame rate. The device is placed in the secondary image plane of an inverted widefield Olympus IX71 microscope. Structured illumination is generated by projecting illumination patterns of the DMD onto the sample via a demagnifying optical relay. Details on the design and layout of the optical setup can be found in our earlier work [30]. Experiments were performed using a $60\times/0.7$ air objective and 488/520 nm excitation and emission wavelengths. The sizes of the DMD pixel and the camera pixel back-projected to the sample plane are 137 nm and 108 nm, respectively.

The illumination pattern at the DMD is generated as an array of spots arranged in

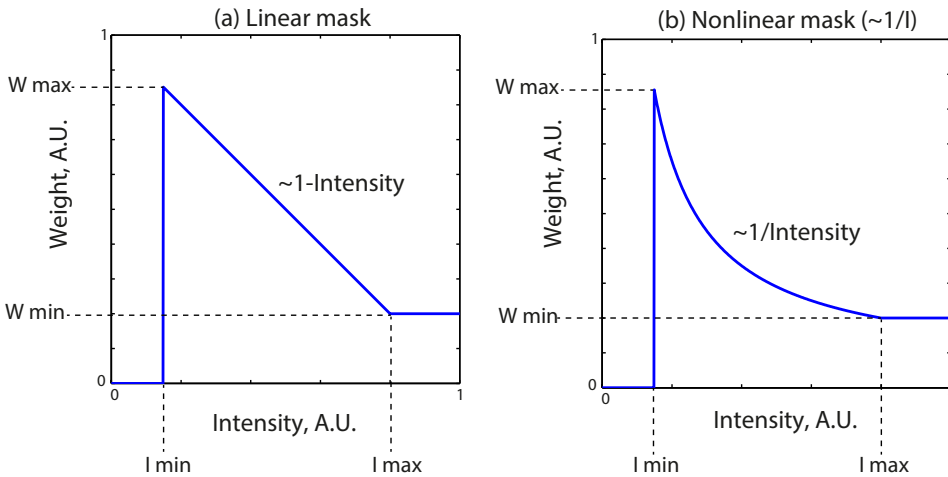


Figure 5.2: Two approaches for grayscale mask generation. In mask (a) the weight of the grayscale mask depends linearly on the intensities in the widefield image. In mask (b) the weight of the grayscale mask is inversely proportional to the intensities in the widefield image. Boundary values I_{min} and I_{max} are found empirically for a given sample.

a square grid with periodicity of 10 DMD pixels. This multi-spot pattern is translated with one DMD pixel per step and a camera frame is taken at each position of the pattern. The final SIM image is reconstructed from a dataset of 100 raw frames using the piFP algorithm, which is implemented in MATLAB (Mathworks, USA) in the same way as described in [27, 29].


5.3.2. MAPPING THE DMD ONTO THE CAMERA

For adaptive SIM it is essential to establish precise mapping between the DMD chip and the camera chip. This mapping is done by projecting a multi-spot illumination pattern onto a thin (~ 110 nm), spatially homogeneous fluorescent layer, which is produced as described in Ref.[31]. The resulting camera image contains an array of spots, each corresponding to a single DMD pixel. By extracting the coordinates of spots centers in the camera image we find the correspondence between DMD pixels and their image positions in the camera chip plane [30].

5.3.3. SAMPLE PREPARATION

Human Embryonic Kidney 293T (HEK 293T) cells were cultured on 100-mm plates (SARST-EDT) at 37 °C with 5% CO₂ in Dulbecco's modified Eagle's medium (DMEM, GIBCO) supplemented with 10% fetal bovine serum (FBS, GIBCO). At about 80% confluency the cells were washed once with phosphate-buffered saline (PBS, pH 7.4, GIBCO), treated with 0.25% trypsin-EDTA (Gibco) and collected in 1 mL of growth medium.

Methanol fixation and DNA staining were performed in the following way. Glass coverslips (#1.5, Menzel Glaser) were sterilized in 70% ethanol, washed with milli-Q water and dried. The coverslips were then incubated with 0.01% Poly-L-Lysine (PLL, Sigma

Aldrich) in PBS for 5 minutes at room temperature. PLL-coated coverslips were placed at the bottom of a six-well plate and 50 μL of the HEK 293T cell suspension were added. After 24 hours culture, the growth medium was removed, the cells were washed once with PBS and incubated for 10 minutes at room temperature with 100% methanol. After methanol fixation, the solvent was removed and the cells were washed once with PBS. Fixed cells were then incubated for 30 minutes at 37 $^{\circ}\text{C}$ with 0.2 U/ μL RNase ONE (Promega) to avoid background signal from labelled RNA and washed with PBS and Milli-Q water. DNA staining was performed by further incubating the cells at room temperature with PBS containing 0.1 μM SYTOX Green Nucleic Acid Stain (ThermoFisher Scientific) for 20 minutes in darkness. The cells were finally rinsed with PBS and Milli-Q water. Fixed samples were glued overnight to microscope slides (76 x 26 mm, Menzel-Glaser) with aqueous mounting medium (Sigma Aldrich) at room temperature in darkness. Samples were stored protected from light for up to two weeks at 4 $^{\circ}\text{C}$. 

5.4. EXPERIMENTAL RESULTS

5.4.1. PHOTBLEACHING BEHAVIOR OF THE FLUOROPHORE

IN order to demonstrate the photobleaching behavior of the SYTOX stain in HEK 293T cells sample, we have acquired photobleaching curves in widefield mode at different illumination intensities. The number of acquisitions scaled inversely proportional to the applied illumination intensity, so that each curve corresponded to an equal cumulative illumination dose received by the sample. As can be seen from Fig. 5.3, the photobleaching rate of the SYTOX stain depends nonlinearly on the illumination intensity. However, photobleaching curves corresponding to illumination intensities $I < 10 \text{ W/cm}^2$ largely coincide with each other, which indicates that the photobleaching rate scales linearly with the illumination intensity in this range.

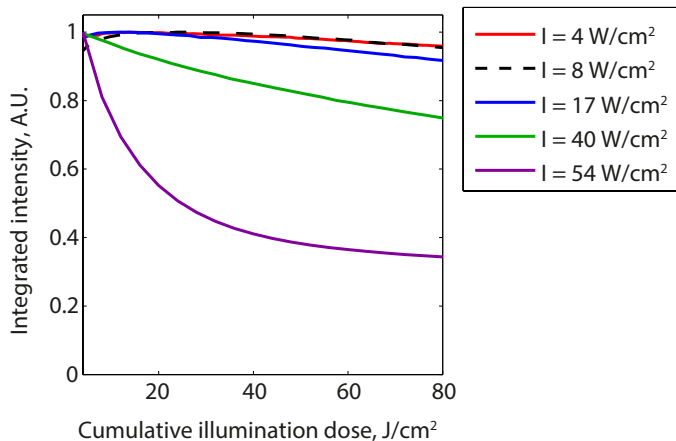


Figure 5.3: Photobleaching curves were acquired in a widefield mode at different illumination intensities on a sample containing HEK 293T cells in which the DNA was labeled with SYTOX green nucleic acid stain. In the region of illumination intensities 0 – 10 W/cm^2 photobleaching rate depends linearly on the illumination intensity. Additionally, a small self-quenching effect is observable at initial times due to the dense DNA labeling.

We have performed standard non-adaptive multi-spot SIM using an average intensity of approximately 0.08 W/cm^2 per multi-spot pattern. The average intensity used in adaptive SIM varies between $0.025\text{--}0.05 \text{ W/cm}^2$. Hence, we have operated in the region of linear photobleaching behavior of the fluorophore.

5.4.2. ILLUMINATION MASK EXAMPLES

For the generation of the grayscale masks we have employed the designs described in section 5.2.1. Here we present three examples in the decreasing order of the illumination dose that they impose on the sample. The linear mask shown in Fig.5.4(b) is calculated using the intensity normalized widefield image and the boundary values of $I_{min} = 10\%$ and $I_{max} = 85\%$. A lower illumination dose can be achieved with the same boundary values if the linear grayscale mask calculation is based on a normalized widefield image to which 15% percentile clipping is applied (Fig.5.4(c)). Finally, the nonlinear grayscale mask shown in Fig.5.4(d) results in the most light saving regime. This mask is calculated according to the $\sim 1/I$ scheme, using an intensity normalized widefield image and $I_{min} = 10\%$ and $I_{max} = 85\%$ boundary values.

Performances of the three masks were compared in the time-lapse imaging. In standard SIM the integrated intensity of the image is decreased by 64% after 30 minutes of time-lapse imaging. When adaptive SIM is used, the integrated intensity is decreased by only 46%, 35% and 28% for the masks shown in Fig.5.4 (b-d) respectively. As expected, a lower total illumination dose results in slower photobleaching of the sample. For our further experiments we have used the linear mask shown in Fig.5.4(c) and the nonlinear mask shown in Fig.5.4 (d).

5.4.3. IMAGE QUALITY IN ADAPTIVE SIM

In order to test the feasibility of the proposed method, we have compared adaptive SIM images to standard SIM images acquired under equal imaging conditions. The linear grayscale mask shown in Fig.5.4(c) was used as a weight for the multi-spot illumination patterns.

The reconstructed adaptive SIM image bears a strong visual resemblance to the standard SIM image, as can be seen in Fig.5.5(a). This visual resemblance is confirmed numerically by the structural similarity index *ssim* [32]. The *ssim* index between the standard and adaptive SIM equals 0.97, whereas the *ssim* index between two repeated standard SIM images equals 0.99. A decrease of 0.02 in *ssim* index roughly corresponds to adding Gaussian noise with a standard deviation of 0.5% of the maximum pixel value to the image.

The sum of all acquired images in the standard SIM dataset results in the widefield image, which confirms the uniformity of the overall illumination; whereas the sum of all acquired images in adaptive SIM dataset results in an image with a more uniform signal level, revealing the non-uniform overall illumination in this case. Moreover, the sum of all the acquired images is substantially less bright in adaptive SIM compared to the standard SIM, which indicates the reduction in overall illumination intensity specific to the adaptive SIM (see Fig.5.5(b)). Examples of standard and adaptive illumination patterns are given in Fig.5.5(c) for comparison.

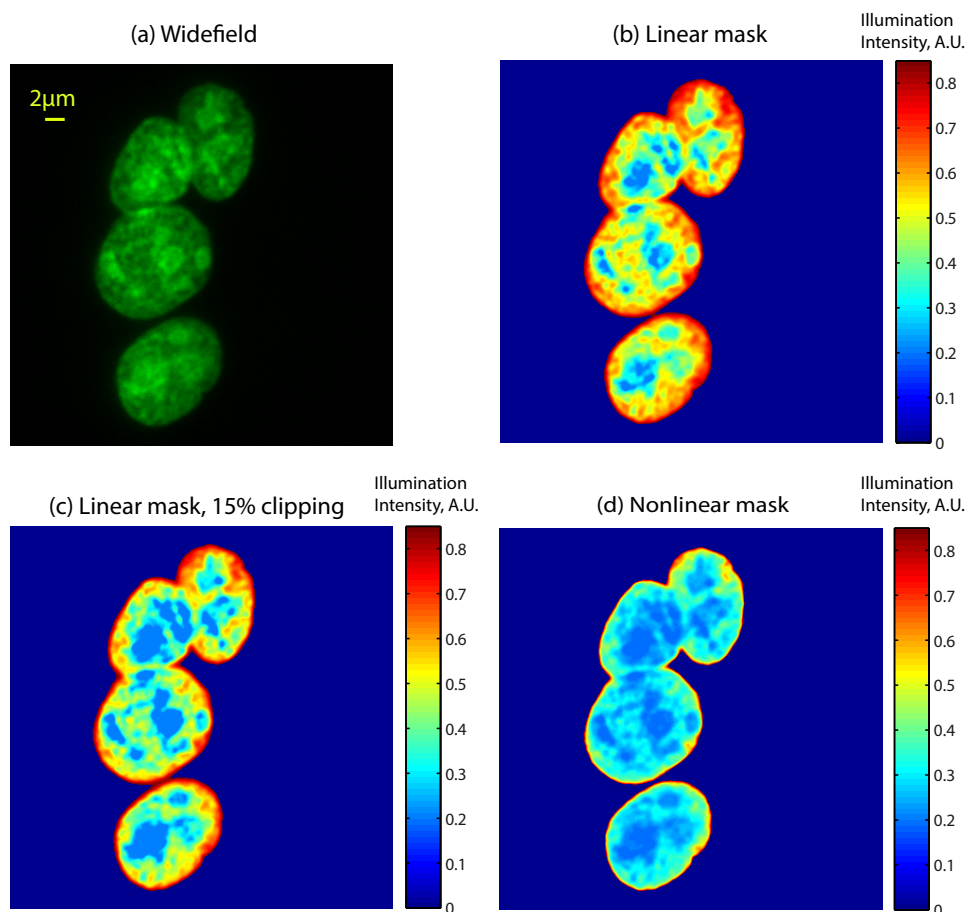


Figure 5.4: Widefield image of HEK 293T cells in which DNA is labelled with SYTOX stain (a), and the resulting grayscale masks (b-d), which can be used as a weight for the multi-spot illumination patterns.

5.4.4. PHOTBLEACHING STUDIES

The reduction in photobleaching was quantitatively assessed in time-lapse experiments. For each of the three imaging methods (standard SIM, adaptive SIM with linear mask and adaptive SIM with nonlinear mask) five separate sample areas were imaged over 30 minutes. During this time 60 SIM acquisitions were taken, with each SIM acquisition consisting out of 100 raw frames corresponding to the 100 multi-spot illumination patterns. The integrated image intensity per SIM acquisition is decreasing with time due to photobleaching of the fluorophores. The resulting photobleaching curves for the three methods are shown in Fig.5.6 to demonstrate the improvement in photobleaching reduction achieved by applying adaptive grayscale illumination patterns. In standard SIM the integrated image intensity is reduced by 35% after 20 acquisitions, whereas in adaptive SIM with the linear mask design it takes 60 acquisitions to induce the same bleach-

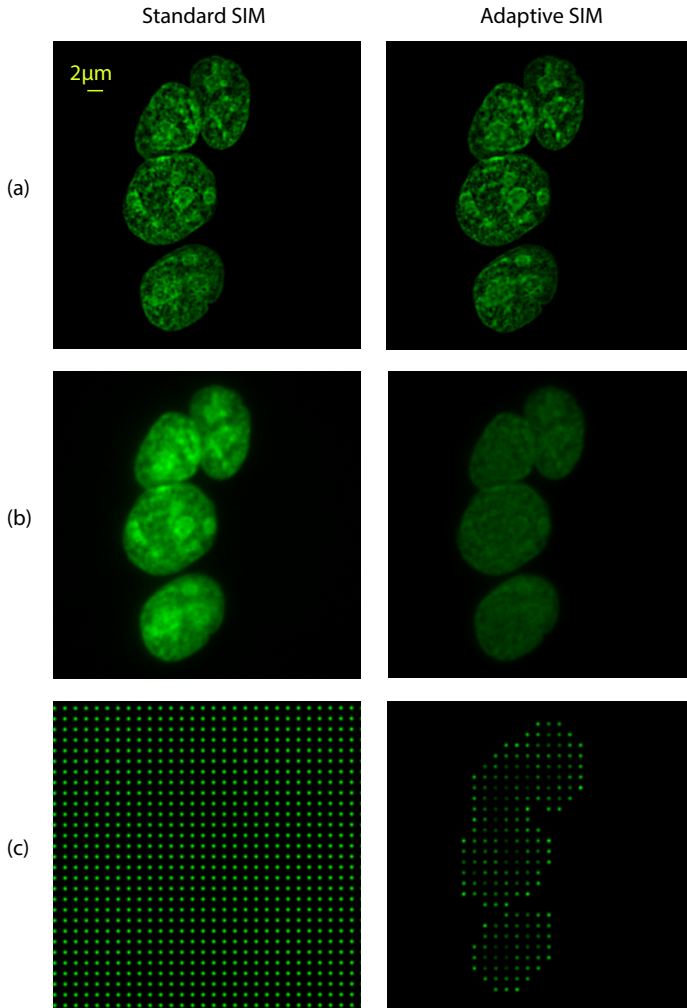


Figure 5.5: Comparison of standard and adaptive SIM imaging modalities. (a) Visual similarity of the adaptive and standard SIM images acquired under equal imaging conditions. (b) The sum of 100 raw images in standard SIM results in a widefield image, whereas the sum of 100 raw images in adaptive SIM results in an image with a more unified signal level. (c) Examples of the illumination patterns for the standard and adaptive SIM. Illumination patterns for the adaptive SIM are produced by multiplying the standard SIM illumination patterns with the mask shown in Fig.5.4 (c).

ing. Application of the nonlinear mask results in further improvements.

Examples of the reconstructed images for the three considered methods are given in Fig.5.7. Time-lapse reconstructions for adaptive SIM show only small reduction in the image brightness, unlike the reconstructions for standard SIM, in which the brightness is progressively reduced during the 30 minutes imaging time. The SIM images were reconstructed using 6 iterations of the piFP algorithm in the case of standard SIM and 40

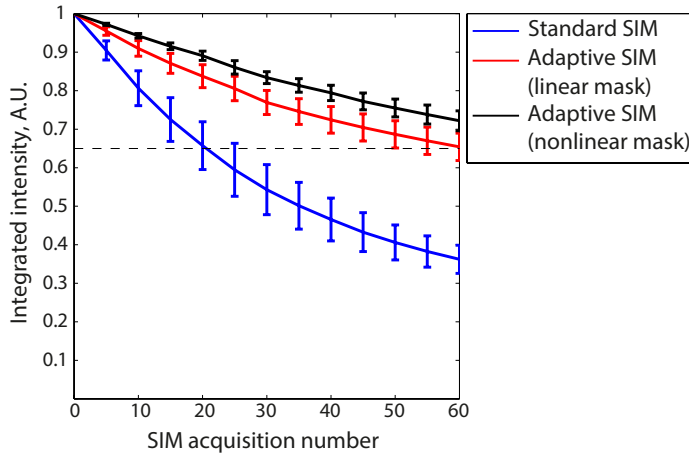


Figure 5.6: Comparison of photobleaching in standard and adaptive SIM. Each curve shows the average of 5 measurements on separate sample areas and the error bars indicate the standard deviations over 5 measurements. Adaptive SIM enables at least three times longer imaging than the standard SIM.

5

iterations of the piFP algorithm in the case of adaptive SIM.

5.4.5. THE INFLUENCE OF OUT-OF-FOCUS LIGHT

The sample under study has a 3D structure, and the fluorophores located outside the focal plane can be excited when the illumination pattern is projected onto the sample. In order to investigate the impact of the photons emanating from the out-of-focus planes on the measured photobleaching curves, we have applied pinholing to the acquired raw image data. The pinholing is done by multiplying each of the raw frames of the SIM acquisition with the corresponding illumination pattern, and leads to suppression of out-of-focus light. The difference between the photobleaching curves obtained from the original and the pinholed data is below 2% of the original integrated intensity. Therefore, we conclude that the same reduction in photobleaching is achieved in and out of focus, since cumulative light dose is equal in and out of focus and the bleaching rate scales linearly with the illumination intensity for the used range of intensities.

5.5. CONCLUSION

WE have demonstrated the use of grayscale illumination patterns of the DMD for lowering photobleaching in SIM. The overall illumination dose in SIM was reduced by adapting the grayscale illumination patterns to the sample structure.

A reduced illumination dose inevitably leads to a reduced SNR in the acquired images. However, the final reconstructions in adaptive SIM do not display significant degradation of the image quality compared to standard SIM. We have used the *ssim* measure in order to test their similarity. The degree of image deterioration in adaptive SIM is equal to adding Gaussian noise with a standard deviation of 0.5% of the maximum pixel value to the standard SIM reconstruction.

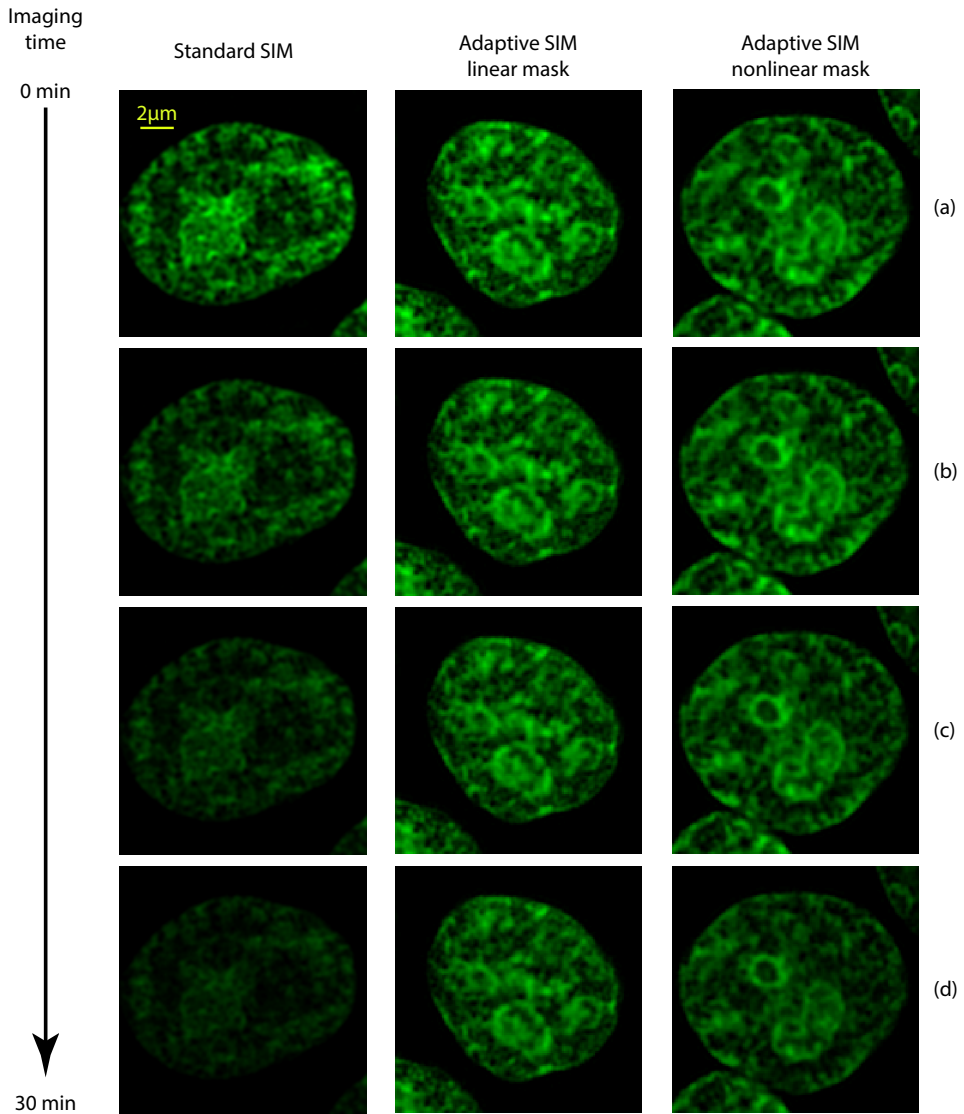



Figure 5.7: Comparison of the photobleaching induced by 30 minutes of time-lapse imaging in standard and adaptive SIM on HEK 293T cells, in which DNA is labelled with SYTOX stain. (a) First acquisition, (b) 20th acquisition (10 min), (c) 40th acquisition (20 min), (d) 60th acquisition (30 min). Adaptive SIM leads to deceleration of the photobleaching, enabling longer observation time of the sample. Intensities are comparable over all images.

We considered two schemes for the generation of adaptive patterns: with a linear and a non-linear dependence of the grayscale mask on the initial widefield intensity. The performance of adaptive SIM with both schemes was compared to standard SIM in time-lapse experiments on HEK 293T cells with SYTOX-stained DNA. The imaging time in adaptive SIM can be at least three times longer than in standard SIM because of the reduction in photobleaching. The nonlinear scheme for adaptive patterns generation provides a slightly bigger improvement than the linear scheme.

The degree of improvement achieved by adaptive SIM strongly depends on the sample structure and the fluorophore that is used. Adaptive SIM is expected to provide even bigger photobleaching reduction when applied in 3D imaging due to the generally higher sparsity of the sample in 3D than in 2D.

Moreover, the types of masks that are used to create adaptive illumination patterns may vary for different sample types. In order to support adaptive SIM imaging for a broad spectrum of sample types, various strategies for generation of the adaptive patterns have to be developed. For example, a mask based on a variance filter can be used to image samples with multiple nearly uniform objects or to study processes occurring at the border of such objects.

Finally, one of the potential pitfalls of adaptive SIM is non-uniform bleaching of the sample. Since the overall illumination in adaptive SIM is not uniform, the areas of the sample that receive a higher intensity will bleach faster than the other areas. Hence, adaptive SIM has to be applied cautiously in applications where precise quantitative analysis of the images is required 

5

5.6. ACKNOWLEDGEMENTS

We would like to thank Erik Manders and Ronald Breedijk for stimulating discussions on grayscale mask designs for adaptive SIM, and Chirlmin Joo lab (Delft University of Technology) for kindly providing the HEK 293T cells. This research is supported by the Dutch Technology Foundation STW (<http://www.stw.nl/>).

REFERENCES

- [1] N. Chakrova, A. Soler Canton, C. Danelon, S. Stallinga, and B. Rieger, “Adaptive illumination reduces photobleaching in Structured Illumination Microscopy,” submitted to Biomed. Opt. Express (2016).
- [2] E. Betzig, G. H. Patterson, R. Sougrat, O. W. Lindwasser, S. Olenych, J. S. Bonifacino, M. W. Davidson, J. Lippincott-Schwartz, and H. F. Hess, “Imaging intracellular fluorescent proteins at nanometer resolution,” *Science* **313**, 1642–1645 (2006).
- [3] M. J. Rust, M. Bates, and X. Zhuang, “Sub-diffraction-limit imaging by stochastic optical reconstruction microscopy (STORM),” *Nat. Methods* **3**, 793–795 (2006).
- [4] S. T. Hess, T. P. K. Girirajan, and M. D. Mason, “Ultra-high resolution imaging by fluorescence photoactivation localization microscopy,” *Biophys. J.* **91**, 4258–4272 (2006).

- [5] R. Heintzmann and C. Cremer, "Laterally modulated excitation microscopy: improvement of resolution by using a diffraction grating," *Proc. SPIE* **3568**, 185–196 (1999).
- [6] M. G. L. Gustafsson, "Surpassing the lateral resolution limit by a factor of two using structured illumination microscopy," *J. Microsc.* **198**, 82–87 (2000).
- [7] J. T. Frohn, H. F. Knapp, and A. Stemmer, "True optical resolution beyond the Rayleigh limit achieved by standing wave illumination," *Proc. Natl. Acad. Sci. USA* **93**, 7232–7236 (2000).
- [8] G. E. Cragg and P. T. So, "Lateral resolution enhancement with standing evanescent waves," *Opt. Lett.* **25**, 46–48 (2000).
- [9] C. B. Muller and J. Enderlein, "Image Scanning Microscopy," *Phys. Rev. Lett.* **104**, 198101 (2010).
- [10] G. M. R. De Luca, R. M. P. Breedijk, R. Brandt, C. H. C. Zeelenberg, B. E. de Jong, W. Timmermans, L. N. Azar, R. Hoebe, S. Stallinga, and E. M. M. Manders, "Re-scan confocal microscopy: scanning twice for better resolution." *Biomed. Opt. Express* **4**, 2644–2656 (2013).
- [11] S. W. Hell and J. Wichmann, "Breaking the diffraction resolution limit by stimulated emission: stimulated-emission-depletion fluorescence microscopy," *Opt. Lett.* **19**, 780–782 (1994).
- [12] P. Kner, B. B. Chhun, E. R. Griffis, L. Winoto, and M. G. L. Gustafsson, "Super-resolution video microscopy of live cells by structured illumination," *Nat. Methods* **6**, 339–342 (2009).
- [13] L. Shao, P. Kner, E. H. Rego, and M. G. L. Gustafsson, "Super-resolution 3D microscopy of live whole cells using structured illumination," *Nat. Methods* **8**, 1044–1046 (2011).
- [14] D. Li, L. Shao, B.-C. Chen, X. Zhang, M. Zhang, B. Moses, D. E. Milkie, J. R. Beach, J. A. Hammer, M. Pasham, T. Kirchhausen, M. A. Baird, M. W. Davidson, P. Xu, and E. Betzig, "Extended-resolution structured illumination imaging of endocytic and cytoskeletal dynamics," *Science* **349**, aab3500 (2015).
- [15] S. Cox, "Super-resolution imaging in live cells," *Dev. Biol.* **401**, 175–181 (2015).
- [16] E. Mudry, K. Belkebir, J. Girard, J. Savatier, E. Le Moal, C. Nicoletti, M. Allain, and A. Sentenac, "Structured illumination microscopy using unknown speckle patterns," *Nature Photon.* **6**, 312–315 (2012).
- [17] A. G. York, S. H. Parekh, D. Dalle Nogare, R. S. Fischer, K. Temprine, M. Mione, A. B. Chitnis, C. A. Combs, and H. Shroff, "Resolution doubling in live, multicellular organisms via multifocal structured illumination microscopy," *Nat. Methods* **9**, 749–754 (2012).

- [18] P. Křížek, I. Raška, and G. M. Hagen, “Flexible structured illumination microscope with a programmable illumination array,” *Opt. Express* **20**, 24585–24599 (2012).
- [19] D. Dan, M. Lei, B. Yao, W. Wang, M. Winterhalder, A. Zumbusch, Y. Qi, L. Xia, S. Yan, Y. Yang, P. Gao, T. Ye, and W. Zhao, “DMD-based LED-illumination Super-resolution and optical sectioning microscopy,” *Sci. Rep.* **3**, 1116 (2013).
- [20] R. A. Hoebe, C. H. Van Oven, T. W. J. Gadella, P. B. Dhonukshe, C. J. F. Van Noorden, and E. M. M. Manders, “Controlled light-exposure microscopy reduces photobleaching and phototoxicity in fluorescence live-cell imaging,” *Nat. Biotechnol.* **25**, 249–253 (2007).
- [21] R. A. Hoebe, H. T. M. Van der Voort, J. Stap, C. J. F. Van Noorden, and E. M. M. Manders, “Quantitative determination of the reduction of phototoxicity and photobleaching by controlled light exposure microscopy,” *J. Microsc.* **231**, 9–20 (2008).
- [22] W. Caarls, B. Rieger, A. H. B. De Vries, D. J. Arndt-Jovin, and T. M. Jovin, “Minimizing light exposure with the programmable array microscope,” *J. Microsc.* **241**, 101–110 (2011).
- [23] P. J. Verveer, Q. S. Hanley, P. W. Verbeek, L. J. v. Vliet, and T. M. Jovin, “Theory of confocal fluorescence imaging in the programmable array microscope (PAM),” *J. Microsc.* **189**, 192–198 (1998).
- [24] Q. S. Hanley, P. J. Verveer, M. J. Gemkow, and T. M. Jovin, “An optical sectioning programmable array microscope implemented with a digital micromirror device,” *J. Microsc.* **196**, 317–331 (1999).
- [25] K. K. Chu, D. Lim, and J. Mertz, “Enhanced weak-signal sensitivity in two-photon microscopy by adaptive illumination,” *Opt. Lett.* **32**, 2846–2848 (2007).
- [26] T. Staudt, A. Engler, E. Rittweger, B. Harke, J. Engelhardt, and S. W. Hell, “Far-field optical nanoscopy with reduced number of state transition cycles,” *Opt. Express* **19**, 5644–5657 (2011).
- [27] N. Chakrova, R. Heintzmann, B. Rieger, and S. Stallinga, “Studying different illumination patterns for resolution improvement in fluorescence microscopy,” *Opt. Express* **23**, 31367–31383 (2015).
- [28] L. Song, E. J. Hennik, I. T. Young, and H. J. Tanke, “Photobleaching kinetics of fluorescein in quantitative fluorescence microscopy,” *Biophys. J.* **66**, 2588–2600 (1995).
- [29] N. Chakrova, B. Rieger, and S. Stallinga, “Deconvolution methods for structured illumination microscopy,” *J. Opt. Soc. Am. A* **33**, 12–20 (2016).
- [30] N. Chakrova, B. Rieger, and S. Stallinga, “Development of a DMD-based fluorescence microscope,” *Proc. SPIE* **9330**, 933008 (2015).
- [31] J. M. Zwier, G. J. Van Rooij, J. W. Hofstraat, and G. J. Brakenhoff, “Image calibration in fluorescence microscopy,” *J. Microsc.* **216**, 15–24 (2004).

- [32] Z. Wang, A. C. Bovik, H. R. Sheikh, and E. P. Simoncelli, "Image quality assessment: From error visibility to structural similarity," *IEEE Trans. Sig. Process.* **13**, 600–612 (2004).

6

CONCLUSION

6.1. RESULTS

A demand for high resolution visualization tools in cell biology serves as a powerful incentive for fluorescence microscopy development. This ongoing development resulted in a number of super-resolution techniques, including SIM, that have matured and have been brought to the market. In this work we have considered an alternative SIM configuration, with DMD-based hardware and deconvolution-based image reconstruction. We have developed an optical design of a DMD-based microscope, taking into account the diffraction effects of the DMD. The optical quality of our microscope was estimated by the modulation transfer function obtained from an edge profile measurement (Chapter 2). The advantage of the DMD-based SIM is great flexibility in the choice of operational mode, which enabled us to examine different illumination patterns and reduce photo-bleaching. A detailed summary of the results of these studies and the comparison of the different reconstruction algorithms in SIM is given below.

6.1.1. OPTICAL SECTIONING IN A DMD-BASED SIM MICROSCOPE

Optically sectioned images can be obtained in SIM by using multi-spot illumination patterns and subsequent digital pinholing. We have experimentally proven that the sectioning capability, measured by the signal-to-background ratio, improves with increasing pitch and decreasing size of the digital pinhole (Chapter 2). However, the number of required raw images scales quadratically with the pitch. Therefore, the pitch has to be chosen large enough to avoid crosstalk between the pinholes, and, at the same time, sufficiently small to maintain reasonable temporal resolution of the microscope. Similar to standard confocal microscopy, the size of the pinhole establishes a user-defined compromise between the sectioning strength and the signal level in the image. As a rule of thumb, the size of the digital pinhole can be set to the diameter of the first dark ring of the Airy pattern.

6.1.2. RESOLUTION-DOUBLING IN A DMD-BASED SIM MICROSCOPE

When performing SIM with a DMD-based microscope one has to choose between various illumination and reconstruction options. In this thesis we have compared several illumination types (Chapter 3) and several reconstruction algorithms (Chapter 4).

The illumination patterns can be roughly divided into two groups – periodic and random. The quality of the image in case of periodic patterns depends on the pitch of the patterns, whereas in case of randomized patterns it depends on the sparsity and the number of pseudo-random patterns. Our simulations, for which only Poisson noise is taken into account, predict that dense pseudo-random patterns (with fill factor > 20%) result in higher noise amplification and lower resolution than sparse patterns. In practice, however, sparse pseudo-random patterns exhibit additional spiky noise, presumably due to insufficient averaging of the background intensity. As a consequence, both sparse and dense pseudo-random patterns result in much noisier images than periodic patterns. From this we conclude that SIM with speckle illumination is inferior to the standard stripe-based or multi-spot SIM in terms of image quality. This means that illumination patterns with strong peaks at high spatial frequencies (periodic patterns) provide better OTF support in the reconstructed images than illumination patterns with continuous decreasing frequency spectrum (pseudo-random patterns). Thus, in DMD-

based SIM pseudo-random patterns, which imitate speckle illumination, do not offer advantages over periodic illumination pattern types. However, speckle-based SIM implemented with a diffuser was originally intended to provide a SIM imaging solution with low cost and low hardware complexity. In this respect, SIM with speckle illumination can still prove to be useful.

The reconstruction algorithms can be split into two groups. The first group of algorithms only deals with illumination patterns that can be represented as a sum of discrete components in the Fourier domain. The final image can then be reconstructed by separating the components, placing them at their original positions in Fourier space and recombining them again. These methods cannot be used when the Fourier transform of the illumination pattern has a fairly large number of discrete components, which makes their separation practically difficult. The second group of methods treats the reconstruction problem in SIM as an inverse problem and seeks a solution by employing a noise model and carrying out the MLE of the corresponding likelihood function. These methods can process images acquired under any type of illumination, and due to this property were used in this thesis. Many different algorithms belong to this group, but, in fact, all of them can be derived using a common strategy. We devised a generalization of different MLE methods applied to SIM (Chapter 4.2). By choosing different noise models, update steps and regularization functions, this general formulation can be transformed into various reconstruction algorithms known from the literature, notably the piFP and the jRL algorithms. The choice of a specific algorithm depends on the parameters of the problem and available prior knowledge about the sample.

One of the most basic reconstruction algorithms is based on the steepest descent optimization of a quadratic error function and can be derived from the general MLE formulation using the Gaussian noise model and a constant update step (Chapter 4.2.2). We have shown that the piFP algorithm is identical to the steepest descent of the quadratic likelihood function with the only difference being the order of the applied object update (Chapter 3.2). In the steepest descent method, the sought-for object is updated once for all the raw acquisitions, while in the piFP algorithm the object is updated sequentially for each acquisition. This sequential update leads to faster convergence of the piFP algorithm. In a series of experiments, conducted on fluorescent beads and fixed cells, we have demonstrated that the piFP algorithm is a fast and computationally undemanding way to solve the reconstruction problem in SIM. In order to further speed up the convergence of the piFP algorithm we suggested to use Newton-Raphson (NR) update coefficients. Both simulations and experiments show a faster convergence when the NR update step is used. However, the piFP algorithm with NR update step is less stable and might lead to diverging solutions. The piFP algorithm with NR update coefficients can be recommended when a large number of raw images is used, for example, in speckle-based SIM.

Another algorithm, jRL, can be derived from the general MLE formulation by using the Poisson noise model and the Richardson-Lucy update step (Chapter 4.2.3). We have compared the performance of the jRL and piFP algorithms in simulations and experiments in terms of resolution improvement, reconstruction artefacts, and convergence speed. By analyzing the change in MTF curves as a function of the number of iterations in the piFP and jRL algorithms we drew the following conclusions. The resolution im-

provement for the piFP algorithm is uniform for different types of objects, whereas the resolution improvement for the jRL algorithm is object-dependent, with isolated objects, such as points or well separated thin lines, being better resolved than dense or periodic objects. Moreover, in the jRL reconstruction of well separated objects we have observed the interesting phenomenon of resolution improvement above the SIM frequency cutoff. Such an improvement is possible thanks to the a priori available information that the object is sparse. As a result, periodic or dense objects are better resolved in the piFP reconstruction, while point-like objects and thin lines are better resolved in the jRL reconstruction. One can benefit from both methods by combining them, for example by using an outcome of several piFP iterations as an initial estimate for the jRL algorithm.

We have demonstrated that analysis of the MTF curves is a useful approach that can serve not only to indicate the resolving capabilities of a particular algorithm, but also to interpret the potential causes of reconstruction artefacts. For example, the ringing artefacts, inherent to both methods, appear to be correlated to the sharp cutoff of the corresponding MTF curves.

In terms of convergence speed the piFP algorithm is 5-10 times faster than the jRL (it typically takes 0.1-1 min (3-20 iterations) for the piFP, and 6-10 min (100-150 iterations) for the jRL algorithm to converge). For the reconstruction of one 2D section this difference does not play a big role. However, in time lapse and/or 3D SIM imaging the speed of convergence becomes an important factor.

6.1.3. ADAPTIVE SIM

One of the main advantages of the SIM setup with an integrated DMD is the possibility to locally adjust the illumination light dose. For example, the illumination intensity can be adapted according to the brightness of the observed sample. Although the idea of such an adaptive illumination is not new and has been demonstrated in confocal and PAM microscopes, to our knowledge, it has not been applied to SIM before. In this work we have implemented adaptive illumination in multi-spot SIM (Chapter 5). With the help of adaptive illumination we have reduced the overall illumination light dose and, thereby, achieved photobleaching reduction. This has been quantified in time-lapse experiments performed on fixed cells by monitoring the decay of the integrated image intensity over time. For the sample under study, the observation time is increased at least three times in adaptive SIM compared to non-adaptive SIM. Furthermore, with the help of the structural similarity index we have verified that there is no significant degradation of the image quality in adaptive SIM compared to the non-adaptive case, although adaptive SIM images do have a lower SNR.

6.2. DISCUSSION AND OUTLOOK

6.2.1. FUTURE SIM

The performance of a DMD-based SIM microscope in optical sectioning or resolution-doubling imaging modes is similar to the performance of commercially available SIM and confocal microscopes. However, the fact that all these imaging modes can be combined within one optical instrument has potential economic value. It is possible that the next generation of SIM microscopes will indeed be equipped with a DMD rather than diffraction gratings. An advantage of the versatile DMD-based setup is that it can accommodate different objectives with minimum changes to the optical path. For example, in high throughput applications it can be interesting to use a lower-NA air objective in SIM mode in order to obtain a resolution on par with an oil immersion objective, while maintaining a large field of view (FOV) and the possibility of imaging large areas by scanning or patching multiple FOVs together. In a classical SIM setup, using lower-NA objectives would require an additional diffraction grating, while in a DMD-based setup the problem can be solved by simply changing the pitch of the projected illumination patterns. Apart from its flexibility, a DMD-based microscope offers the possibility of adaptive SIM imaging. Since photobleaching and phototoxicity are the main factors hampering long-time live cell imaging, the ability to reduce the illumination intensity without introducing significant image deterioration gives a DMD-based SIM configuration another serious advantage.

It is important to note, however, that line illumination patterns produced by the DMD and projected onto the sample via a microscope objective have lower modulation depth than similar sinusoidal patterns produced by two or three interfering beams from a diffraction grating. Decreased modulation depth of the illumination pattern leads to the degraded SNR of the images. As a result, SIM images acquired using sinusoidal patterns will have lower quality in a DMD-based setup compared to the standard SIM setup with an integrated diffraction grating. For this reason multi-spot patterns are preferred in DMD-based SIM setups. However, the number of required raw frames in multi-spot SIM is on the order of 100 and in SIM with sinusoidal illumination patterns it is only 9-25 frames per section (depending on the number of orientations and translations of the sinusoidal illumination pattern). Therefore, the temporal resolution of multi-spot SIM is inferior to that of standard SIM. Another way to solve the modulation depth problem in DMD-based SIM is to introduce an additional spatial frequency filtering step in order to filter out the dc-component of the diffracted field. This step, however, will complicate and possibly disable the adaptive SIM imaging mode.

Additionally, in a DMD-based SIM microscope the incidence angle of the illumination beam has to be adjusted in order to match roughly the blazed grating condition for the used wavelength. This issue is not prohibitive for multi-color SIM, but it has to be taken into account in the experimental setup. In a classical SIM setup the change of the illumination wavelength is not associated with any changes in the optical path.

6.2.2. DEVELOPMENTS IN DECONVOLUTION

In this thesis we restricted our consideration on MLE methods for image reconstruction in SIM to non-regularized problems. However, in the majority of cases some information about the imaged structure, such as positivity or sparsity, is available in advance. This information can be used in the form of a regularization function in order to enhance the resolution and reduce or equalize the noise amplification in the reconstructed images.

Furthermore, sparsity of the images can be exploited in a different imaging method using the compressive sensing (CS) framework. According to the theory of CS, it is possible to reconstruct sparse signals from measurements with less sampling points than dictated by the classical Nyquist-Shannon theorem [1]. Current implementations of the CS principle in fluorescence microscopy are based on DMD-modulated illumination and single-pixel detection [2, 3]. In these implementations the use of expensive scientific cameras is avoided, however, this feature comes at the cost of increased image acquisition times. Since fast imaging is a highly desirable feature in live-cell fluorescence microscopy, we anticipate that further developments in the field of compressive microscopy will target image acquisition speed and the related illumination dose.

6.2.3. COMPARISON TO SELECTIVE PLANE ILLUMINATION MICROSCOPY

Since SIM is well-suited for live-cell imaging at high resolution, it is useful to compare it to another fluorescence microscopy technique designed for imaging living specimens – the selective plane illumination microscopy (SPIM). In SPIM, a thin plane illumination and widefield detection are used to achieve optical sectioning [4]. The lateral resolution in SPIM is equal to the resolution of a standard widefield microscope, and the axial resolution depends of the thickness of the illumination plane, which is typically 1-4 μm thick (the thickness is defined by the NA of the illumination objective, which cannot be high due to the required working distance). However, in cases when the sample can be rotated and observed under different angles, the tomographic reconstruction of the SPIM data provides an almost isotropic overall resolution [5, 6].

SPIM has a number of very strong characteristics. First of all, since the illumination volume in SPIM is reduced to one plane at a time, a great reduction in photobleaching can be achieved (SPIM uses 1-3 orders of magnitude lower light dose than confocal microscopy [7]). Next, since the whole plane is illuminated simultaneously, SPIM has a high temporal resolution (image acquisition speed in SPIM is 10 to 1000 frames per second [7], which is 10 to 1000 times faster than in SIM). Moreover, in SPIM it is possible to observe 3D specimens with a thickness of several millimeters. These beneficial features for imaging living samples come at the expense of a rather poor spatial resolution. In applications where spatial resolution can be sacrificed for better temporal resolution and lower photobleaching, SPIM is preferred to SIM. Therefore, SPIM is mostly used to study large living specimens, for example, in developmental biology. However, the combination of SIM with SPIM may expand the scope of its use to single cell imaging [8–10].

6.2.4. IMAGE QUALITY ASSESSMENT

An unresolved issue in fluorescence microscopy in general and in SIM microscopy in particular is the assessment of image quality. Interpretation of the images is a complex matter and often turns out to be very subjective. Since a universal procedure to judge

the resolution and the overall quality of the final image does not exist, in an attempt to provide verifiable image comparison microscopists judge the image quality based on several separate parameters, such as SNR, PSF, presence and severity of artefacts, etc. A parameter which is commonly used to represent the resolution in fluorescence microscopy is the FWHM of the PSF. The FWHM is often obtained from point-like objects, such as fluorescent beads with sub-diffraction size [11]. As has been shown in this thesis (Chapter 4), some reconstruction methods provide object-dependent resolution improvement. Therefore, super-resolution methods which involve a deconvolution step often perform significantly better on particular structure types, such as isolated points or thin filaments. Using one FWHM criterion to judge the overall resolution that the method provides can be unfair and even misleading in this case.

In order to improve the situation, a considerable effort should be put in developing universal criteria that are truly representative of the image quality. Promising developments in this direction are the resolution measures which are based on the Fourier Ring Correlation (FRC) [12, 13] and the spectral signal-to-noise ratio [14]. The FRC resolution concept, which was first used in the field of cryo-electron microscopy, implies measurement of the correlation between the Fourier Transforms of independent noise realizations of the same object. This measure was recently successfully implemented for resolution assessment in localization microscopy [15], and may be extended to other super-resolution methods. In the case of SIM, the FRC resolution can be computed from two images of the same sample area with different noise characteristics.

Additionally, we expect that fluorescent resolution targets with sufficiently fine structures will become commonplace to accommodate standardized image quality measurements in the near future [16].

6.2.5. SUGGESTIONS FOR FOLLOW-UP RESEARCH IN ADAPTIVE SIM

Adaptive SIM is a very promising emerging method. The photobleaching reduction effect in adaptive SIM strongly depends on three factors: sample structure, fluorophore in use, and the implementation of the adaptivity of the illumination patterns. In this thesis we have demonstrated adaptive SIM on fixed HEK293T cells in which DNA was labeled with SYTOX stain, and considered two different implementations of adaptivity. Although the first results are very positive, a thorough follow-up study is required in order for adaptive SIM to become a reliable technique for photobleaching and phototoxicity reduction. To that end the following studies can be recommended:

1. The design of adaptive illumination patterns has to be tailored to the sample type (such as filamentous, dotted, dense, etc.). Therefore, different strategies for the generation of adaptive illumination patterns have to be developed in order to create a bank of possible adaptive illumination designs for different sample types.
2. Since a significant spread in the efficiency of the method is expected for different samples, it is useful to quantify the photobleaching reduction for the different sample types and commonly used fluorophores.
3. A comprehensive comparison of the image quality in adaptive SIM and non-adaptive SIM should be done.

4. Adaptive SIM should be extended to 3D imaging, as it is expected to provide an even bigger gain in this modality.
5. Since the overall illumination in adaptive SIM is not uniform, some areas of the sample receive higher light dose and, therefore, bleach faster than other areas of the sample. If the information about the photobleaching dynamics of the fluorophore is available, a correction for non-uniform photobleaching can be implemented in the adaptive SIM image reconstruction.
6. An important parameter in live-cell SIM imaging is the temporal resolution, since insufficiently fast imaging can lead to motion artefacts in the reconstructed images or simply fail to capture the fast biological processes. The sinusoidal illumination patterns offer better temporal resolution than the multi-spot illumination patterns, therefore, implementing adaptive SIM with sinusoidal illumination patterns would be extremely useful in the view of live-cell imaging. However, it is not clear if such an implementation is possible, and if so, how complex the required setup would have to be.

REFERENCES

- [1] E. J. Candès and M. B. Wakin, "An introduction to Compressive Sampling," *IEEE signal Processing Magazine* pp. 21–30 (2008).
- [2] Y. Wu, P. Ye, I. O. Mirza, G. R. Arce, and D. W. Prather, "Experimental demonstration of an Optical-Sectioning Compressive Sensing Microscope (CSM)," *Opt. Express* **18**, 24565–24578 (2010).
- [3] V. Studer, J. Bobin, M. Chahid, H. Shams, and E. Candès, "Compressive fluorescence microscopy for biological and hyperspectral imaging," *Proc. Natl. Acad. Sci. USA* **109**, 1679–1687 (2012).
- [4] J. Huisken, J. Swoger, F. D. Bene, J. Wittbrodt, and E. H. K. Stelzer, "Optical Sectioning deep inside live embryos by Selective Plane Illumination Microscopy," *Science* **305**, 1007–1009 (2004).
- [5] J. Swoger, J. Huisken, and E. H. K. Stelzer, "Multiple imaging axis microscopy improves resolution for thick-sample applications," *Opt. Lett.* **28**, 1654–1656 (2003).
- [6] P. J. Verveer, J. Swoger, F. Pampaloni, K. Greger, M. Marcello, and E. H. K. Stelzer, "High-resolution three-dimensional imaging of large specimens with light sheet – based microscopy," *Nat. Methods* **4**, 311–313 (2007).
- [7] E. H. K. Stelzer, "Light-sheet fluorescence microscopy for quantitative biology," *Nat. Methods* **12**, 23–26 (2015).
- [8] B.-C. Chen, W. R. Legant, K. Wang, L. Shao, D. E. Milkie, M. W. Davidson, C. Janetopoulos, X. S. Wu, J. A. H. Iii, Z. Liu, B. P. English, Y. Mimori-kiyosue, D. P. Romero, A. T. Ritter, J. Lippincott-Schwartz, L. Fritz-laylin, R. D. Mullins, D. M. Mitchell, J. N. Bembenek, A.-C. Reymann, R. Böhme, S. W. Grill, J. T. Wang, G. Seydoux, U. S. Tulu,

- D. P. Kiehart, and E. Betzig, "Lattice light-sheet microscopy: Imaging molecules to embryos at high spatiotemporal resolution," *Science* **346**, 1257998 (2014).
- [9] R. Galland, G. Greci, A. Aravind, V. Viasnoff, V. Studer, and J.-B. Sibarita, "3D high- and super-resolution imaging using single-objective SPIM," *Nat. Methods* **12**, 641–644 (2015).
- [10] M. B. M. Meddens, S. Liu, P. S. Finnegan, T. L. Edwards, C. D. James, and K. A. Lidke, "Single objective light-sheet microscopy for high-speed whole-cell 3D super-resolution," *Biomed. Opt. Express* **7**, 2219–2236 (2016).
- [11] R. W. Cole, T. Jinadasa, and C. M. Brown, "Measuring and interpreting point spread functions to determine confocal microscope resolution and ensure quality control," *Nat. Protoc.* **6**, 1929–1941 (2011).
- [12] W. Saxton and W. Baumeister, "The correlation averaging of a regularly arranged bacterial cell envelope protein," *J. Microsc.* **127**, 127–138 (1982).
- [13] M. van Heel, "Similarity measures between images," *Ultramicroscopy* **21**, 95–100 (1987).
- [14] M. Unser, B. L. Trus, and A. C. Steven, "A new resolution criterion based on spectral signal-to-noise ratio," *Ultramicroscopy* **23**, 39–52 (1987).
- [15] R. P. J. Nieuwenhuizen, K. A. Lidke, M. Bates, D. L. Puig, D. Grünwald, S. Stallinga, and B. Rieger, "Measuring image resolution in optical nanoscopy," *Nat. Methods* **10**, 557–562 (2013).
- [16] S. Hari, "Resolution test target for optical nanoscopy," Delft University of Technology (dissertation in preparation).

LIST OF PUBLICATIONS

4. **N. Chakrova, A. Soler Canton, C. Danelon, S. Stallinga and B. Rieger**, *Adaptive illumination reduces photobleaching in Structured Illumination Microscopy*, *Biomedical Optics Express* **7**, 4263–4274 (2016).
3. **N. Chakrova, B. Rieger, and S. Stallinga**, *Deconvolution methods for structured illumination microscopy*, *Journal of the Optical Society of America A* **33**, 12–20 (2016).
2. **N. Chakrova, R. Heintzmann, B. Rieger, and S. Stallinga**, *Studying different illumination patterns for resolution improvement in fluorescence microscopy*, *Optics Express* **23**, 31367–31383 (2015).
1. **N. Chakrova, B. Rieger, and S. Stallinga**, *Development of a DMD-based fluorescence microscope*, *Proceedings of SPIE* **9330**, 933008 (2015).